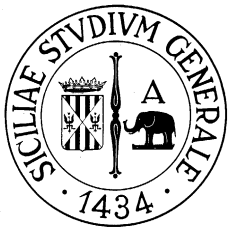

Università degli studi di Catania
Facoltà di scienze matematiche fisiche e naturali
Dottorato di ricerca in Fisica

FRANCESCO CAVALLARO

A Pathway to EMU: The SCORPIO Project

PhD Thesis

COORDINATOR:
Prof. V. Bellini
SUPERVISOR:
Prof. F. Leone
TUTORS:
Dr. C. Trigilio

XXIX Ciclo

Contents

List of Tables

List of Figures

Chapter 1

Introduction

We are entering a golden age for radio astronomy. There are several new interferometers upcoming, whose characteristics, in terms of sensitivity, frequency coverage, angular and temporal resolution, field of view etc., will permit unprecedented deep observations. The most outstanding ones among them will be the Square Kilometre Array (SKA, Carilli & Rawlings 2004) and its precursors, such as the Australian SKA Pathfinder (ASKAP) and MeerKAT. Several surveys will be carried out, in continuum and spectral line. In particular, in continuum, the scientific interest is both for galactic and extragalactic science, for which surveys at low or high galactic latitude are planned, such as the Evolutionary Map of the Universe (EMU; Norris et al. 2011), to be carried out with ASKAP, the MeerKAT International GigaHertz Tiered extra-galactic Exploration Survey (MIGHTEE, Jarvis 2015) and the MeerKAT High Frequency Galactic Plane Survey (Meer-GAL), both to be carried out with MeerKAT.

Many radio surveys have been carried out in the past years. In continuum the NRAO Very Large Array (VLA) Sky Survey (NVSS; Condon et al. 1998) is the largest existing survey. Other important surveys are the Multi-Array Galactic Plane Imaging Survey (MAGPIS; Becker, White, & Helfand 2006), the Co-Ordinated Radio 'N' Infrared Survey for High-mass star formation (CORNISH; Purcell & Hoare 2010), the HI, OH, Recombination line survey of the Milky Way (THOR; Bihr et al. 2016). In the following, we briefly discuss NVSS, the largest and most important existing survey.

NVSS was carried out with the Very Large Array between 1993 and 1996 in compact D configuration at 1.4 GHz. It covered ~ 10.3 sr of sky with J2000 $\delta > -40^\circ$ in 217 466 pointings. It produced a catalogue of more than 2 million sources, with an angular resolution of $45''$ and a rms of 0.45 mJy beam^{-1} (Condon et al., 1998). The EMU survey will cover a sky area comparable to NVSS, but it will be 45 times more sensitive and with a better

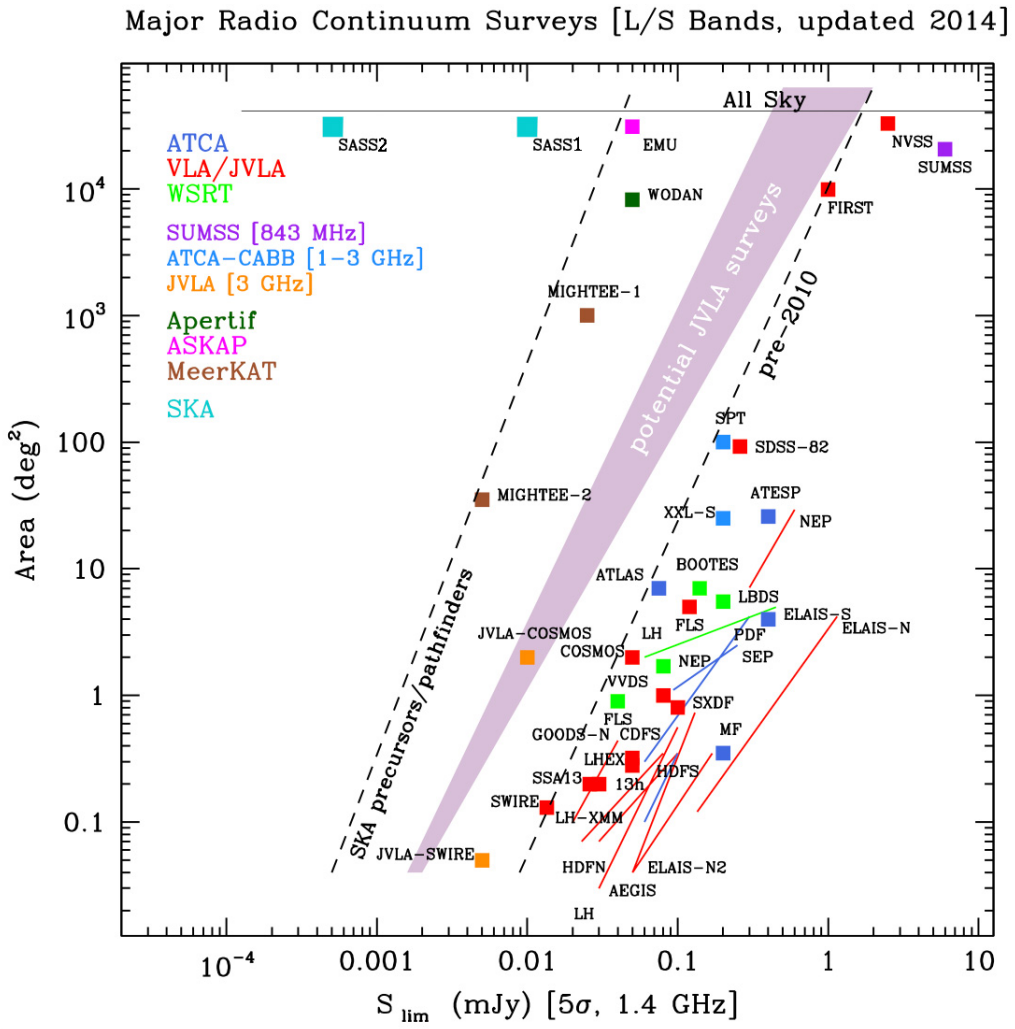

Figure 1.1: Area plotted against sensitivity of the most important surveys pre-2010 compared to the future ones (Norris et al., 2015). The plot shows that we will explore an unexplored survey parameter space, that will, for sure, produce a lot of new results.

angular resolution. Considering also the difference in the *uv* coverage, EMU will be also more sensitive to extended structures. In Fig. 1.1 (Norris et al., 2015) we report the area of the surveys plotted against their sensitivity. Thanks to the new telescopes we should cross the "pre-2010 line" and have larger and more sensitive surveys. Details on what we could expect from EMU are discussed in the Sec 2.3.

The main focus of this thesis is on radio stars and the science that can be carried out with the new radio interferometers. Even if, in general, stars emit in radio a small fraction of their luminosity, at these wavelengths it is possible to trace different phenomena that is not possible to study by other means, e.g. the physics of their magnetospheres, the interaction with the ISM in the first and in late phases of their lives, etc. Furthermore the Galaxy is optically thin in radio, then we can observe stars in the GP that we could not observe in the optical frequencies. Unfortunately, due the faintness of stars in radio, the number of currently known radio stars is limited to a small sample.

1.1 Radio sources

One of the main goal of this work is the characterisation of different kind of radio sources. The flux density of a radio source can be generically expressed as Hjellming (1988):

$$S_\nu = \frac{T_B \theta_1'' \theta_2''}{1960 \lambda_{\rm cm}} \,\mathrm{Jy} \tag{1.1}$$

where T_B is the brightness temperature, θ_1'' and θ_2'' are the angular dimension of the source in arcsec and $\lambda_{\rm cm}$ is the wavelength at which we observe in cm. This means that a source must have either high angular dimension or high brightness temperature to be detected. For thermal emission we usually have a extended source with a low brightness temperature, while for non-thermal emission it is the opposite.

In the next sections we will show the main emission mechanism in the radio wavelength and we will give an overview of the most common source classes.

1.1.1 Emission mechanism

One way to discriminate sources is to study their emission mechanism. Knowing what makes a source emit in radio can unveil its physics and exclude that it is part of a particular class. The main responsible of the radio emission in

continuum are the bremsstrahlung and the synchrotron. The bremsstrahlung emission is caused by the coulombian interaction between a free electron and a nucleus. If the plasma is in thermodynamical equilibrium, the emission mechanism is called thermal breamsstrahlung. Synchrotron is a non-thermal mechanism, where the emission is caused by the interaction between ultra-relativistic electrons ($\gamma > 10$, where $\gamma = (1 - v^2/c^2)^{-\frac{1}{2}}$ is the Lorentz factor and v is the speed of the electrons) with a non-thermal energy distribution (usually a power law $N(E) = N_0 E^{-\delta}$) and a magnetic field. If the electrons are non-relativistic this mechanism is called cyclotron ($\gamma < 1$) and it is called gyro-synchrotron for $1 < \gamma < 10$.

One way to discriminate between different emission mechanism is to study the source Spectral Index Distribution (SED). A parameter that characterises the SED in the radio wavelengths is the spectral index α, defined as $S(\nu) = S_0 \left(\frac{\nu}{\nu_0}\right)^{\alpha}$, where $S(\nu)$ is the flux density of the source at a given frequency ν and S_0 is the flux density at the frequency ν_0. The spectral index can change with the frequency, but both synchrotron and bremsstrahlung lose this dependence in the two limits $\tau \gg 1$ and $\tau \ll 1$, where τ is the optical depth of the source. In particular, in case of a homogeneous source of thermal bremsstrahlung we have $\alpha = 2$ for $\tau \gg 1$ while, for $\tau \ll 1$, it is $\alpha = -0.1$. If the density is not constant, the spectral index changes. When the density varies as r^{-2}, as in the case of symmetrical spherical wind from hot stars, the spectral index is $\alpha = 0.6$ (Panagia & Felli, 1975).

In the case of a homogeneous source of synchrotron we have $\alpha = 2.5$ for $\tau \gg 1$ and, for $\tau \ll 1$, it depends on the spectral index δ of the energy distribution of the relativistic electrons, giving us information on this physical parameter. In particular $\alpha = \frac{\delta - 1}{2}$ so, for typical values of δ, it ranges between -1 and -0.5 (Burke & Graham-Smith, 2014).

The frequency at which a source has an optical depth $\tau = 1$ is the turnover frequency. Measuring the turnover frequency can allow us to constrain additional physical parameters, such as magnetic field intensity or electronic density. In Fig. 1.2 and 1.3 we show a typical spectrum of a bremsstrahlung emitting source and a syncrotron emitting one.

1.1.2 Extra-galactic sources

With the expression "extra-galactic sources" we intend all the sources external to our Galaxy. Generally speaking, these sources are far galaxies. The most luminous class of extra-galactic radio sources are the Radio Galaxies, distant Radio-Loud Quasars and Blazars. Their radio emission originates from the processes occurring in their nuclei, hosting a supermassive black

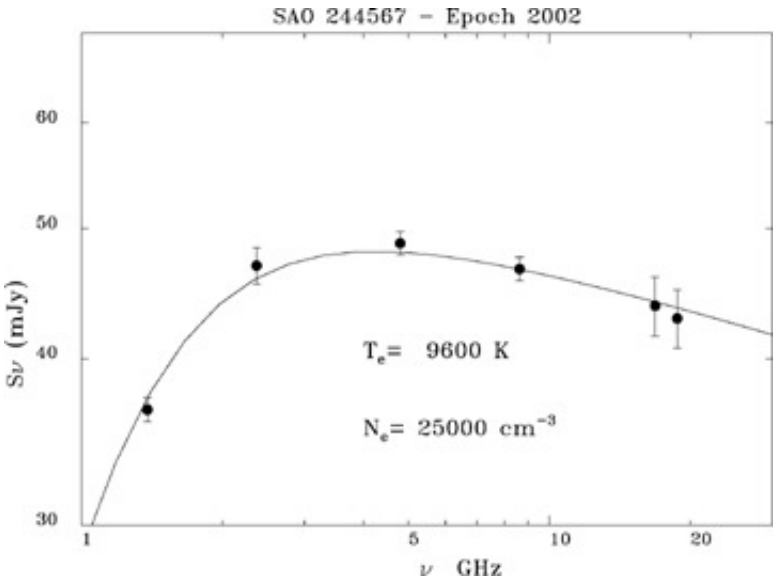

Figure 1.2: Spectrum of the SAO 244567 nebula (Umana et al., 2008). It presents the typical thermal bremsstrahlung spectrum.

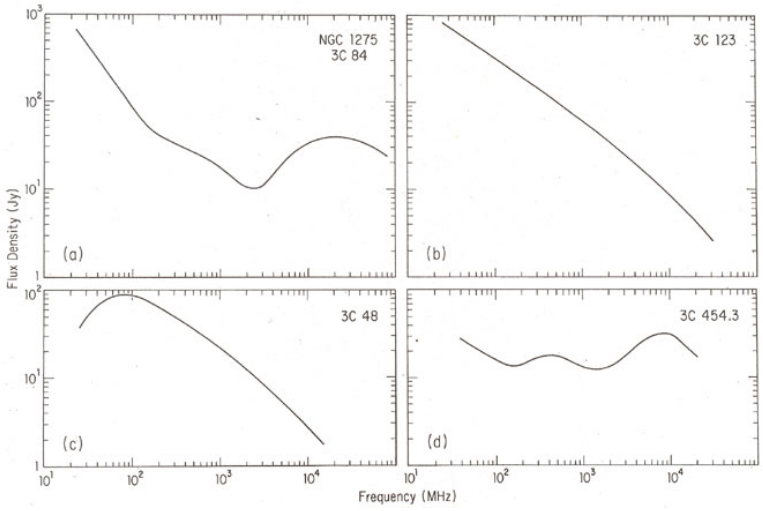

Figure 1.3: Spectra of four galaxies. NGC 1275 and 3C 454.3 (first and last panels) present a superposition of different emission mechanism, while 3C 123 and 3C 48 (second and third panels) present a synchrotron spectrum (Verschuur, Kellermann, & van Brunt, 1974)

hole. For this reason they are called Active Galactic Nuclei (AGN).

AGNs produce high luminosity in a compact volume, with processes different from the star nuclear fusion. The gravitational energy released by cold gas accreting onto the central supermassive Black Hole (SMBH) is converted in electromagnetic radiation and represent the emission source of the AGN. The SMBH loses angular moment because of viscous processes in the accretion disc, resulting also in high soft X-ray ($\lesssim 10$ keV) luminosity. Evidence of hard X-ray ($\gtrsim 10$ keV) emission is sometimes found toward the SMBH. There are emission lines in the optical and in the UV originating from the rapidly moving gas in the gravitational potential that are usually obscured by the cold matter torus rotating in a larger orbit around the SMBH. Along the rotation axis of the SMBH, matter is ejected in plasma jets that show radio emission. The most powerful radio sources are generally hosted in elliptical galaxies (Urry & Padovani, 1995).

Radio galaxies consist of an elliptical or spiral galaxy containing the AGN, and two spatially symmetric lobes. These lobes are formed by the ejected AGN plasma and are confined by the magnetic field and deposited in the intergalactic medium. They contain ultra relativistic electrons accelerated in a magnetic field of the order of 10^{-5} G. The spectral index α is usually around -0.8, where $S(\nu) \propto \nu^{\alpha}$ (Burke & Graham-Smith, 2014). Galaxies with the jet beamed towards us result in a compact observed object with a really high luminosity (it could be 3 orders of magnitude brighter than an equivalent not beamed source). In the more compact AGN the radio emission can be optically thick, resulting in a flatter spectrum. They are historically divided into 2 categories, Fanaroff-Riley of type 1 (FR I) and type 2 (FR II) (Fanaroff & Riley, 1974). FR I galaxies are brighter near the central body and become fainter the as one approaches the outer extremities of the lobes (see Fig. 1.4), while FR II galaxies have their brightest point at the edge of the jets, in the region where they collide with intergalactic medium (see Fig. 1.5).

The Gigahertz Peaked Spectrum (GPS) and Compact Steep Spectrum (CSS) are two classes of compact extra-galactic objects, about 1 kpc in size the first, some tens the latter. They can be young radio galaxies or "frustrated" ones, that means contained into a particularly dense intergalactic medium that limits their espansion and dimension (Randall et al. 2011; Fanti 2009). Their name is due to the particular shape of their spectra. CSS have a steep spectrum ($\alpha \leq -0.5$), while the GPS spectra have a peak around $1 \sim 10$GHz, their turnover is caused by the synchrotron self-absorption. Both of them are usually unresolved (they are resolved using VLBI methods) because of their small dimensions.

In normal spiral galaxies the emission is caused by the synchrotron of the

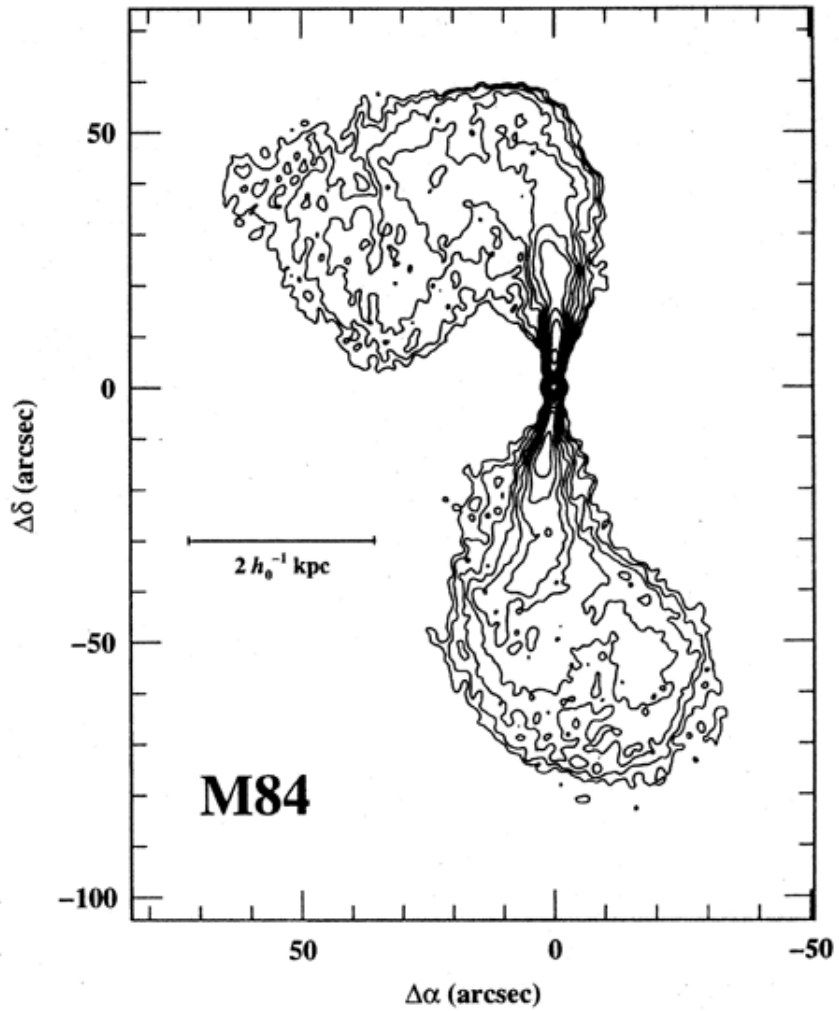

Figure 1.4: Example of an Fanaroff-Riley type I (FR I) galaxy. This is a radio map of the Virgo cluster elliptical galaxy M84 (Laing & Bridle, 1987).

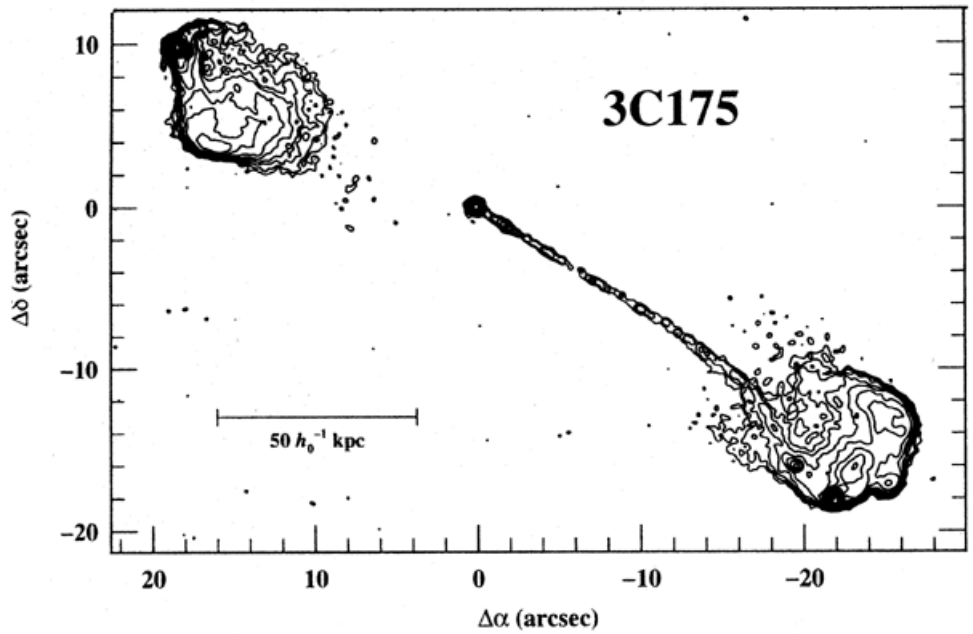

Figure 1.5: Example of an Fanaroff-Riley type II (FR II) galaxy. This is a map of the quasar 3C 175, as observed with the VLA at 4.9 GHz (Bridle et al., 1994)

relativistic cosmic rays diffused in the galaxy that interact with its magnetic field. The emission is correlated with the star formation rate. Galaxies with a higher than average star formation rate are called Star Forming Galaxies (SFG). Star Burst Galaxies (SBG) are characterised by a even higher star formation rate so, given the higher number of supernovae, their synchrotron emission is enhanced (Burke & Graham-Smith, 2014).

1.1.3 Galactic sources

The typical radio sources that we can observe within our Galaxy are: the Galaxy itself, with the diffuse radio emission, H II regions, circumstellar envelopes of evolved stars, different type of stars. Many discrete sources in nearby galaxies can also be studied in a similar way thanks to their proximity.

H II regions

The H II regions are ionised nebulae surrounding one or more early type young stars. The linear size of the nebulae can range from 0.03 pc to 100 pc and more (see Table 1.1). Inside the nebulae there is a stationary equilibrium

Class of Region	Size (pc)	Density (cm^{-3})	Ionised mass ($M_\odot$)
Hypercompact	$\lesssim 0.03$	$\gtrsim 10^6$	$\sim 10^{-3}$
Ultracompact	$\lesssim 0.1$	$\gtrsim 10^4$	$\sim 10^{-2}$
Compact	$\lesssim 0.5$	$\gtrsim 5 \times 10^3$	~ 1
Classical	~ 10	~ 100	$\sim 10^5$
Giant	~ 100	~ 30	$10^3 \sim 10^6$
Supergiant	> 100	~ 10	$10^6 \sim 10^8$

Table 1.1: Physical parameters of H II regions (Kurtz, 2005).

between the ionisation caused by the UV light from hot young stars and the recombination. The electron temperature is around 8000 $\sim$ 10000 K. The radio emission is caused by the thermal bremsstrahlung (free-free emission), the turnover frequency depends on the density and the temperature of the object but it is usually around 1 GHz (Burke & Graham-Smith, 2014). In Fig. 1.6 it is shown a compact H II region. Note the 8-μm emission surrounding the radio emission, as in most of the H II region, is explained as thermal emission arising from very small dust grains (PAH), that are located far from the central ionising source, beyond the photo dissociation region (PDR) (Deharveng et al., 2010).

Supernovae Remnants

Stars with a mass larger than $8M_\odot$ in main sequence end their life in a catastrophic way: their core collapses in less than a second leaving a compact object as a neutron star or a black hole, while the energy released accelerates the matter outward in a violent explosion in the phenomena called supernovae. Supernovae are caused also by the thermonuclear explosion of a white dwarf in a close binary system, where the companion, a giant o supergiant star, loses mass through the Roche lobe accreting the white dwarf until they reach the Chandrasekhar limit. These are type Ia supernovae. The matter ejected by the star, interacting with the interstellar medium, produces a shell enclosing a nebulae called supernovae remnant (SNR) (see Fig. 1.7). The radio emission of the SNR becomes dominant with respect to the optical as the nebulae evolve and it is caused by the synchrotron emission of the shock-accelerated ultra-relativistic electrons. The spectral index α is usually around -0.5 (see Fig 1.8), as predicted by the Diffusive Shock Acceleration theory (Bell 1978a,b). There are SNRs with steeper or flatter spectra. In particular the latter can be due to the presence of a Pulsar Wind

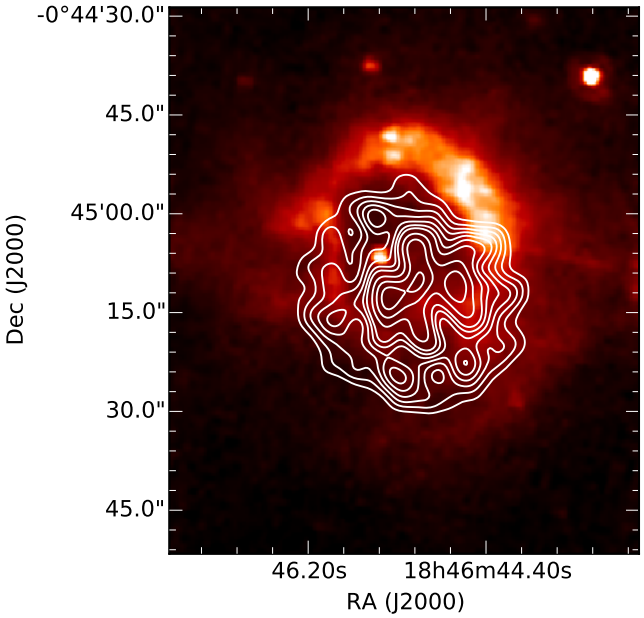

Figure 1.6: Superposition of 8-μm image and 6-cm contours of MGE 031.7290+00.6993 (Ingallinera et al., 2016).

Nebulae (PWNe), to the interaction with molecular clouds or to adding up of the thermal emission.

Radio Stars

This review is mostly based on Seaquist (1993). Most of the objects visible with your naked eye in the sky are stars. Many of them, because they rely only on their photospheric black body radiation to emit in radio, are quite faint radio source. In fact, stars like our Sun have a radio luminosity ~ 13 orders of magnitude smaller than their bolometric luminosity and, while our Sun is near so it is nevertheless a very strong radio source, even the nearest star is a really faint source. However, many stars are visible in radio, emitting not only for the normal black body mechanism but also by other mechanisms, that could be either thermal or non-thermal. In this section we will discuss all the star classes known to be radio emitters, commonly known as radio stars. As shown in Fig. 1.9 radio stars cover all the HR diagram. However, all the stars known for being radio emitters were found by targeted observations, leading to an observation bias.

OB and Wolf-Rayet Stars

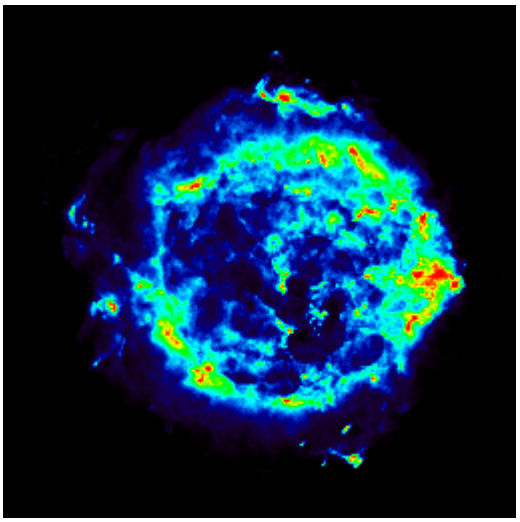

Figure 1.7: Image of Cassiopeia A in radio, taken with the VLA in the NVSS survey.

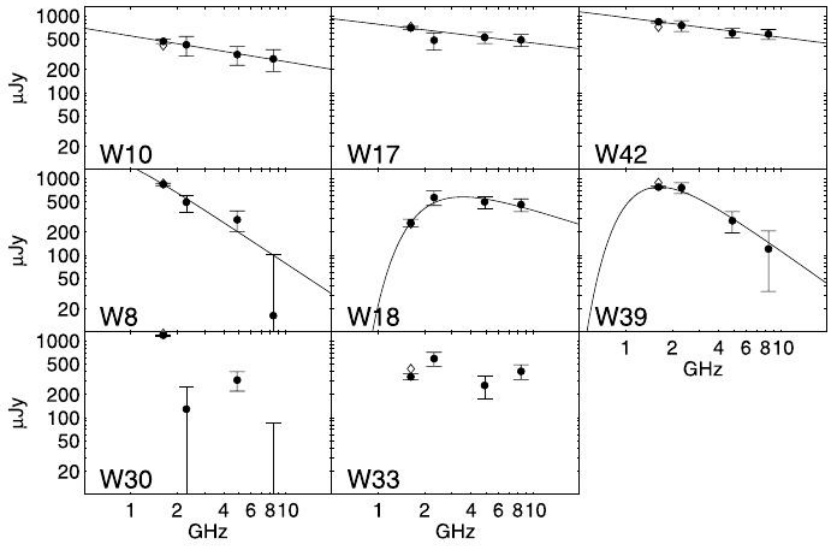

Figure 1.8: Radio spectra of some supernovae remnant older than 11 years (Parra et al., 2007).

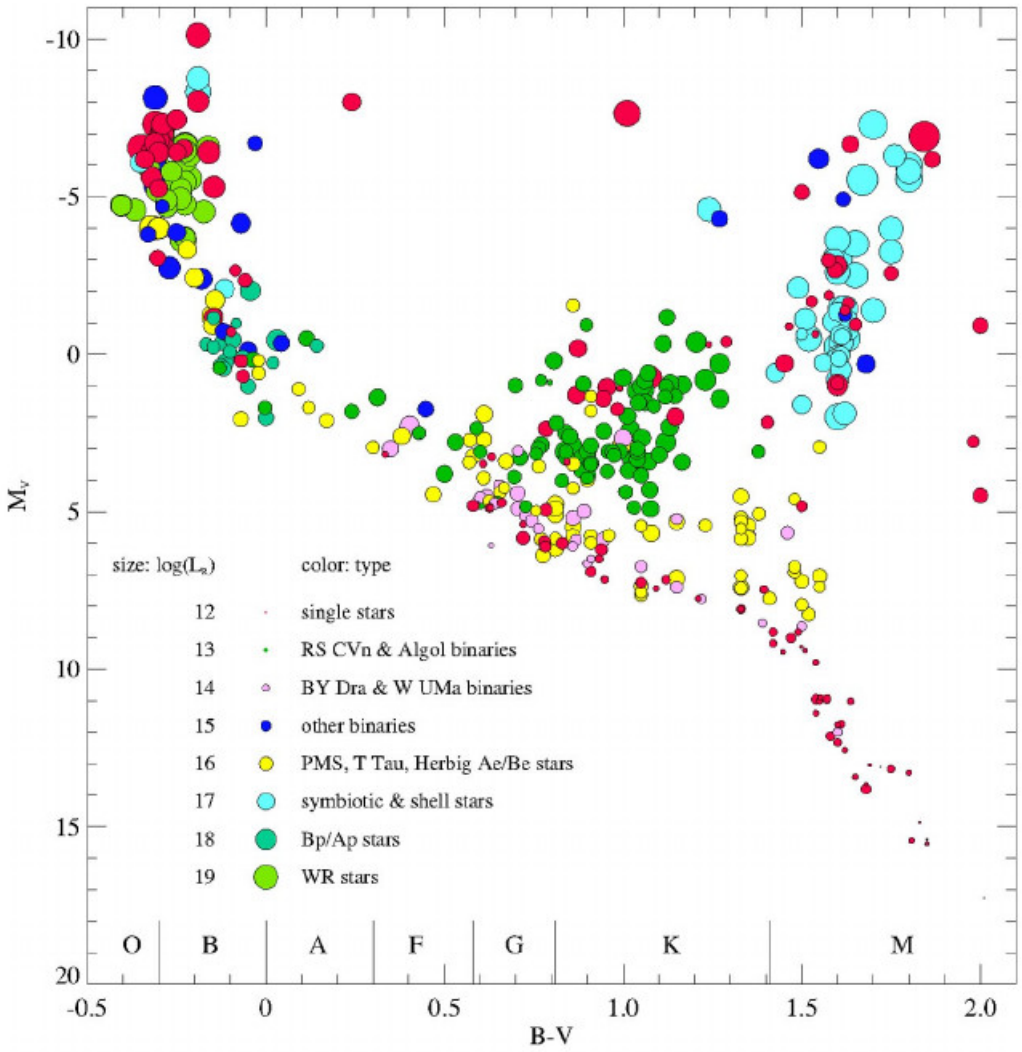

Figure 1.9: HR diagram of all known radio stars as in the Güdel (2002) 440 stars sample.

The Luminous OB stars are the most visible optical tracers of star formation. They undergo mass loss at rates of about 10^{-6} $M_\odot$ yr^{-1} with wind speed at $1 \sim 3 \times 10^3$ km s^{-1}. The Wolf-Rayet (WR) stars are similarly massive stars ($\sim 20\,M_\odot$) at the end of their life with even greater mass loss rates (10^{-5} $M_\odot$ yr^{-1}), so large that the wind is optically thick at optical wavelengths, obscuring the stellar surface (Usov, 1992). Radio emission is commonly detected from OB stars and WR stars at cm wavelengths and it is typically due to the thermal bremsstrahlung emission of an optically thick stellar wind. If the wind is steady, spherically simmetric and at constant speed, the mass continuity law requires $n_e \propto r^{-2}$, where n_e is the electron density and r is the distance from the star. In this case the star flux density S is proportional to $\nu^{0.6}$ (Panagia & Felli, 1975). Some of these stars have been detected with a non-thermal emission component (Bieging, Abbott, & Churchwell, 1989) caused by the synchrotron radiation from a population of ultra-relativistic electrons embedded or entrained in the wind. The accepted model to take into account these electrons was proposed by Williams et al. (1990). They suggested that the acceleration is caused by a shock associated with the collision between the winds of two components of a binary, one of which is typically a WR star and the other an O-type companion. These stars are nowadays called symbiotic.

Single red giants and supergiants

Red giants and supergiants are cool, highly evolved stars with radii that can reach several AU. For this reason, they can have a large angular size (up to tens of mas) and, even if the brightness temperature is about 3000 K, they can be detected at radio wavelengths as black body emitters. Photospheres can be studied in this way. Red giants and supergiants are characterized by massive stellar winds. The mass loss rates generally increase with spectral class. In extreme cases, the rate is as high as OB and WR stars but the wind speed is slower (tens of km s^{-1}). However, the continuum radio emission is substantially weaker than their early-type counterparts because the winds are cool and, generally, not-ionised, unless the giant possesses a hot companion which fully ionises a portion of its wind (like the case of symbiotic stars). Because of that, the spectral index of the emission is generally between 0.6 (ionised wind) and 2 (black body radiation). Red giants and supergiants can also have spectral line emission from circumstellar molecules and OH, H_2O and SiO masers, especially the ones in the Asymptotic Giant Branch (AGB).

Flare stars

Flare stars are single stars at the faint end of the main sequence and exhibit activity closely related to chromospheric activity on the sun, intense flares in many regions of the EM spectrum, from X-rays to radio waves. While the earlier type could host a solar-like dynamo effect thanks to the transition line between the radiative and the convective zone, called thacocline (Spiegel & Zahn, 1992), the stars below $M = 0.35 M_{\odot}$ are completely convective and they do not present a tachocline. We also observe that the strong correlation between X-ray and radio luminosities established by Guedel & Benz (1993) for stars of spectral types ranging from F to mid M is not valid for very low mass dwarfs which exhibit very strong radio emission whereas X-ray emissions dramatically drop (Berger, 2006). So there must be another mechanism to produce the dynamo. However this is yet not completely understood (Morin et al., 2010), even if the observations show us that partly convective stars possess a weak non-axisymmetric field with a significant toroidal component, while fully convective ones exhibit strong poloidal axisymmetric dipole-like topologies (Donati et al. 2008; Morin et al. 2008). In radio we observe a much higher activity from the later types, as discussed later in Section 3.3.3.

Active Binary Systems: RS CVn and Algol system

RS CVn are close detached binary systems of two late-type stars, usually a main sequence G-type star and a K0 subgiant. The magnetic reconnection caused by the interaction of the magnetospheres accelerates the particles. The particles begin to interact with the magnetic field and produce gyrosynchrotron emission. We usually see an emission localised around the subgiant exhibiting a flat spectrum (Mutel et al., 1987). Algol systems are similar to RS CVn but they are semi-detached binaries, where the less massive star has evolved to fill its Roche lobe and transfers mass to the less evolved more massive star (1.10). This condition is possible if the evolved star was the more massive prior to transferring significant mass to its companion. The radio properties are similar to those observed in RS CVn stars (Umana, Catalano, & Rodono, 1991).

Pre-main sequence star

The pre-main sequence stars (PMS), known as T Tauri stars are very young variable emission line stars of about 1 $M_{\odot}$ still contracting toward the main sequence. They are frequently found in groups or associations in the central regions of molecular clouds where star formation is active. T Tauri stars are recognised to comprise two classes: the so-called classical T-Tauri stars

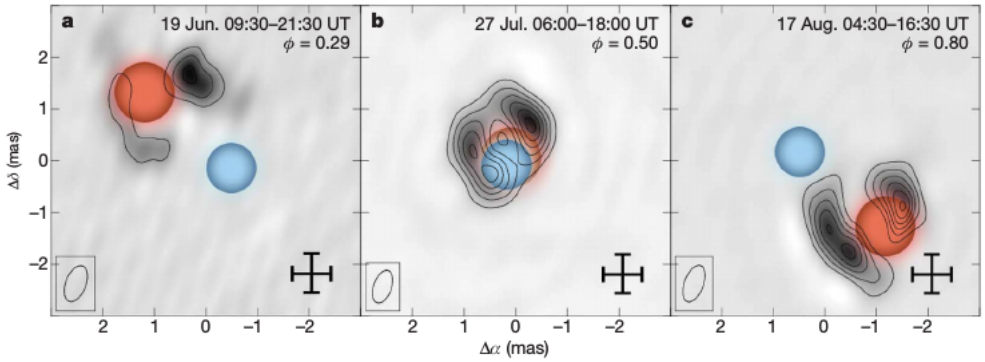

Figure 1.10: Radio images of Algol at three different orbital phases. Notice the radio emission localised near the evolved star, pointing towards the main sequence star (Peterson et al., 2010). The cross represents the position error.

(CTT) exhibit strong evidence for circumstellar matter and appear to be sources of thermal free-free radio emission from ionised gas, while the weak-lined stars (WTT) exhibit weaker evidence for circumstellar matter and emit non-thermal emission from magnetically active regions. For the CTT, the radio spectral indices generally fall within the range $1 \sim 2$ (Bieging, Cohen, & Schwartz, 1984) (probably due to an optically thick free-free emission) and some have the canonical value of 0.6 applicable to a steady outflow. They are also sources of line emission. WTT radio properties are similar those observed in RS CVn stars, showing a non-thermal mechanism associated with a gyrosynchrotron (Smith et al., 2003).

Microquasar

Microquasars are X binaries that have an emission mechanism analogue to the quasars. A microquasar consists of a central compact object with an accretion disc. The disc emits X-rays, while the jets of relativistic magnetised plasma ejected from the compact objects emit in the radio waves, just like quasars. The difference is that the microquasar compact object is a stellar black hole or a neutron star and the disc matter comes from a companion star that fills the Roche lobe and transfers matters through the Lagrange point L1. The radio emission is usually detected during the relativistic ejection of matter, but sometimes there is a continuous emission due to the interaction of the jets with the interstellar medium (Miller-Jones et al., 2007). The flare radio emission presents a classical synchrotron spectrum (see Fig. 1.11) and it can last some days (Mioduszewski et al., 2001).

Pulsar

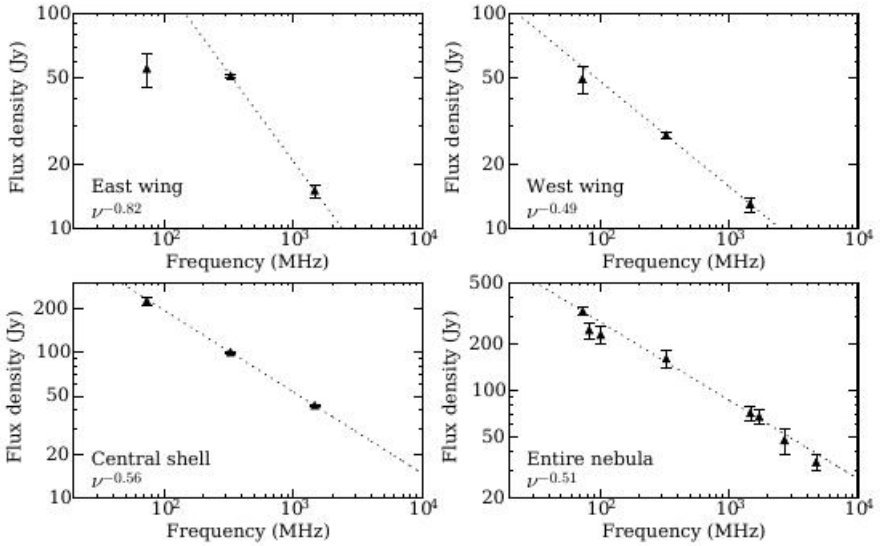

Figure 1.11: Spectrum of the W50 nebulae components, surrounding the SS433 microquasar (Miller-Jones et al., 2007)

Pulsars are rotating neutron stars with a strong magnetic field (it can be as high as 10^{15} G). They emit from the magnetic poles, with the magnetic axis misaligned respect to the rotation axis (oblique rotator model: ORM). They are what remains, apart from the nebulae, from a core collapse Supernovae that has a core too little massive to form a black hole. It is possible to observe them at regular intervals, with periods of pulsating emission ranging from 10^{-3} to 10 s. Some pulsars show radio emission and they are called "radio pulsars". They usually have a spectral index around -2 with a dispersion of the order of 0.5 (Bagchi, 2013).

Planetary Nebulae

Planetary nebulae (PNe) are nebulae originating from the envelope of a star with a mass $M < 8M_{\odot}$. They emerge after the AGB and post-AGB phase, a phase immediately next to the AGB one characterised by an axi-symmetric mass loss instead of spherical symmetric, a period of high mass loss rate, as soon as the exposed inner layers of the star are hot enough to ionise the surrounding envelope. PNe emit in radio via a thermal bremsstrahlung mechanism, so the spectral index is 2 at low frequencies, -0.1 at high ones (see Fig. 1.12). Nevertheless, there are planetary nebulae with spectral indices $0.6 < \alpha < 1.8$, due to not constant electronic densities, as the case of stellar winds (Gruenwald & Aleman, 2007). There are also very young planetary nebulae emitting non-thermal radiation (Cohen et al., 2006).

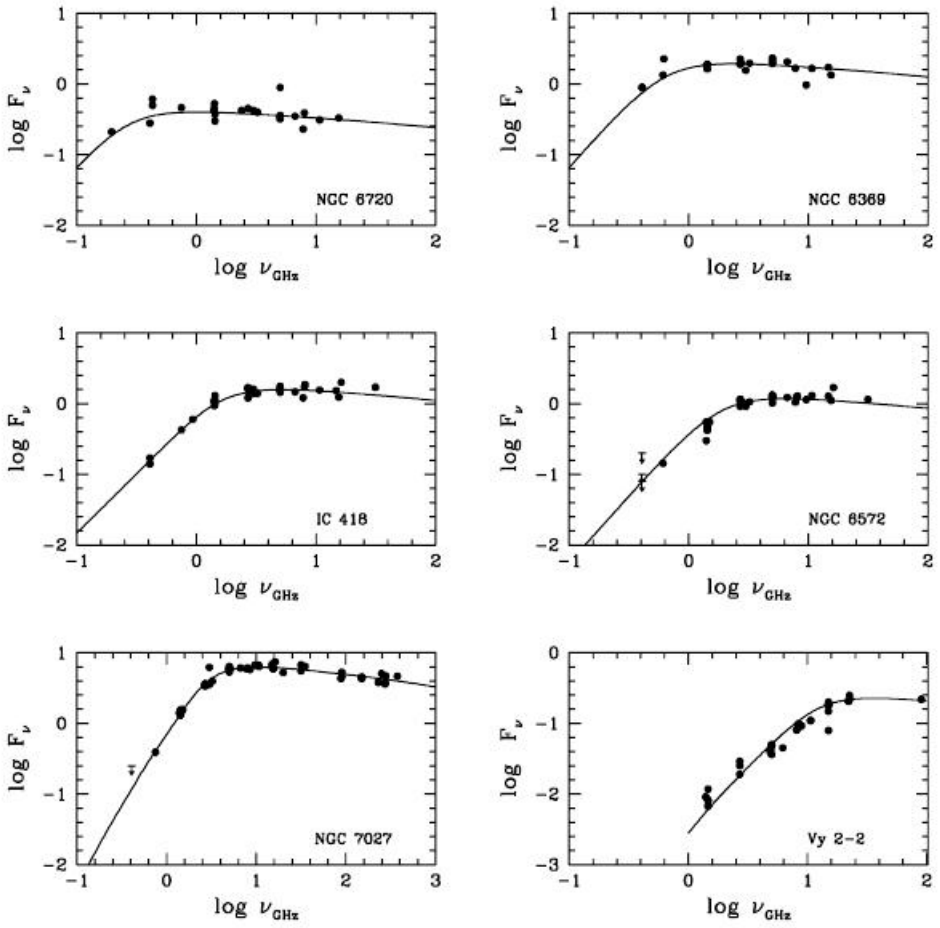

Figure 1.12: Spectrum of several planetary nebulae (Gruenwald & Aleman, 2007).

Luminous Blue Variable Stars

Luminous Blue Variable (LBV) are extremely massive stars ($M \gtrsim 10M_{\odot}$) that had a really fast evolution in the main sequence and that have a luminosity similar to the Eddington limit ($\sim 10^6 L_{\odot}$). They are characterised by a mass-loss rate of order of $10^{-5} \sim 10^{-3}$ $M_{\odot}yr^{-1}$ and by a high visual and infrared variability (Humphreys & Davidson, 1994). The envelope is highly ionised and emits, as the planetary nebulae, as a bremsstrahlung source.

Magnetic Chemically Peculiar Stars

Chemically Peculiar (CP) stars present an unusually high or low abundance of heavy elements. They are main sequence stars, usually B or A. We can distinguish 4 types of CP (Preston, 1974):

1. Am or CP1 show weak lines of singly ionised Ca and Sc but they show enhanced abundances of heavy metals;

2. Ap or CP2 or MCP (magnetic chemically peculiar) are characterised by strong bipolar magnetic field, enhanced abundances of elements such as Si, Cr, Sr and Eu, and are also generally slow rotators;

3. HgMn or CP3 are similar to the MCP but they do not show the strong magnetic field and are even slower rotators. They are characterised by strong Hg and Mn lines;

4. He-weak or CP4 show weak Helium lines.

Among them, MCP can show radio emission, especially in the centimetre wavelengths. This emission is correlated with the magnetic field and actually the most accepted model assumes that the emission is caused by a gyrosynchotron mechanism of non-thermal electrons, accelerated by magnetic reconnection (Leone et al. 2004; Trigilio et al. 2004). MCP can also emit coherent, directive and highly circularly polarised pulse of radio waves (Trigilio et al., 2000). There are two mechanisms that can cause a coherent emission in a magnetised plasma, the electron cyclotron maser emission (ECME) and plasma radiation due to Langmuir waves (Trigilio et al., 2008). In the ECME, the favourite mechanism in Trigilio et al. (2008), electrons reflected by a magnetic mirror can develop a pitch-angle anisotropy. In this condition, at certain value of plasma density and plasma frequency, found in the star considered in the paper, the ECME can arise.

1.2 Work outline

The main goals of this thesis are both scientific and technical:

1. studying the radio stars;
2. understand the issues that we will encounter in the future surveys, in particular in the Galactic Plane.

We want to estimate the radio star detection density in the next surveys and, to do that, we present two parallel approaches. In Chap 2 we describe the next generation of radio interferometers and the planned surveys. The Chapter 3 will focus on the theoretical approach and it is based on the Besançon Galactic model (Robin et al., 2003). The observational approach focuses on a project called Stellar Continuum Originating from Radio Physics in Ourgalaxy (SCORPIO, Umana et al. 2015b) a $\sim$ 5 deg^2 survey on the Galactic Plane. We will describe how we reduced and analysed the data to extract how many galactic sources we should expect. In Chapter 4 we will discuss about the SCORPIO data reduction, focusing on the issues caused by the extended emission in the Galactic Plane. Chapter 5 will focus on the spectral indices analysis and Chapter 6 on the discussion of the imaged maps and the study of some sources. At the end there will be a discussion on the results.

Chapter 2

Next generation telescopes and surveys

Between the 70s and the 80s many radio telescopes and interferometers were built. All of them were limited to a collecting area of $\lessapprox 10^4$ m^2, permitting, as an example, the study of the 21cm emission of H I up to a redshift of $z \sim 0.2$. In this period, technical improvements focused in the upgrade of receivers, of the electronics, data transport etc., but the collecting areas of the telescopes and interferometers did not increase. In the 90s the ideaof an interferometer with a very large are, up to 10^6 m^2 begins to spread into the radio astronomy community and in 2000 the Square Kilometre Array (SKA) project was approved and promised to be funded by 11 countries. The SKA is a very challenging project in particular for the new technologies involved. This requires a gradual development of the instrumentation and techniques, carried out with demonstrators, precursors and pathfinders. Among them, ASKAP and MeerKAT, at high frequencies ($\nu > 700$ MHz), the Murchison Widefield Array (MWA) and the Hydrogen Epoch of Reionization (HERA) at low frequencies ($\nu < 300$ MHz). Currently, ASKAP is in the phase of commissioning and the Early Science phase is just started. A call for proposal for surveys to be carried out was issued in 2008. Ten projects have been selected, in continuum, spectral line, pulsar search mode, high temporal resolution etc., in order to test the capability of the new instrument, to improve the techniques of observation and data reduction, to demonstrate the science that is possible to carry out. They chose two proposals to be the key science projects of the ASKAP science: the Widefield ASKAP L-Band Legacy All-Sky Blind Survey (WALLABY; Johnston et al. 2008; Duffy et al. 2012), that will survey the sky looking for the 21 cm emission of the H I, and the Evolutionary Map of the Universe (EMU; Norris et al. 2011). In this chapter we will discuss the SKA, ASKAP and EMU in details.

2.1 SKA

The SKA is an international project participated by Australia, Canada, China, India, Italy, New Zealand, South Africa, Sweden, the Netherlands and the United Kingdom. Germany left 2 years and an half ago, leaving the country number to 10. The headquarter is located at Jodrell Bank Observatory, near Manchester, UK. The SKA will feature two different arrays, consisting of two types of antennae: SKA-mid will host more than 2000 15-m dishes, located in South Africa, to explore the mid and high frequencies, while SKA-low will host up to a million low-frequency antennae, located in Australia (see Table 2.1). Nowadays, the countries funded only the first phase, called SKA1 (see Table 2.1 for technical details, the number of dishes comprises 64 MeerKAT dishes). SKA2-MID is the complete SKA high frequency project, designed to reach an rms in a 1-hour observation of 0.1 μJy and will have a resolution roughly 20 times higher.

This design is guided by the key science projects (Carilli & Rawlings, 2004):

- **Galaxy evolution, cosmology and dark energy:** the Universe is expanding and the actual theories model a force, called dark energy, that makes the Universe expand. Thanks to the SKA we will be able to track the H I, the most common element in the Universe, till the ages when the galaxies were born, knowing how its distribution evolved;
- **Strong-field tests of gravity using pulsars and black holes:** the SKA will investigate the nature of the gravity where this force is really strong, near the pulsars and, in particular, in the pulsars binary systems;
- **The origin and evolution of cosmic magnetism:** the SKA will generate a 3D large scale map of the magnetic fields in the Universe through the effect known as Faraday rotation;
- **Probing the cosmic Dawn:** the epoch of reionisation is not well studied. The SKA will cover this hole thanks to the high-redshift H I observations that it will allow;
- **The Cradle of life:** the SKA will try to answer one of the most asked question: "are we alone in the universe?". It will study star formation, stars, it will be used to search for organic molecules, such as amino acids and for the Search for ExtraTerrestrial Intelligence (SETI). It will be able to detect weak extraterrestrial signals (an airport radar in a planet 50 ly away).

	SKA1-LOW	SKA1-MID
Location	Australia	South Africa
frequency range	50-350 MHz	350 MHz-14 GHz
collecting area	0.4 km^2	33 000 m^2
antenna type	dipole	dish
quantity	$\sim 130,000$	~ 200
maximum baseline (km)	65	150
raw data output (TB/s)	157	2
resolution (arcsec)	3-20	0.03-1.2
Rms (μJy)	3	1

Table 2.1: Instrumental parameters of SKA1. The rms is calculated for a 1-hour observation, considering the whole band.

2.2 ASKAP

ASKAP is a radio interferometer, located at Murchison Radio-astronomy Observatory (MRO), in West Australia. In his final shape, it will consist of 36 antennae (see Fig. 2.1), each 12 metres in diameter, positioned in a pseudo-random way to optimise the *uv* plane coverage (see Fig. 2.2). It covers all the frequencies between 700 and 1800 MHz in 4 bands (3 nowadays, that leave a band-hole between 1300 and 1500 MHz), each 300 MHz wide divided into 16000 channels (there is some overlap). Actually, there are 12 antennae working, in the array called ASKAP-12, that just started the early science. The most innovating devices in ASKAP are the receivers, called Phased Array Feed (PAF), consisting of 188 elements, 94 in each polarisation (see Fig. 2.3). The elements work as an aperture array, whose signal is directly modulated onto optical fibre link that can transverse several kilometres to the digital receiver and the beamformer in the control building (Chippendale et al., 2015). For each antenna, the beamformer combines the digital signal of all the elements of the PAF in order to build 36 beams, each one with a ~ 1 deg^2 area at 1.4 GHz, that overlaps and form a ~ 30 deg^2 field of view (FOV) (see Fig. 2.4[1]). Thanks to this huge FOV, ASKAP will be the fastest survey telescope at his wavelength.

[1] `http://www.atnf.csiro.au/projects/askap/news_aces_15042016.html`

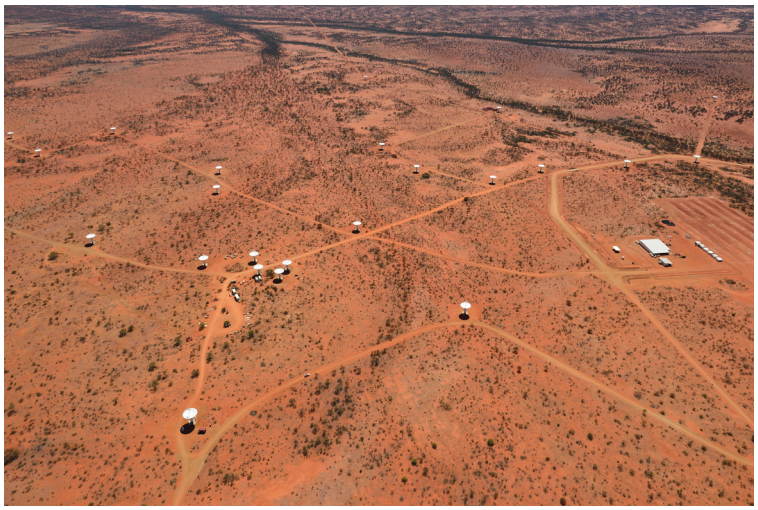

Figure 2.1: The ASKAP site from captured from an helicopter.

2.3 EMU

The Evolutionary Map of the Universe (EMU) is a deep blind survey of all the southern sky up to a declination of +30° (75% of the sky). The rms will be 10 μJy, so, adopting a 5σ detection limit, we will detect all the sources brighter than 50μJy. The expected angular resolution is 10 arcSection The observations will take 2 years and they will be carried out at 20 cm, in the 1120-1420 MHz band.

EMU will provide a whopping 70 millions detections of galaxies, a number $\sim$ 30 times higher than the total number of galaxies knows nowadays, to a redshift as high as 6 (see Fig. 2.5 for the expected distribution; Norris et al. 2015). Half of the galaxies are expected to be AGN while the others will be normal galaxies (the radio sky is not dominated by AGNs at this sensitivity; Norris et al. 2011). The key science goals for EMU are:

1. trace the evolution of the universe from $z = 2$ to the present, using the galaxies;

2. trace the evolution of AGNs and supermassive black holes in our universe;

3. use the distribution of the source to do cosmological studies;

4. explore a new region of the phase space, willing to find new classes of objects;

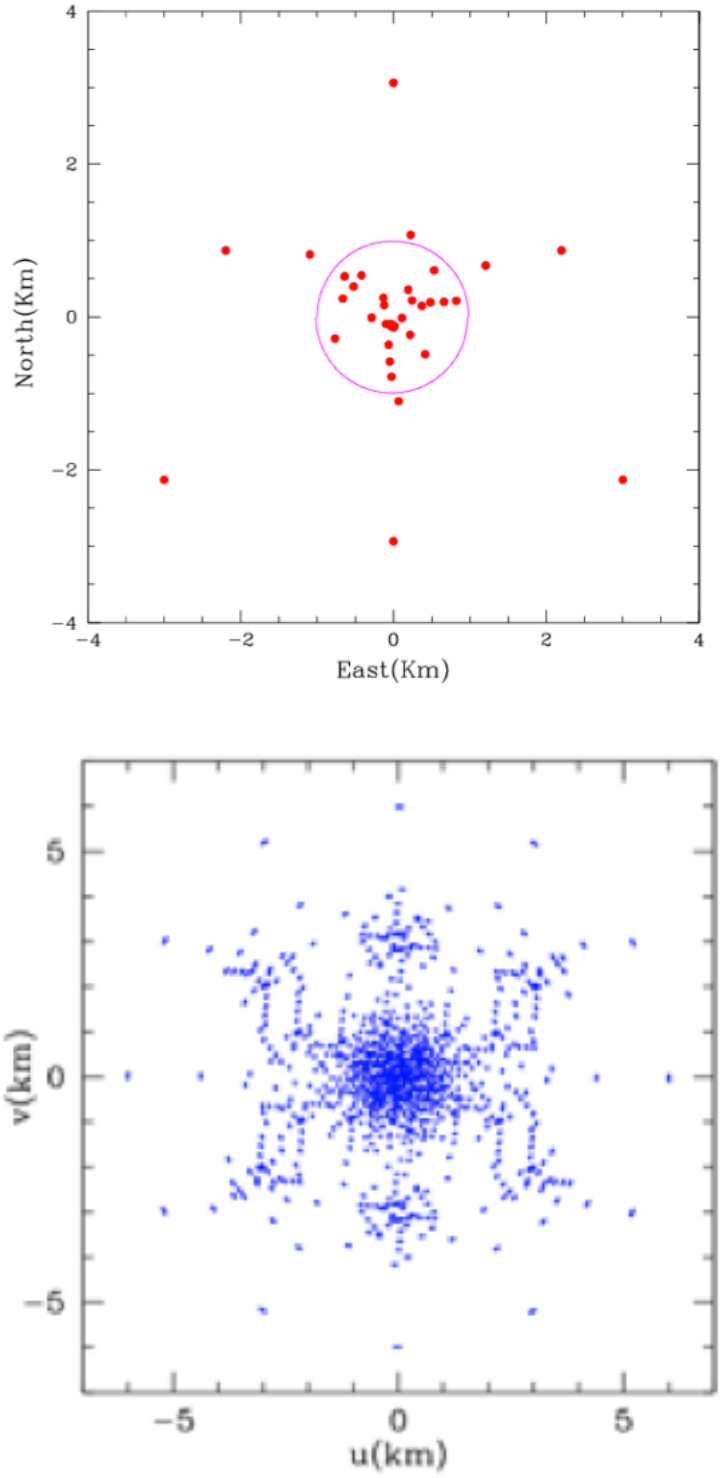

Figure 2.2: ASKAP antennae configuration and corresponding *uv* plane in a 12 minute observation.

Figure 2.3: Phased Array Feed mounted on an ASKAP antenna.

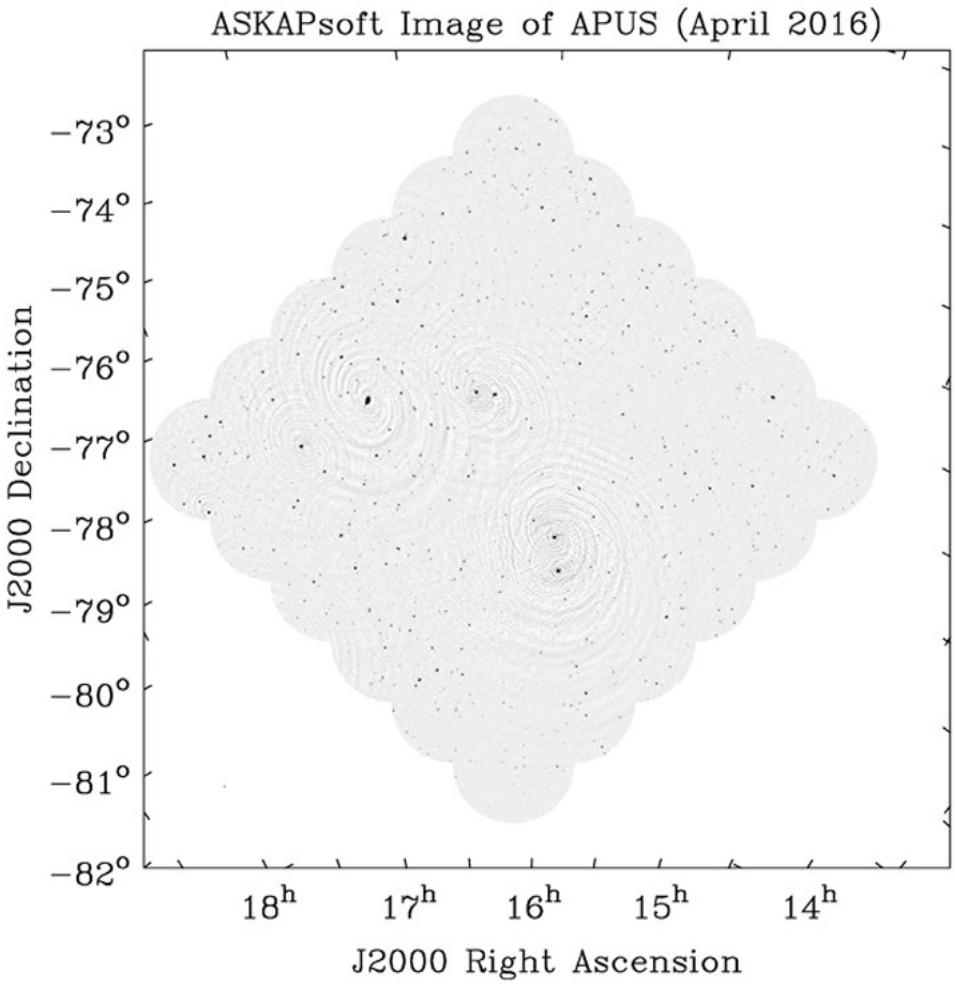

Figure 2.4: First image of ASKAP-12 at 36 beams. Notice the huge FOV.

5. create the larger atlas of the Galactic continuum emission in the southern emisphere.

Even if most of the goals are extra-galactic oriented, EMU will observe a large portion of the Galactic Plane so, based on what NVSS (see the Introduction) did, there will be a huge impact of EMU on it. Goals of the galactic science include:

1. a complete catalogue of all the massive stars in their early stages;
2. a better understanding of the complex structure of giant H II regions and how the star formation is triggered in the inside;
3. a more complete catalogue of supernovae remnants, especially the most compact one;
4. detections of planetary nebulae, which can help estimate the rate formation of the smaller stars;
5. detections of radio stars and pulsars;
6. discover the unexpected.

We are interested, for this thesis, in the fifth point, the detections of radio stars. EMU, thanks to its sensitivity, is expected to detect a large amount of stars of different classes. EMU will be the first blind survey for stars, allowing us to overcome the problem that all the stars known as radio emitters so far have been detected with targeted observation. In Fig. 2.6 and in Fig. 2.7 it is shown the flux density of the radio star classes described in the Chapter before as a function of, respectively, the frequency and the distance from the observer, after imposing the luminosities of the stellar classes found in Umana et al. (2015a). To estimate the radio stars density that we will find in EMU and how many of them will belong to the different star classes and to approach the issues arising from a so deep survey into the GP, we have started the Stellar Continuum Originating from Radio Physics in Ourgalaxy (SCORPIO; Umana et al. 2015b, hereafter paper I).

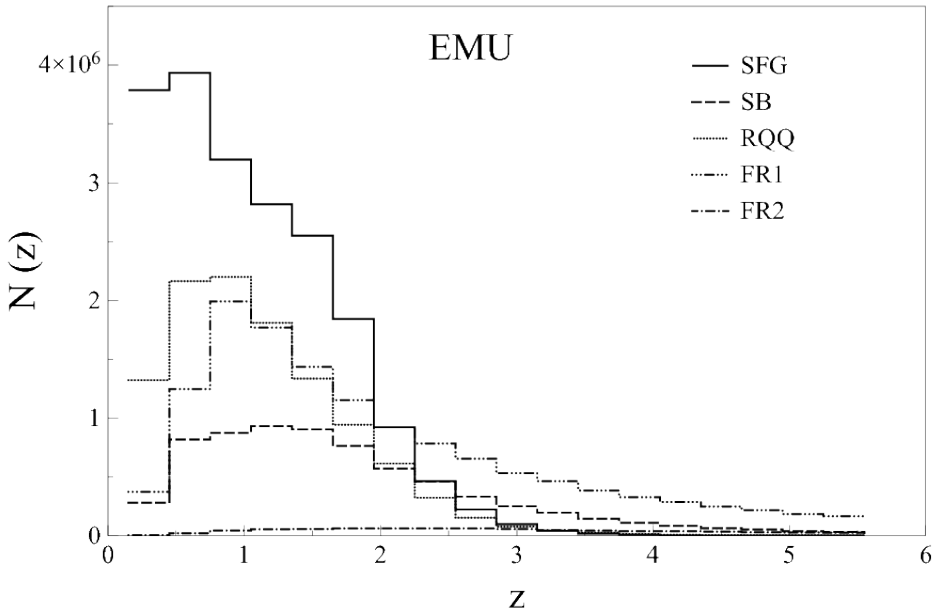

Figure 2.5: Expected redshift distribution of the EMU sources. RQQ are radio quiet quasars, FR1 and FR2 are the Fanaroff-Riley galaxies type 1 and 2.

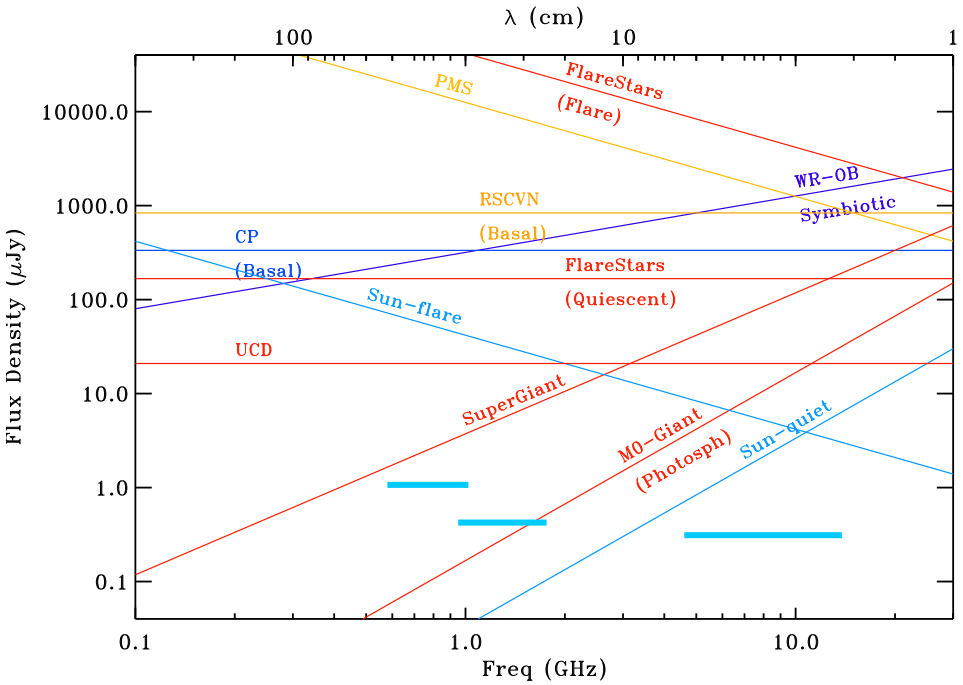

Figure 2.6: Average spectrum of common radiostars classes. The WR-OB and giant stars are assumed to be at 1 kpc, the MCP at 0.5 kpc, the RS CVn, flare stars and sun-like stars at 10 pc and the Ultra Cool Dwarf (UCD) at 20 pc. The pale blue horizontal lines represent the SKA-1 1 σ for an hour of observation at the three different bands.

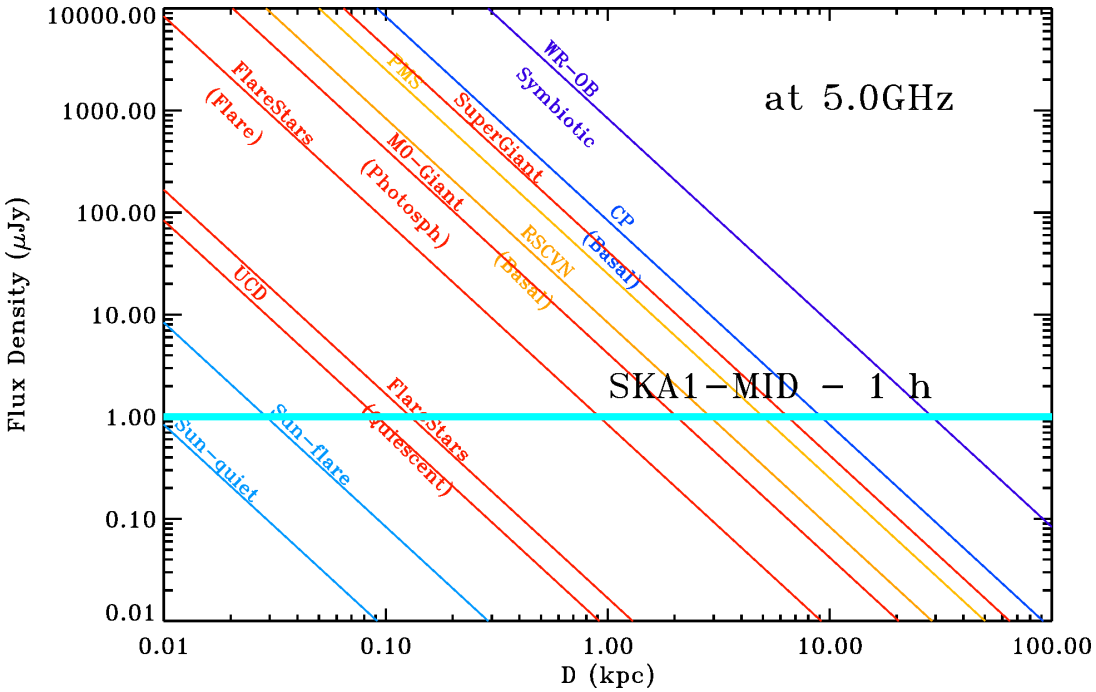

Figure 2.7: Expected flux of common radio stars classes versus their distance from the Earth at 5 GHz. The pale blue horizontal line represents the SKA1 1σ 1-hour observation.

Chapter 3

How many radio stars can we detect?

The next years are going to be crucial for radio astronomy, with several new telescopes that will start working, e. g. the Square Kilometre Array (SKA), the Australian SKA Pathfinder (ASKAP) and MeerKAT. These instruments will be capable of surveying large areas of the sky with high sensitivity, discovering a lot of new radio sources (e.g. the Evolutionary Map of the Universe, EMU, survey will detect 70 millions of galaxies, Norris et al. 2011), and, among them, a lot of radio stars. A method to estimate the number density of radio stars is an application of the Besançon model (Robin et al., 2003) to evaluate how many stars per square degree there are in our Galaxy in a given direction. In this chapter we present the results.

3.1 Modelling the Milky Way

This section is based on Mihalas & Binney (1981) and Robin et al. (2003). When we look at the sky with our naked eye we can see a fairly uniform distribution of bright stars over the entire sky and a quite uniform light coming from a plane, the Galactic Plane, caused by billions of fainter stars. We can describe this distribution quantitatively using the star counts. Let $A(m, l, b, S)$ be the number of stars of spectral type S at apparent magnitude m, per unit magnitude interval, per square degree, in galactic coordinates (l, b). We can also determine an integrated star count $N(m, l, b, S)$, the cumulative number of stars, per square degree, having apparent magnitudes less than or equal to m. These quantities are observable and are very important for the construction of the Milky Way model. Our ultimate objective is to determine the space density $\nu(r, l, b, M, S)$ (stars pc^{-3}) of stars of absolute

magnitude M and spectral type S at distance r from the Sun, in the direction selected by galactic coordinates (l, b). For the sake of brevity we shall drop the variables l and b in our notation, every other analysis will be carried out for a definite field with a specific l and b. Assuming that $\nu(r, M, S)$ can be represented as the product of two factors $D_S(r)$ and $\Phi(M, S)$, we can write:

$$\nu(r, M, S)\, dM dV = \Phi(M, S)\, dM D_S(r)\, dV \tag{3.1}$$

where dV is a volume element, dM is an increment of absolute magnitude, $D_S(r)$ is called the relative density function and it represents the density of stars of spectral type S at distance r and $\Phi(M, S)$ is the luminosity function and it gives us the actual number of stars having absolute magnitude M and spectral type S per cubic parsec in the solar neighbourhood. We can also define the general luminosity function

$$\Phi(M) \equiv \sum_S \Phi(M, S) \tag{3.2}$$

This function describes the stellar composition of a unit volume in the solar neighbourhood at the present time. However the distribution of stars over luminosity implied by $\Phi(M)$ is not an accurate representation of the relative frequencies with which these stars are formed. This is caused by the rapid decrease of the main-sequence lifetime $\tau_{MS}(\mathcal{M})$ of stars with increasing mass $\mathcal{M}$. Therefore, below some critical mass $\mathcal{M}_0$, stars will persist on the main sequence for periods longer than τ_G, the age of our Galaxy, while stars with a mass exceeding $\mathcal{M}_0$ will evolve as white dwarf or explode as supernova. This effect leads to a great abundance of low-mass, faint stars. To describe the rate of star creation it was introduced by Salpeter (1955) an initial luminosity function $\Psi(M_V)$ which gives the relative numbers of stars formed, per unit magnitude interval per unit volume as a function of M_V.

In the broadest term, our Galaxy comprises two main structural elements, a spheroidal component and a disc (see Fig. 3.1 for a complete scheme). The first one can be thought of as being an approximately axially symmetric system that can be divided into several subcomponents: the nucleus, the innermost part of the Galaxy, with a size of $\sim$ 3 pc, the bulge, $\sim$ 3kpc in size, and the extensive halo around our Galaxy, that can extend to a radius of $\sim$ 30 kpc or more. The disc can be divided into two subcomponents: the thin disc, that is an extremely thin (about 200 pc thick), flat system extending in the Galactic Plane from the center to a radius of 25 $\sim$ 30 kpc and the thick disc that is about 2 kpc thick but it is less dense.

The spheroidal component is almost gas and dust free. The stars that are part of it are usually metal-poor subdwarfs and RR Lyrae variables. Both the

star density and the metallicity rise considerably toward the Galactic centre, leading scientists to divide the spheroidal stellar population into a sequence of subpopulations, such as bulge-component stars, intermediate spheroidal-component stars and halo-component stars. They have low orbital velocity around the galactic centre and high eccentricity. The disc is usually divided into two subcomponents, the thin disc and the thick disc. The thin disc component is constituted by: interstellar dust and gas, young metal-rich stars, which are concentrated on the spiral arms and older metal-rich stars which have a smooth distribution throughout the disc. Thin disc stars have high rotation velocity and almost perfectly circular orbit. The thick disc is composed of older stars and there are several theories about its genesis:

1. it comes from the heating of the thin disc (Steinmetz, 2012);
2. more energetic stars migrate outwards from the inner galaxy to form a thick disk at larger radii (Schönrich & Binney, 2009);
3. it is a result of a merger event between the Milky Way and another dwarf galaxy (Bensby & Feltzing, 2010);
4. the disc forms thick at in the first ages of the universe with the thin disc forming later (Brook et al., 2004).

The thick disc stars are poorer in metals than the thin disc ones and they are studied for determining the chemical composition of the Galaxy in early time.

Models divide stars into several populations, corresponding to their position in the different elements of the Galaxy, each one described with several parameters such as age, metallicity $\left[\frac{Fe}{H}\right]$, initial mass function (IMF), star formation rate (SFR), density law, local mass density, etc.

3.2 The Besançon model

In this section we discuss the Besançon model (Robin et al., 2003). They divide stars into 4 populations: disc, thick disc, stellar halo and bulge. To compute the population synthesis model, the stellar content at each epoch has been extracted from standard parameters such as the IMF, SFR and a set of evolutionary track (see Table 3.1).

The thin disc population was assumed to evolve in 10 Gyr, life-span derived from the white dwarf luminosity function with an accuracy of about 15% (Wood & Oswalt, 1998). Sets of IMF slopes and SFRs have been tentatively assumed and tested against star counts. The luminosity function

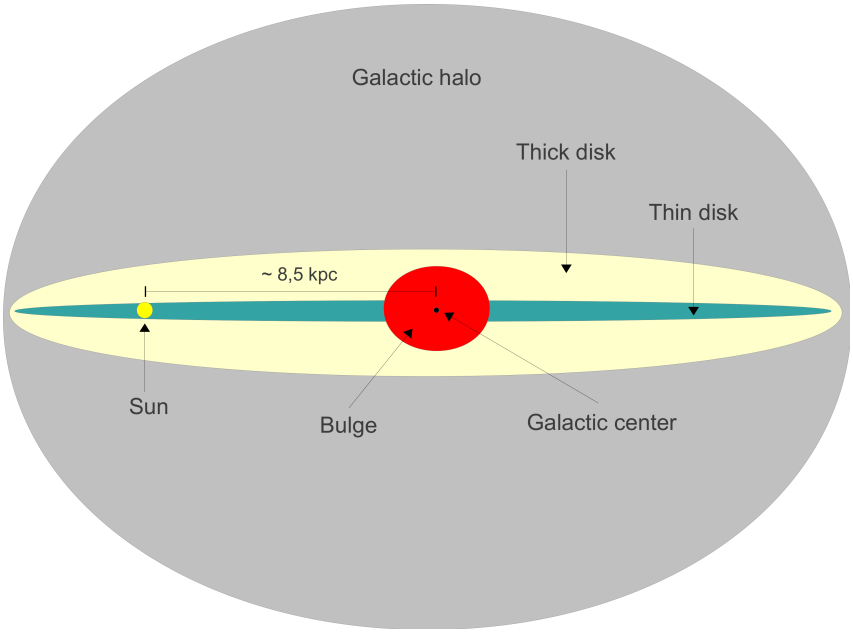

Figure 3.1: Components of our Galaxy

	Age(Gyr)	$\left[\frac{Fe}{H}\right]$ (dex)	$\frac{d[Fe/H]}{dR}$	IMF	SFR
Thin Disc	0-0.15	0.01 ± 0.12			
	0.15-1	0.03 ± 0.12			
	1-2	0.03 ± 0.10		$dN/d\mathcal{M} \propto \mathcal{M}^{-\alpha}$	
	2-3	0.01 ± 0.11	-0.07	$\alpha = 1.6$ for $\mathcal{M} < 1\mathcal{M}_\odot$	constant
	3-5	-0.07 ± 0.18		$\alpha = 3.0$ for $\mathcal{M} > 1\mathcal{M}_\odot$	
	5-7	-0.14 ± 0.17			
	7-10	-0.37 ± 0.20			
Thick disc	11	-0.78 ± 0.30	0.00	$dN/d\mathcal{M} \propto \mathcal{M}^{-0.5}$	one burst
Stellar halo	> 11	-1.78 ± 0.50	0.00	$dN/d\mathcal{M} \propto \mathcal{M}^{-0.5}$	one burst
Bulge	10	0.00 ± 0.40	0.00	$dN/d\mathcal{M} \propto \mathcal{M}^{-2.35}$ for $\mathcal{M} > 0.7\mathcal{M}_\odot$	one burst

Table 3.1: Age, metallicity, radial metallicity gradient, initial mass function and star formation rate of the stellar components.

derived by the data of the Hipparcos mission (Perryman et al., 1997) constrained the following parameters:

1. The IMF is modeled by a broken power law (see Table 3.1). At high masses the slope of the function $dN/d\mathcal{M} \propto \mathcal{M}^{-\alpha}$ is assumed to be $\alpha = 3$, steeper than the Salpeter assumption, and it is determined by Haywood, Robin, & Creze (1997), while at low mass the assumption $\alpha = 1.6$ was chosen to better fit the Jahreiß luminosity function (Jahreiss, 2003);

2. new constraints on the local kinematics made them choice the age-velocity dispersion relation from Gomez et al. (1997);

3. the local density of interstellar matter is set to $0.021 M_\odot\,pc^{-3}$ from the Dame (1993) observation of the local surface density of HI+H_2, which leads to a total local mass density of $0.076 \pm 0.015 M_\odot\,pc^{-3}$ as in Crézé et al. (1998).

As already stated, there are several thick disc formation scenario theories. A formation by a merger event was assumed for this model, which explains the observed properties of this population: the accreting body heats up the stellar population previously formed in the disc making a thicker population with larger velocity dispersion. The thick disc abundances are intermediate between the stellar halo and the thin disc. They also assumed a single epoch of star formation, that cannot exceed 1 Gyr and that took place 11 Gyr ago.

The stellar halo and the Bulge are distinct in the model construction but they may be related in their formation scenario. The most significant difference in the model between the two populations is the abundance distribution. In fact, while halo stars are assumed to be metal-poor, the bulge stars, despite being $\sim$ 10 Gyr old, have a higher metal concentration. To have a more detailed description of the model see Robin et al. (2003).

3.3 Radio stars counts

In order to estimate the number of radio stars that can be detected with the new surveys, we used the Besançon model, which gives us the number of stars of a given spectral type, at distance r from the Sun, for the direction (l, b). While its purpose is to simulate an optical stellar field, we want to simulate a radio one. To achieve this goal, given that the Galaxy is optically thin at radio wavelengths, we set the diffuse emission parameter to $A = 0$ and, to collect all the stars in a given direction, we imposed 30 as the faintest magnitude to detect. Among all the stars that can emit in radio we decided

to investigate only the most common ones: the M stars, the OB stars and the MCP stars. We will also discuss the RS CVn binary stars but we will not use the Besancçon model for that. To show our results, we assume a quantity $N(S)$ that is defined as the number of source per square degree having a flux that exceeds S and we plot the $\log N$-$\log S$ distribution figure.

3.3.1 OB and Wolf-Rayet stars

The star formation, as explained before, is a process localised in the thin disc. Stars can move from the thin disc but it is a really long process. OB and Wolf-Rayet stars are intrinsically bright and quite young among the stars, so we supposed the distribution to be anisotropic, with almost all the stars lying in the GP (Mihalas & Binney, 1981). We set the maximum distance along the GP to be 20 kpc. We proceeded to simulate the number of stars of each spectral type and luminosity class from O4 to B3 (see Table 3.2 for the used parameters), dividing the GP longitudinally in 60 degrees interval and latitudinally in $-1 < b < 1$, $1 < b < 3$, $3 < b < 23$, assuming that we should have a similar star density at opposite latitude. We assumed the OB stars to emit radio waves because of the free-free mechanism in their wind. OB stars have high values of mass loss caused by their radiation pressure Garmany & Conti (1984):

$$\log \dot{M} = -6.2 + 1.6\,(L/L_{\odot} - 5) - 0.5 \log\left(M/M_{\odot}\,(1-\Gamma)\right) \tag{3.3}$$

where L is the optical luminosity of the star, M the mass and $\Gamma = \frac{\sigma_e L}{4\pi G M c}$ is the ratio of stellar luminosity to the Eddington limit, σ_e is the cross section of the electron, G and c are respectively the gravitational constant and the speed of light. $\dot{M}$ is expressed in $\mathrm{M}_{\odot}\ \mathrm{yr}^{-1}$. The mass loss generates an ionized wind around the star which has a density proportional to r^{-2} (assuming the wind velocity constant and a spherical symmetry) and that emits as in Panagia & Felli (1975):

$$\begin{aligned} S \;&= 5.12 \left(\frac{\nu}{10\,\mathrm{GHz}}\right)^{0.6} \left(\frac{T_e}{10^4\,\mathrm{K}}\right)^{0.1} \left(\frac{\dot{M}}{10^{-5}\,M_{\odot}/y}\right)^{\frac{4}{3}} \\ &\left(\frac{\mu}{1.2}\right)^{-\frac{4}{3}} \left(\frac{v_{\mathrm{exp}}}{10^3\,\mathrm{km\,s^{-1}}}\right)^{-\frac{4}{3}} \bar{Z}^{\frac{2}{3}} d_{\mathrm{kpc}}^{-2} \end{aligned} \tag{3.4}$$

where ν is the frequency, M is the mass of the star, d_{kpc} is the distance in kpc, μ and $\bar{Z}$ are the average atomic number and the average charge of the wind particles and v_{exp} is its expansion velocity. S is expressed in mJy.

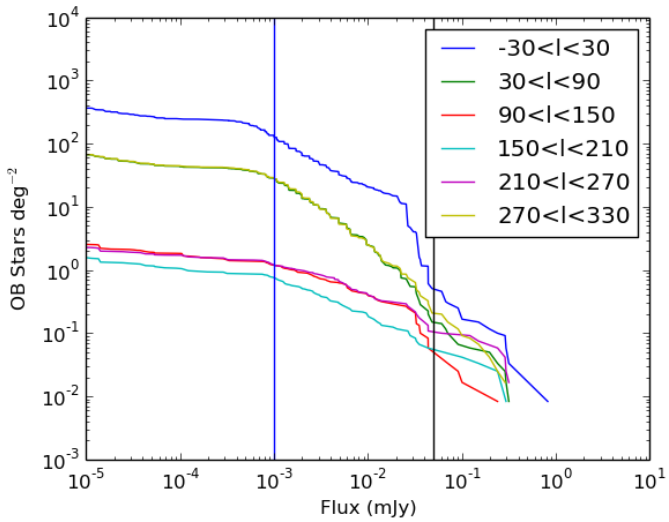

Figure 3.2: $\log N$-$\log S$ distribution for a galactic latitude $-1 < b < 1$ at different galactic longitude. The black line is at 50 μJy, the EMU sensitivity, while the blue one is at 1 μJy, the SKA-1 25-hours sensitivity.

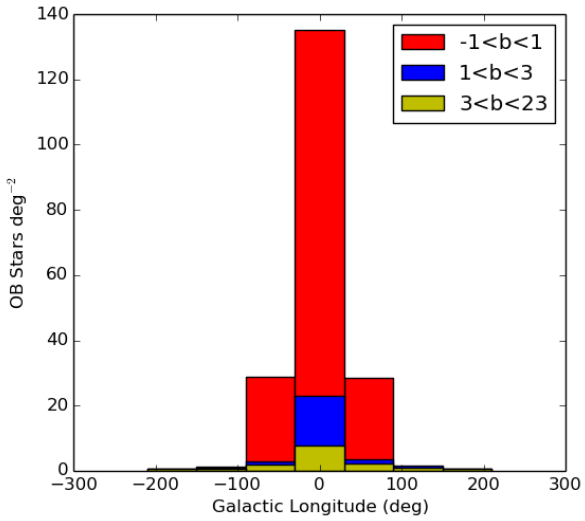

Figure 3.3: Density of OB stars with a flux greater than 1 μJy for $-1 < b < 1$, $1 < b < 3$ and $3 < b < 23$ with respect to galactic longitude.

SP	Teff (K)			Mv				$L/L_\odot$				$Mass/M_\odot$
	ZAMS-V	III	I	ZAMS	V	III	I	ZAMS	V	III	I	
O4	50000	47500	45000	−6.1	−6.1	−6.3	−6.5	6.11	6.11	6.12	6.13	35
O5	47000	44500	42000	−5.6	−5.8	−6.0	−6.4	5.83	5.92	5.93	6.00	32.7
O5.5	44500	42500	40000	−5.2	−5.5	−5.8	−6.3	5.60	5.74	5.78	5.89	31
O6	42000	40000	38000	−4.9	−5.3	−5.6	−6.3	5.40	5.56	5.63	5.82	29.5
O6.5	40000	38000	36000	−4.5	−5.0	−5.5	−6.3	5.17	5.37	5.50	5.75	29
O7	38500	36500	35000	−4.2	−4.8	−5.5	−6.3	5.00	5.24	5.45	5.72	28.3
O7.5	37500	35500	34000	−4.1	−4.6	−5.5	−6.4	4.92	5.11	5.41	5.73	26
O8	36500	34500	33000	−3.9	−4.5	−5.5	−6.5	4.81	5.05	5.38	5.74	25.2
O8.5	35500	33500	32000	−3.8	−4.4	−5.5	−6.6	4.73	4.97	5.35	5.75	23
O9	34500	33000	31000	−3.7	−4.3	−5.5	−6.7	4.66	4.90	5.34	5.76	22.6
O9.5	33000	31500	30000	−3.6	−4.2	−5.5	−6.7	4.58	4.82	5.30	5.73	20
B0	30900	29300	28000	−3.3	−4.0	−5.0	−6.6	4.40	4.68	5.03	5.63	17.8
B0.5	26200	25000	23600	−2.8	−3.5	−4.3	−6.6	4.04	4.31	4.57	5.48	14
B1	22600	21500	20400	−2.3	−2.9	−3.8	−6.6	3.72	3.95	4.27	5.32	11.7
B2	20500	19500	18500	−1.9	−2.5	−3.6	−6.8	3.46	3.70	4.09	5.28	10.0
B3	17900	17000	16100	−1.1	−1.7	−3.1	−6.8	3.02	3.24	3.75	5.20	7.32

Table 3.2: Typical OB stars parameters from Panagia (1973). ZAMS is the zero main sequence, V, III and I are the luminosity class of dwarf, giant and hypergiant.

In Fig. 3.2 the $\log N$-$\log S$ distribution of OB stars along the Galactic Plane ($-1 < b < 1$) is shown, while in Fig. 3.3 the number of stars with a flux greater than 1μJy (the sensitivity of 25-hours SKA-1) versus l at different b at 5 GHz is shown. As expected, the number of OB stars decreases rapidly going away from the Galactic Centre. Notice that we are taking into account the wind radio emission of the OB stars, however a lot of them ($\sim 20\%$ of the O stars) are embedded in nebulae, so what we will see are HII regions and not stellar winds. Is it possible for the stellar wind to completely absorb the UV radiation of a OB star and to block the formation of an HII region, or at least diminish its area? We will consider a typical O4V star and compute how many photons its wind will block. We know that $\dot{M} = 4\pi r^2 \rho v$, where ρ is the density of the wind and v its velocity, so we have:

$$\rho = \frac{\dot{M}}{4\pi r^2 v}$$

Assuming $v = 1000$ km s^{-1} and $\dot{M} = 10^{-5}\,\mathrm{M}_\odot$ we will have $\rho \approx 6 \cdot 10^9$ protons cm^{-3} at $r = 10R_*$, where $R_* = 10\mathrm{R}_\odot$. The number of absorbed photons is $N_r = \beta_r \rho^2$, so $N_r \approx 10^7$ photons cm^{-3} s^{-1} and the entire surface will absorb $n_r = N_r \cdot 4\pi r^2 = 6.8 \cdot 10^{33}$ photons cm^{-1} s^{-1}. In total we will have

$$n_r(r) = 6.8 \cdot 10^{33} \left(\frac{10R_*}{r}\right)^2 \Rightarrow N_{\mathrm{tot}} = \int_{2R_*}^{\infty} N(r)\, dr$$

so $N_{\mathrm{tot}} = 2.4 \cdot 10^{47}$ photons s^{-1}, negligible with respect of the $\sim 10^{50}$ photons s^{-1} emitted by the star.

3.3.2 MCP stars

MCP (or CP2) stars, as OB and Wolf-Rayet, are intrinsically bright and quite young, so we supposed the distribution to be anisotropic, with almost all the stars lying in the GP (Mihalas & Binney, 1981). Only 25% of all the MCP emits in radio wavelength (Leone, Trigilio, & Umana, 1994) so, after simulating the number of main sequence stars of each spectral type between B8 and A7, the fraction of them supposed to be MCP are reported in Table 3.3 and their 25% are assumed to be radio emitters. Assuming a typical MCP radio luminosity of $10^{16.8 \pm 0.9}$ erg s^{-1} Hz^{-1} (Drake et al. 1987; Linsky, Drake, & Bastian 1992) at 5 GHz, we derived the expected $\log N$-$\log S$ distribution for CP stars in Fig. 3.4 and the spatial distribution at a 1μJy/beam sensitivity in Fig. 3.5.

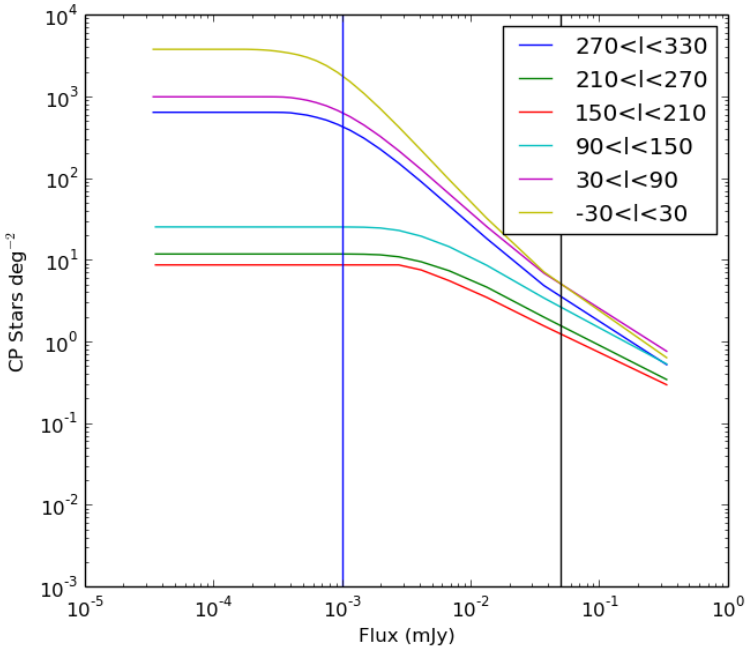

Figure 3.4: $\log N$-$\log S$ distribution for a galactic latitude $-1 < b < 1$ at different galactic longitude. The black line is at 50 μJy, the EMU sensitivity, while the blue one is at 1 μJy, the 25-hours SKA-1 sensitivity.

Spectral Type	N_{tot}	MCP	Percentage of the total
B8-B9	1916	327	17%
A0-A1	2014	191	9%
A2-A3	1728	58	3%
A4-A5	650	6	1%
A6-A7	303	16	5%

Table 3.3: Number of total stars N_{tot} and number of MCP at every spectral types in the Catalano & Leone (1994) sample.

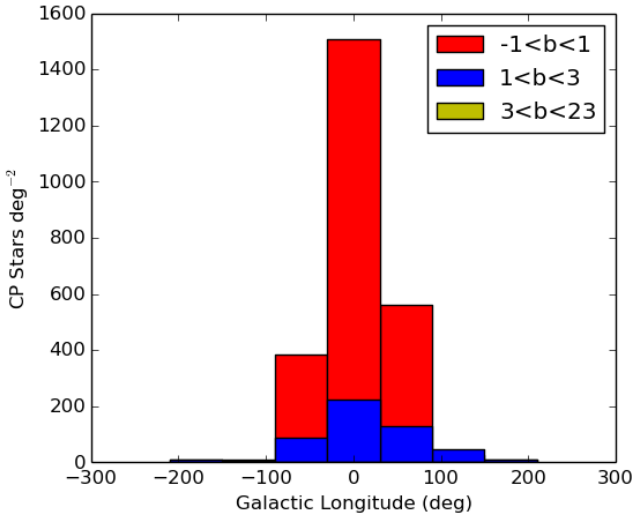

Figure 3.5: Density of MCP stars with a flux greater than 1 μJy for $-1 < b < 1$, $1 < b < 3$ and $3 < b < 23$ with respect to galactic longitude.

3.3.3 Flare stars

Main sequence M stars are faint thermal emitters and they can be detected in radio only if they are extremely close. However a fraction of them are flare stars. Flares are sudden flash of brightness observed on stars. They are burst event affecting all the layer of the stellar atmosphere. The high brightness is caused by the interaction of the particles accelerated by the reconnection of magnetic field lines with the magnetic field or with the stars itself. We assume the typical luminosity of a flare to be 10^{15} erg s^{-1} Hz^{-1} (Umana et al., 2015a) so, knowing that

$$d_{\mathrm{kpc}} = \sqrt{\frac{W * 8.35 \cdot 10^{-19}}{F}}$$

, where W is the luminosity in erg s^{-1} Hz^{-1}, F is the measured flux density in mJy and d_{kpc} is the distance in kpc, we can fix the maximum distance at which we can observe flare stars. Assuming a minimum flux of 1 μJy we can derive $d_{\mathrm{max}} \sim 0.9$ kpc so we imposed a maximum distance of 1 kpc to the Besançon model.

To discriminate between flare and inactive stars, in Hawley et al. (2014) they define active flare stars as the ones with a flare up time of $\sim$30%, while inactive stars have a flare up time of $0.01 \sim 1\%$. Weisenburger et al. (2013)

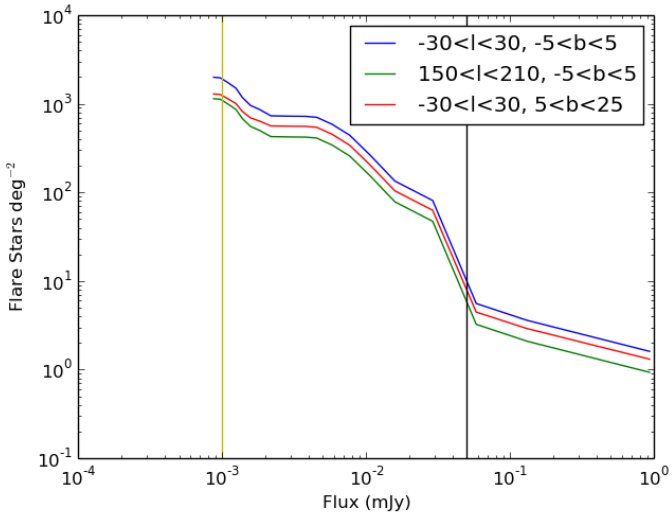

Figure 3.6: $\log N$-$\log S$ distribution at different galactic latitude and longitude of flare stars. The yellow line is at 1 μJy, the 25-hours SKA-1 sensitivity.

pointed out that the stars around M0-M2 are inactive, while 37% of the M3-M4 stars and 60 $\sim$ 70% of the M5-M8 ones are active. Given these assumptions we extracted the $\log N$-$\log S$ distribution in Fig. 3.6. We notice that the sky is almost completely isotropic if we do not have a sensitivity better than 1 μJy, so we expect a roughly constant distribution of M stars in every direction.

3.3.4 RS CVn

To estimate the number of RS CVn stars we will detect with the coming telescopes, we extracted the number of RS CVn in the solar neighbourhood from Eker et al. (2008). The catalogue seems rather complete up to a 50 pc distance, containing 149 RS CVn. This is shown in Fig. 3.7 where we can appreciate the rise in number of stars per bin until the 50-pc limit. That limit must be seen as a lower limit because there can be missing detections. From this data we can suppose a $\sim$ 350 000 sources kpc^{-3} density. To calculate the number of expected detection we assumed a homogeneous distribution in the Galactic Plane and a typical flaring RS CVn luminosity of 10^{16} W (Seaquist 1993; Umana et al. 2015a), that leads to detect all the sources up to 500 pc for EMU and 6 kpc for SKA-1. We need the volume of the pyramid that it is formed between us and a base of 1 deg^2 area 6 kpc away from us

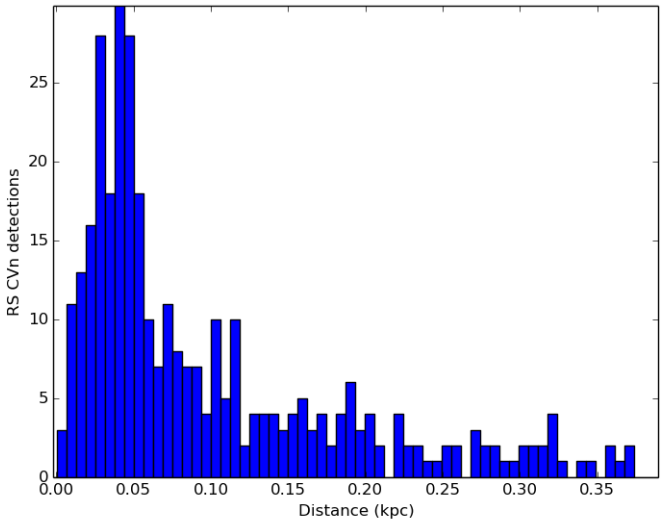

Figure 3.7: Number of RS CVn in the Eker et al. (2008) catalogue at each 0.016 kpc wide distance bin.

to multiply this value for the local density and know how many RS CVn we should expect in SKA-1. The volume of that pyramid is, considering that 1 deg at 6 kpc is 50 pc in linear size, $V = \frac{1}{3}A \cdot d = 0.0025$ kpc^3 where A is the area of the base and d the distance. Multiplying this result for the local density of RS CVn we obtain 875 RS CVn deg^{-2} to be visible during flares. The results considering other sensitivities and at different values of flare up time are shown in Table 3.4. In Umana, Trigilio, & Catalano (1998) the authors indicate a typical flaring occurrence of $\lesssim 20\%$ so we will consider, conservatively, the most probable value to be $\sim 10\%$.

3.3.5 Results

From the work described in this chapter, summarised in Table 3.5, 3.6 and 3.7 we can get the following conclusion:

- at a 50μ-Jy threshold (the EMU sensitivity), we should detect about the same amount of MCP, OB and RS CVn stars and a much higher number of Flare Stars while, at higher sensitivity, the MCP stars will dominate together with Flare Stars (at least along the direction of the Galactic Centre);

	Detection limit of the survey		
Flaring occurrence	1μJy	5μJy	50μJy
1%	8.7	2.3	0.04
10%	87	23	0.4
100%	870	230	4

Table 3.4: Expected number of RS CVn binaries detected per square degree on the Galactic Plane at 1, 5, and 50 μJy, based on the work described in this chapter.

	OB		
	1μJy	5μJy	50μJy
$150 < l < 210$	0.8	0.33	0.05
$210 < l < 270$ and $90 < l < 150$	1.2	0.6	0.07
$30 < l < 90$ and $270 < l < 330$	29	5.2	0.2
$-30 < l < 30$	136	32	0.5

Table 3.5: Expected number of OB stars detection per square degree at different Galactic Longitude, fixing the Galactic Latitude to $-1 < b < 1$ based on the work described in this chapter at 1, 5 and 50 μJy.

	MCP		
	1μJy	5μJy	50μJy
$150 < l < 210$	8.7	6.7	0.05
$210 < l < 270$and $90 < l < 150$	18	12	0.07
$30 < l < 90$ and $270 < l < 330$	529	82	0.24
$-30 < l < 30$	1800	160	0.5

Table 3.6: Expected number of MCP stars detection per square degree at different Galactic Longitude, fixing the Galactic Latitude to $-1 < b < 1$ based on the work described in this chapter at 1, 5 and 50 μJy.

	M		
	1μJy	5μJy	50μJy
every direction	1500	170	7.6

Table 3.7: Expected number of M stars detection per square degree based on the work described in this chapter at 1, 5 and 50 μJy.

- given that EMU will detect ~ 70 millions galaxies (Norris et al., 2011) it means $\sim$ 2200 galaxies deg^{-2}, so the stars will be $\sim$ 3 orders of magnitude less than the extra-galactic sources even in the Galactic Plane. This, given that the rise in MCP number will be way larger than the rise in galaxies with sensitivity, will be different with SKA-1;
- with SKA-1, we will detect all the MCP of the Milky Way;
- M stars detections will be almost isotropic, meaning that, in the SKA-1 maps, their number will pollute the extra-galactic population in every direction;
- SKA-2 will not improve the detection number by too much, meaning that we will not need to wait for it to have better science. This is not true for RS CVn binaries though.

This simulation shows how big of an improvement SKA-1 will be for the radio star science, starring a $\sim$ 2000 times increase in the number of detected stars. Most of them will not be seen in optical because of extinction, so we should develop ways different to the optical matches to distinguish stars from the other source and to classify them. Knowing that in the Galactic Plane lot of them will be MCP stars, the Stokes V map will be really important but, assuming a circular polarisation of the total flux around $\sim$ 20%, we will be able to measure the Stokes V only on 25σ source, so on $\sim$10% of the MCP stars. We need to test new ways to discriminate the galactic and extra-galactic sources and this was one major scientific driver of SCORPIO.

Chapter 4

Data observations

As anticipated in the Introduction, one of the approaches that we are following to estimate the radio star density is the observational one. In particular, the main goal is to determine how many stars can be detected per square degree in the radio wavelengths and the occurrence of the various stellar classes (see Section 1.1.3). This wants also to be a study of the stellar emission free from the target bias. To achieve all these goals we designed the SCORPIO (Umana et al. 2015b, hereafter paper I) project to be a blind radio survey of a $2 \times 2\,\mathrm{deg}^2$ patch of the GP, carried out between 1.1 and 3.1 GHz, using the Australian Telescope Compact Array (ATCA). Technical details on observation strategy and data reduction of SCORPIO data are the main topic of this chapter.

4.1 SCORPIO

SCORPIO wants to collect as many information about radio stars emission as possible. To achieve that we need to select a field that needs to satisfy the following requirements :

1. it shall contain a large number of stars in respect of the other regions of the GP, with a good spread in different classes of stellar objects thought to be radio emitters;

2. it shall contain sources already classified as radio emitters to enable verification of the data;

3. it shall have been already observed in other spectral regions to gather additional information in order to help with the classification of new, unexpected objects or in order to allow complete studies for the classified objects.

Furthermore SCORPIO has also technical goals. As reported in the previous section, we want to test what kind of issues we are going to face in the GP part of EMU. In particular:

1. issues due to the complex structure present in the GP;
2. issues due to the presence of variable sources;
3. issues due to the diffuse emission that dominate the GP;
4. issues regarding the identification of different populations (e.g. Galactic and extra-galactic).

The selected field is a 2×2-deg^2 region of the sky centred at Galactic coordinates $l = 344.25$, $b = 0.66$, in the GP. Because our aim is to get statistical information from the survey, we choose this sky patch only on the a priori knowledge that it satisfies the requirements listed at the beginning of this section. There are eight open star clusters and stellar associations inside the SCORPIO field. Furthermore, part of the field has already been surveyed in the mid-IR by Spitzer (Benjamin et al. 2003; Carey et al. 2009)) and by Herschel Hi-GAL survey (Molinari et al., 2010) and will be covered by CORNISH south (CORNISH south is a high resolution survey of the GP (PI: M. Hoare) being carried out with ATCA at 6 and 9 GHz with a target rms noise of 0.18 mJy beam^{-1}).

SCORPIO was anticipated by a pilot experiment, that took place in 2011, from April 21 to 24. This experiment covered about one quarter of the whole field, namely a 0.5×2 deg^2 (actually larger at the lowest frequencies) region centred at $l = 343.5$, $b = 0.66$. The field was observed in the ATCA mosaic mode, using an 8.8 arcmin spacing hexagonal grid, requiring a total of 38 pointings (paper I).

The SCORPIO project took a total of 312 hours of observing time, in different array configurations. We reached an rms of 25 μJy beam^{-1} and a resolution of 9×5 arcsec (see the next sections for more details and an exhaustive discussion on the data reduction).

4.2 Interferometry

The resolution of a telescope is $\sim 1.22\frac{\varnothing}{\lambda}$, where $\varnothing$ is the diameter of the telescope and λ is the observed wavelength. The radio wavelengths are ~ 7 orders of magnitude larger than the optical ones so, while an optical telescope reaches the $1''$ resolution as long as its diameter is larger than ~ 10 cm, a radio telescope observing at 16 cm (2.1 GHz) needs a diameter of about

26 km. To overcome this issue, we can take advantage of a property of the output of a radio telescope. While an optical telescope gives us the amplitude of the electromagnetic field, a radio telescope measures also the phase. Thanks to this information we can correlate the signal of an array of several radio telescopes to simulate a much larger one. This technique is called interferometry and the utilised array of telescopes an interferometer. If we assume that the telescopes are located in a bidimensional surface (this is possible projecting the telescopes onto a plane), we can assume the distance between every telescope (baseline) to be $|\mathbf{r_1} - \mathbf{r_2}| = \lambda(u, v, 0)$, where $\mathbf{r_1}$ and $\mathbf{r_2}$ are the position of the two telescopes and u and v the x and y coordinates in wavelength units. The output of every baseline in an interferometer is a complex number called visibility $V_\nu(\mathbf{r_1}, \mathbf{r_2})$. This function is the Fourier Transform of brightness $I_\nu(l, m)$ and it can be inverted:

$$V_\nu(\mathbf{r_1}, \mathbf{r_2}) = \iint I_\nu(l, m)\, e^{-2\pi i(ul+vm)} dldm \tag{4.1}$$

However it is not possible to measure the visibility function in every (u, v) point because we would need an infinite number of baseline. We can introduce a sampling function $S(u, v)$ that is defined equal to 0 where we do not have measurements, 1 otherwise. The observed visibility function is $\tilde{V}(u, v) = V(u, v)\, S(u, v)$, so:

$$I_\nu^D(l, m) = \iint V_\nu(u, v)\, S(u, v)\, e^{-2\pi i(ul+vm)} dldm \tag{4.2}$$

where $I_\nu^D(l, m) = I_\nu * B$ is the "dirty" image, $*$ is the convolution operator and $B(l, m) = \int\int S(u, v)\, e^{-2\pi i(ul+vm)} dudv$ is the point spread function or dirty beam (Thompson, 1999).

From the properties of the Fourier Transform we can derive two important properties of the interferometers:

1. the spatial resolution of the derived map is proportional to $1/b_{\max}$, where $b_{\max}$ is the largest baseline of the interferometer;

2. the presence of a largest angular scale (LAS), the of the largest source of extended emission that is possible to measure with an interferometer. It is proportional to $1/b_{\min}$, where $b_{\min}$ is the shortest baseline of the interferometer.

The visibilities are actually modulated by the antennae beam (called the primary beam of the interferometer). The Field of View (FoV) of the interferometer is its primary beam, with some exception due to new technologies (the PAFs described in Section 2.2)

4.3 Deconvolution

As pointed out in Section 4.2, the Fourier transform of the visibility function is $I_\nu^D(l,m) = I_\nu * B$, the "dirty" image. The true sky brightness $I_\nu(l,m)$ can be obtained therefore by a deconvolution procedure. There are several algorithm developed to achieve this result, we will now discuss about two in particular: the CLEAN algorithm (Högbom, 1974) and the Maximum Entropy Method (MEM; Frieden 1972).

The CLEAN algorithm provides a solution to the deconvolution problem by assuming the radio source solely composed of a number of point sources in an otherwise empty region of the sky. The basic algorithm proceeds as follows:

1. find the position of the pixel with the highest absolute value in the field;
2. subtract the dirty beam multiplied by the peak value and a "gain" factor smaller than 1 (usually the default is set to 0.1) from the dirty image;
3. store the position and value of the peak subtracted in a image called model;
4. reiterate from step 1 unless there are no remaining peaks higher than a level specified by the user or if the number of iteration is larger than the maximum number specified by the user;
5. convolve the model with a "clean" beam (an elliptical gaussian fitted to the central lobe of the dirty beam);
6. add the convolved model to the residuals.

The algorithm has been improved since its development and there are many version of it (the Clark algorithm, Clark 1980; the Cotton-Schwab algorithm, Schwab 1984 ecc.). Even if it is not perfectly suitable for all the possible sky brightness distributions, in particular when it is used on extended sources, it is the most used deconvolution algorithm.

The MEM algorithm consists in a procedure that select an image that fits the data and maximise a function, called the entropy. Entropy is a function that produces a positive image with a compressed range in pixel values when maximised (Cornwell, Braun, & Briggs, 1999). The MEM algorithm needs a model image or the estimated total flux of the observed region as an input and it is usually faster than CLEAN to converge. It has some drawbacks

too, it usually fails to map point sources embedded in extended emission. In addition, while a version of CLEAN was developed to cope with multi-frequency observations, there are no versions of MEM that automatically do that.

4.4 Australian Telescope Compact Array

Figure 4.1: Four of the six ATCA dishes

The survey SCORPIO has been carried out with the ATCA. ATCA is a linear interferometer (see Fig. 4.1) oriented along the east-west axis and aperture synthesis based (observers have to take data for about 8-12 hours to have a good *uv* coverage and, therefore, a good map). It consists in 6 antennae with a diameter of 22 m. Among them, 5 can be moved on binaries and position in particular positions (stations) while one, CA06, is located 6 kilometres away from the others and its position is fixed. Thanks to this mobility, the array can be used in 17 different configurations, divided in 3 principal arrays (750m, 1.5km, 6km) (Stevens et al., 2016). ATCA operates in 5 bands, from 1.1 to 105 GHz (see Table 4.1 for details) and it produces two orthogonal linear polarisations (x and y, horizontal and vertical).

The correlator actually used in the system was installed in March/April 2009, and it is called Compact Array Broadband Backend (CABB). The output is:

1. two always available 2048 MHz continuum IF bands, with a maximum separation of 6 GHz, that can be divided into 2048×1 MHz channels or 32×64 MHz channels, with up to 16 "zoom" bands able to be placed for higher spectral resolution;

2. all polarisation parameters for all products (xx, yy, xy, yx);

3. a pulsar gating mode.

The nominal frequencies for continuum observations are: 2.1 GHz for *L*-band, 5.5 and 9.0 GHz for *C*-band, 16.7 and 21.2 GHz for *K*-band, 43.0 and 45.0 GHz for *Q*-band and 93.0 and 95.0 GHz for *W*-band.

Band Name	16cm	4cm	15mm	7mm	3mm
Band Code	L/S	C/X	K	Q	W
Frequency range(GHz)	1.1-3.1	3.9-11.0	16-25	30-50	83-105
Fractional frequency range	95%	95%	44%	50%	24%
Primary beam	42′-15′	12′-4′	2′	70″	30″
Synthesized beam	9″-3″	3″-1″	0.5″	0.2″	2″

Table 4.1: Observing parameters for the 6km array (except for the W band, for which it is assumed the H214 configuration without the CA06 antenna.) (Stevens et al., 2016).

Date	Configuration	Observation time(h)	Target
2011 April 21-24	6A	48	Pilot field
2012 June 3	6B	6	Pilot field
2012 June 3-11	6B	102	Whole field
2012 August 26-30	6A	36	Whole field
2014 February 24-28	EW367	60	Whole field
2016 January 30-February 6	EW352-367	60	Whole field

Table 4.2: Observations log.

4.5 SCORPIO observations

As introduced in Section 4.1, the SCORPIO survey was carried with ATCA in L-band between 2011 and 2016 for a total of 312 hours (see Table 4.2 for the observations log and Fig. 4.2 for the *uv* plane). The first 54 hours, performed between April 2011 and June 2012, were part of the pilot experiment (Paper I) and they were carried out, as all the hours but the last 120, in 6 kilometre configuration, to achieve the best resolution possible with ATCA. The last 120 hours were carried out in compact configuration to add the short baselines necessary to probe the shortest spatial frequencies. Since the field has an extension much greater than the primary beam of the ATCA telescope, the adopted method was the mosaicing, consisting of a series of acquisitions (pointings) whose position are spaced about half of the primary beam. We chose the pointings using the `mosgen` tool in `MIRIAD`. Giving the position of the centre of the mosaic, its width and the frequency, it generates a file containing the mosaic pointing centres. The high frequency primary beam FWHM is $\sim 16.5'$. The total number of observed pointings is 133.

The observations were conducted as follows:

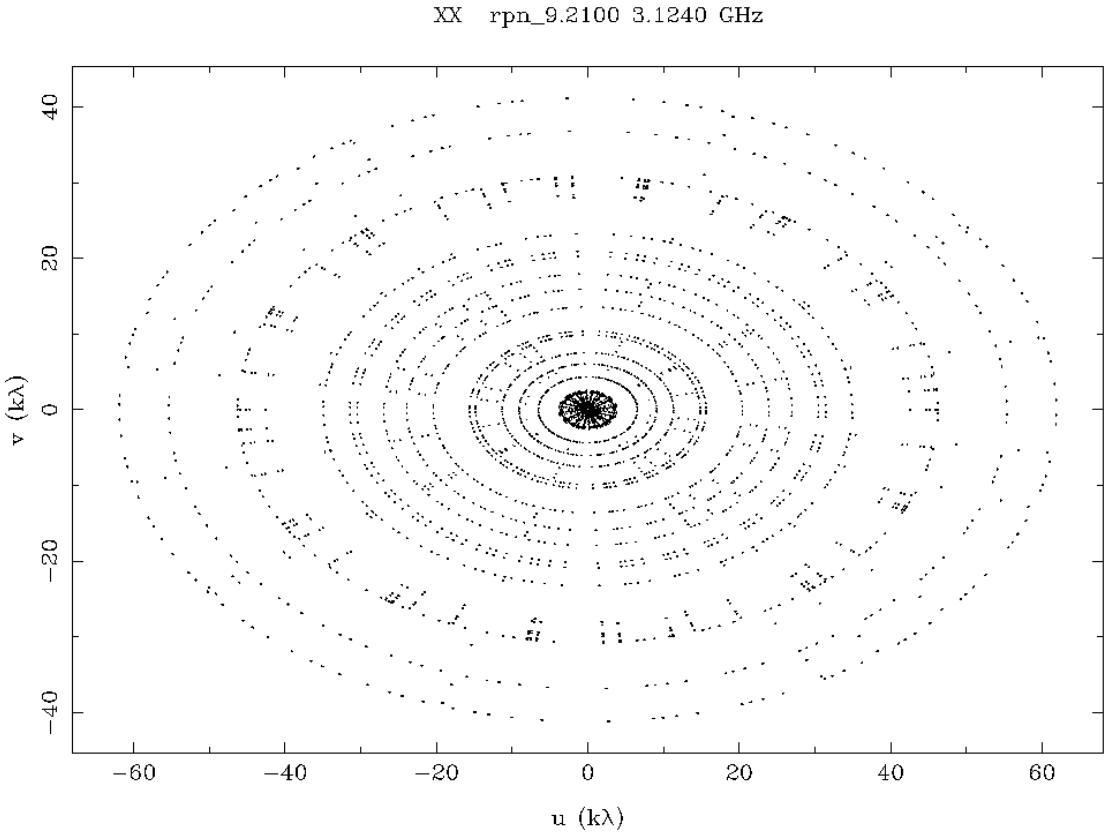

Figure 4.2: *uv* plane of a pointing of the SCORPIO observations at 3.124 GHz resulting from the sum of all the observing intervals. Notice the central part of the *uv* plane, filled by the short baseline observations.

1. acquisition of the bandpass and flux calibrator, the 1934-638 source (once a day, even during the observation when its elevation is sufficiently high);

2. acquisition of the complex gain calibrator, the 1714-397 source, for 2.5 minutes;

3. acquisition of $\sim$ 16 pointings, for 1 minute each (the total duty cycle last about 20 minutes);

4. reiteration of step 2 and 3 for different pointings until all the pointings were observed;

5. reiteration of step 2, 3 and 4 until the end of the observations.

We observed in L-band, in the frequency range 1.1-3.1 GHz, divided into 2048 1MHz-channels. A detailed description of the SCORPIO data reduction process is reported on the next section.

4.6 Data reduction

Data reduction was performed with `MIRIAD`, a radio interferometric data reduction package that includes tasks to flag, calibrate and image the data. The process described in this paragraph was carried out for each run of observation, and at the end, maps were produced after merging the *uv* data of all the days. `MIRIAD` is specifically optimised for ATCA so it is faster than other packages, such as `CASA`. Our data reduction strategy for the SCORPIO field can be divided in seven steps:

1. import the data from the uvfits format to the `MIRIAD` standard using the `atload` task;

2. split the data into the different sources observed: 1934-638, the bandpass calibrator, 1714-397, the secondary calibrator, and the 2 targets. In the case of mosaicing, the *uv* data for all the pointings are stored in one file. The task used was `uvsplit`;

3. flag the data using the task `pgflag`;

4. calibrate the phase and the bandpass of the data using `gpcal` to determines antennae gains and instrumental polarisation characteristics, `mfcal` to determine the bandpass corrections, `mfboot` to set the flux

scale, `gpcopy` to apply the calibration the phase calibrator and the targets and `gpboot` that corrects the gains comparing them between each other;

5. image and deconvolve the individual pointings using the tasks `invert`, `mfclean` and `restor`;

6. selfcalibrate the single pointings using `selfcal`;

7. mosaic the whole field using `linmos`.

The first two steps are straightforward, we simply used the tasks with the suggested options listed in the cookbook (as stated before, `atload` and `uvsplit`). The other steps are more complicated and they will be described in separate sections. Every step from the first to the fourth is applied iteratively for each single observation day so the steady-instrumentation approximation can be assumed.

4.6.1 Flagging

Typical radio data are contaminated by Radio Frequency Interference (RFI), radio emission coming from terrestrial sources, usually human-based and really strong (TV, radio trasmissions, mobile phones, etc.) that seriously contaminate the data. It is important to delete the RFIs and to do so we individuate the visibilities corrupted by the interferences and flag them as bad data point, to not be used in the data reduction. This process is called flagging.

`MIRIAD` has a lot of different flagging tasks, some of them automated (e.g. `mirflag`), some of them requiring actions (e.g. `uvflag`). We chose to use `pgflag` because it is interactive and versatile, with many methods to individuate and erase the corrupted visibilities. In Fig 4.3 we show a typical `pgflag` greyscale plot, the x axis is labelled as the channel numbers and the y axis as the time. The colour intensity represents the amplitude of the visibility. `pgflag` wants commands as input to determine what algorithm to use. The commands that we used to automatically flag our data were:

- $<$ command, to apply the SumThreshold (Offringa et al., 2010) algorithm and perform a preliminary flagging;

- b command, to "blow away the dust" (flag isolated points);

- e command, to extend the flags to all the channels, time sections or baseline that are more than 80% flagged (this value can be changed);

- b command again, to complete the flag.

The flag is applied on the two calibrators and then, after the calibration (next section) on the target data. To manually flag some channels, time intervals or baselines we used the `uvflag` task. We found low frequencies (high channels in Fig. 4.3) to be afflicted by severe RFI, so we selected 1.35-3.1 GHz as the usable frequency range. Furthermore we found the shortest baseline (baseline 4-5) on the 3-11/06/2012 to be hard to properly calibrate so we decided to flag it. This issue arose when we observed using the compact configuration array, see the next sections for more details on it.

Figure 4.3: `pgflag` user interface. In abscissa the channel number (increasing frequency toward left), in ordinate the scan numbers.

4.6.2 Calibration

An important step in the data reduction is the calibration. Data calibration includes amplitude, bandpass, polarisation and phase calibration. Raw data

are not calibrated. The bandpass depends on the frequency and it is usually stable for 12 hours, while the phase calibration depends on time and slightly on direction and weather. We chose the 1934-638 source as our bandpass and flux calibrator. It is a bright, stable source, its flux density was set to 12.31 Jy at 2.1 GHz as in Reynolds (1994). While the bandpass calibrator can occupy any position on the celestial sphere, the complex gain calibrator position must be close to the source, within few degrees since the accuracy of the calibration depends on the distance from the source to be calibrated. We chose the 1714-397 source because it is close to our field and it is a bright source (2.71 Jy at 2.1 GHz).

The data are natively calibrated for delay but not for bandpass or complex gain variations. To achieve this result, we proceeded using `MIRIAD` task as it follows:

1. we ran the `gpcal` task on the 1934-638 to to calibrate this source for complex gain variations. This permits to correct any phase variation during the observing period of the calibration in order to avoid decorrelation and loss of flux. This passage is not strictly necessary but we found it useful to have better calibrated data;

2. we subsequently ran `mfcal` on it. This task implements the bandpass and the amplitude calibration to our primary calibrator using the Reynolds (1994) flux density dependence on frequency;

3. we applied the bandpass and amplitude calibration on the 1714-397 using the `gpcopy` the `gpboot` and the `mfboot` tasks;

4. we ran `gpcal` on the 1714-397. This is the complex gain calibration that will be applied on the actual science data.

In Fig. 4.4 two calibration plots of the secondary calibrator are showed. The plot made in the compact configuration day (lower panel) presents a more scattered spectrum in some baselines. This can be caused by cross talking between antennae but, as showed in Fig. 4.5, the 1714-397 is not really a pointlike source in a clear environment. This can cause problems in the calibration since complex gain calibration assumes that there is only one point-like source in the field, causing the spread shown in the sub-plot in Fig. 4.5b. To fix this issue we decided not to include the compact configuration data on the spectral index analysis, subject of the next Chapter.

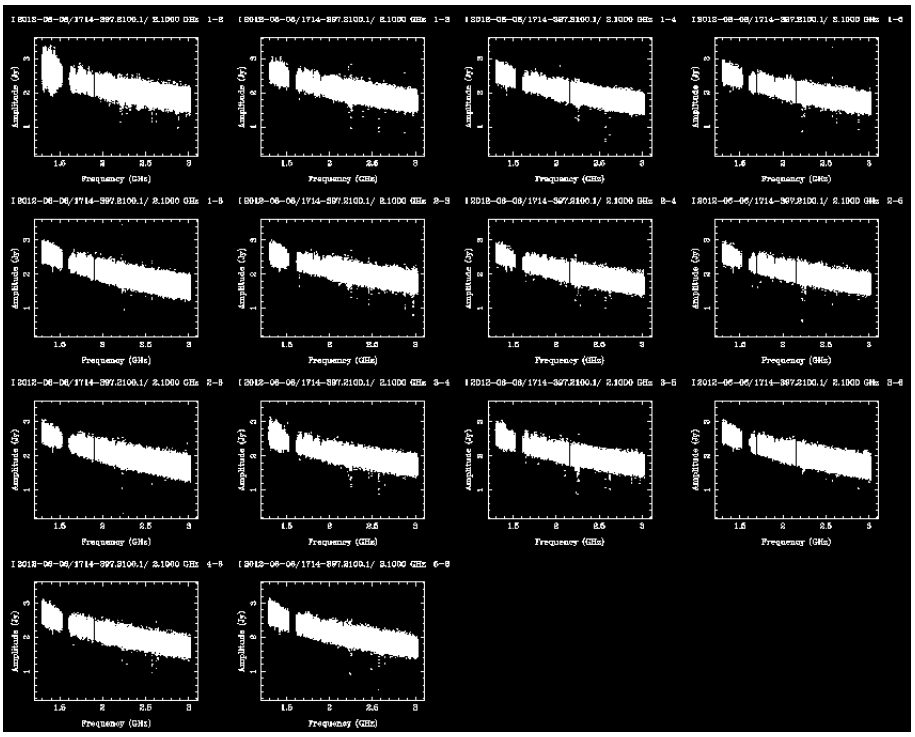

(a) 1714 bandpass with an extended configuration.

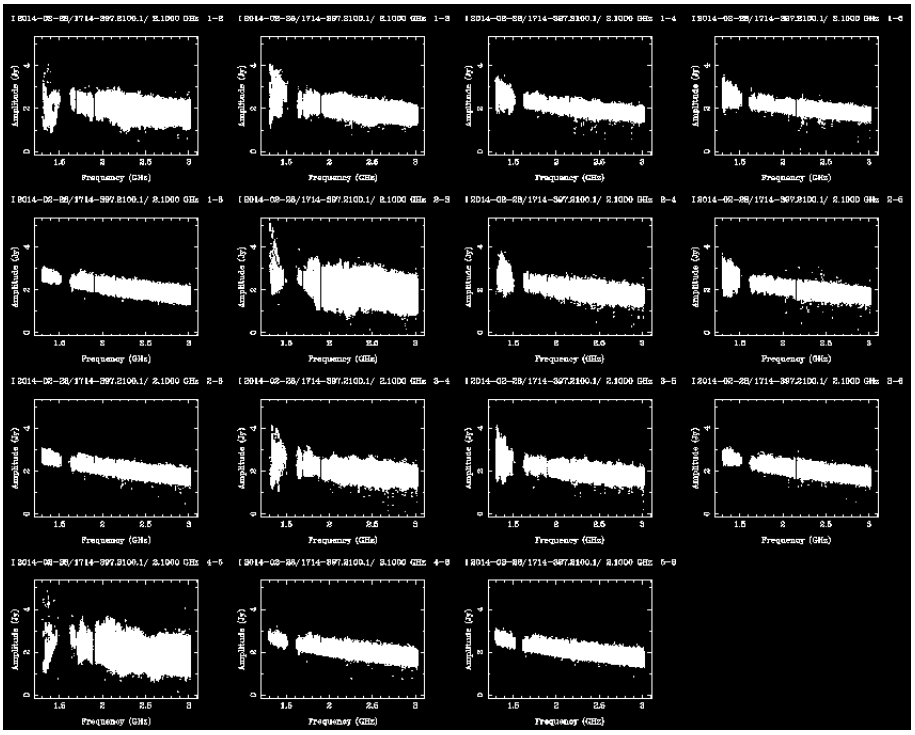

(b) 1714 bandpass with a compact configuration.

Figure 4.4: Spectra of the phase calibrator 1714-397 for all the baselines after the baselines and flux calibrations. In abscissa the frequency, in ordinate the amplitude, 0-3.5 scale in the a subplot, 0-4.5 in the b one. Notice the flagged 4-5 baseline on the extended configuration plot.

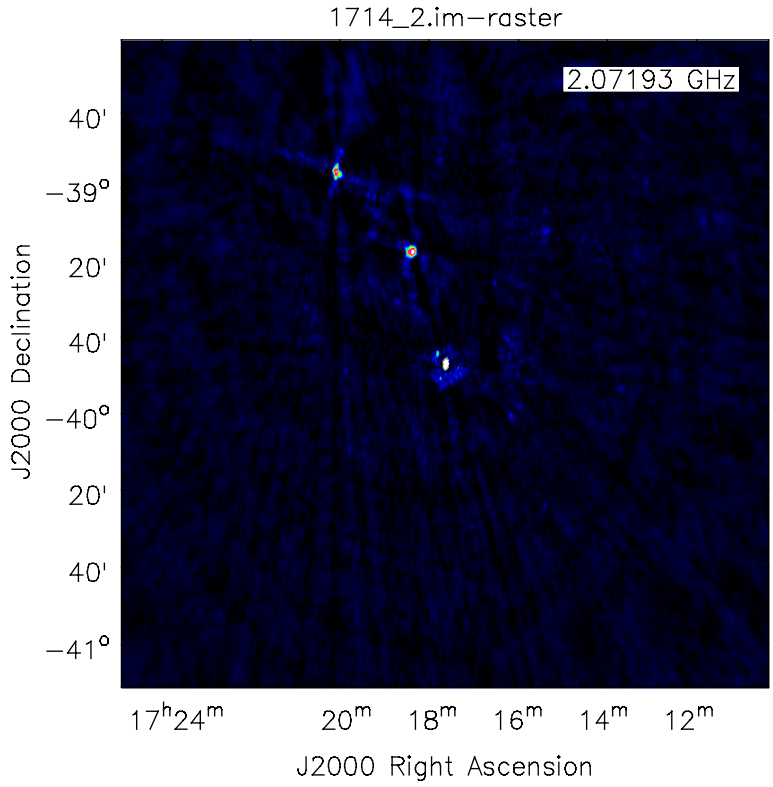

Figure 4.5: Map of the complex calibrator. It is shown how the field is confused by an extended emission around the calibrator that causes the problem in the shortest baselines and by two bright sources. The calibrator is 2.1 Jy bright, the other two source are 370 and 237 mJy without the primary beam correction, that is not known at that angular distance from the centre.

4.7 Mapping

To derive radio images from the *uv* data we have to transform the visibilities into a brightness map. In order to achieve this goal we have to invert the visibilities, treating them as the Fourier transform of the brightness map, and to deconvolve the dirty beam from the resulting map.

To image the entire field with `MIRIAD` in mosaicing mode we could choose among two approaches: the joint and the individual one. In the joint approach, the inversion of the *uv* data and the deconvolution is done on the entire field. In the individual approach the inversion and the deconvolution are applied on the single pointings. The maps of the single pointings are then linearly combined using the linear mosaicing algorithm (see next Section). We opted for the individual approach because the joint one showed some technical issues with `MIRIAD`. It was impossible to invert all the fields at once because that would overflow the fixed array size used by the task to store temporally the *uv* data. We acknowledged the staff who maintains `MIRIAD`.

The CABB has the big advantage to increase the bandwidth and therefore the sensitivity. However, at this frequency, $\Delta\nu/\nu$ is about 1 and this causes that the primary beam of the single dishes, that defines the FoV of each single pointing, varies by a factor 2 across the total band. At the lowest frequency used after flagging, 1.35 GHz, the radius of the primary beam at 5 percent of the peak is about 31 arcmin, while at the highest one, 3.1 GHz, it is 16.7 arcmin. To properly account for the change of the primary beam across the frequency range, we decided to divide the data into 7 sub-bands (see Table 4.3, paper I). The central frequency and the width was decided imposing a constant $\Delta\nu/\nu = 10\%$. We also used the `mfclean` task to deconvolve the images, to further reduce the effect of the primary beam changes across the bandwidth.

The steps to achieve the single pointing maps are:

1. run `invert` to obtain the dirty map and the dirty beam;

2. run `mfclean` to obtain the model of the field and the residuals of the deconvolved dirty map. `mfclean` use the Högbom (1974) algorithm assuming a linear dependence of the flux with the frequency;

3. run `restor` to convolve the model with the synthesized beam and to add the residuals;

4. since the angular resolution varies across the total bandwidth as the primary beam, we used the task `convolve` in order to force the syn-

Sub-bands	Central frequency (GHz)	R arcmin
1	1.469	30.8
2	1.649	27.5
3	1.850	24.4
4	2.075	23.6
5	2.329	20.1
6	2.613	18.7
7	2.932	16.7

Table 4.3: Sub-band frequency and primary beam radii at 5 percent of the peak.

thetic beam for all the frequencies at the same size, the largest one, that is the beam size at the lowest frequency.

The `invert` task was run using the Briggs (1995) algorithm, that requires to set a parameter called "robust". The robust parameter can vary between -2 and 2, at each value corresponds a different kind of weighting of the uv plane, resulting in a map with a higher resolution but a higher rms for -2, a lower resolution but a lower rms for 2. We set different robust values depending on the frequency and the pointing to achieve similar synthesised beams, so the `convolve` task did only small adjustments. We also tested that it is better to convolve after the `restor` and do not use the fwhm and pa option in the `restor` task to choose the synthesised beam because that can introduce errors in faint and medium sources, that are not entirely CLEANed. All these processes are highly parallelisable because all these tasks only use one CPU core each and every single pointing is independent from the other ones. To automatically parallelise the processes we used the python library `multiprocessing`.

4.7.1 Self calibration

Single pointing maps with strong sources show that there are artefacts that could be due to residual phase and amplitude errors after the standard calibration. In order to improve the maps, we decided to self calibrate the pointings. However, this process can be done only if strong point sources are present. To do that on `MIRIAD` we used the `selfcal` task. It requires a model of the field as input, usually from the cleaning tasks (`mfclean` in our case) and it returns the self calibrated uv data. We chose to only calibrate

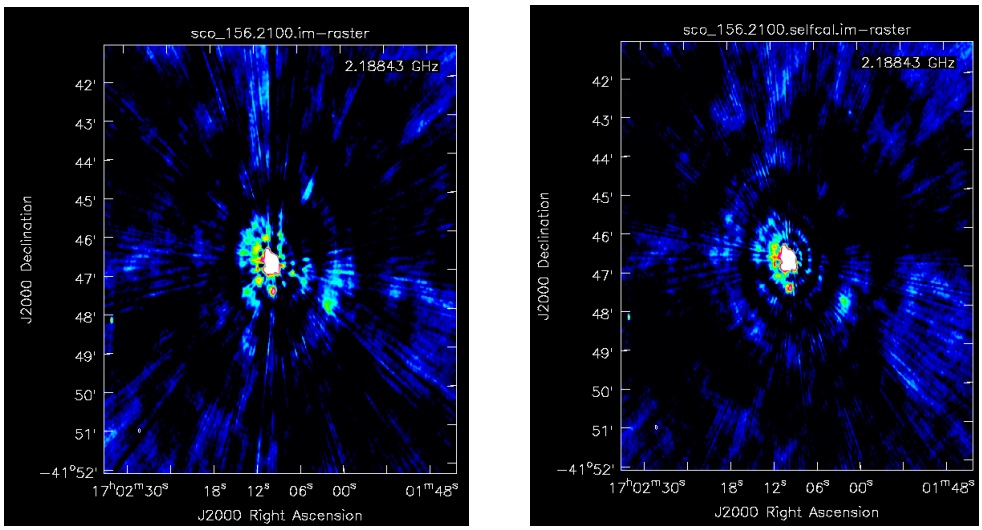

(a) Source not self calibrated (b) Same source self calibrated.

Figure 4.6: A particularly bright and extended source before and after the self calibration. Notice the reduction of bright lines artefacts and of the rms, from 210 μJy to 140 μJy.

the phases and not the amplitude to minimise the risks of the self-calibration process. In fact, it can force wrong gain correction to fit the model, introducing systematic errors. Even this process is highly parallelisable, so we proceeded in the same way explained in Section 4.7. The self calibration helped on lowering the rms and reducing the artefacts on the map (see Fig. 4.6, in this case the rms reduction was as high as 30%, from 210 to 140 μJy).

4.7.2 Mosaicing

The individual maps of all the pointings at each sub-band were linearly combined by using the task `linmos`. This produced seven maps of the whole SCORPIO field, at seven frequencies. A total map, obtained averaging the seven maps, has been also produced. The rms is $\sim 25\mu$Jy at high galactic latitude and it can be as high as 200 μJy in the GP. The resolution 9×5 arcsec (see Fig. 4.7).

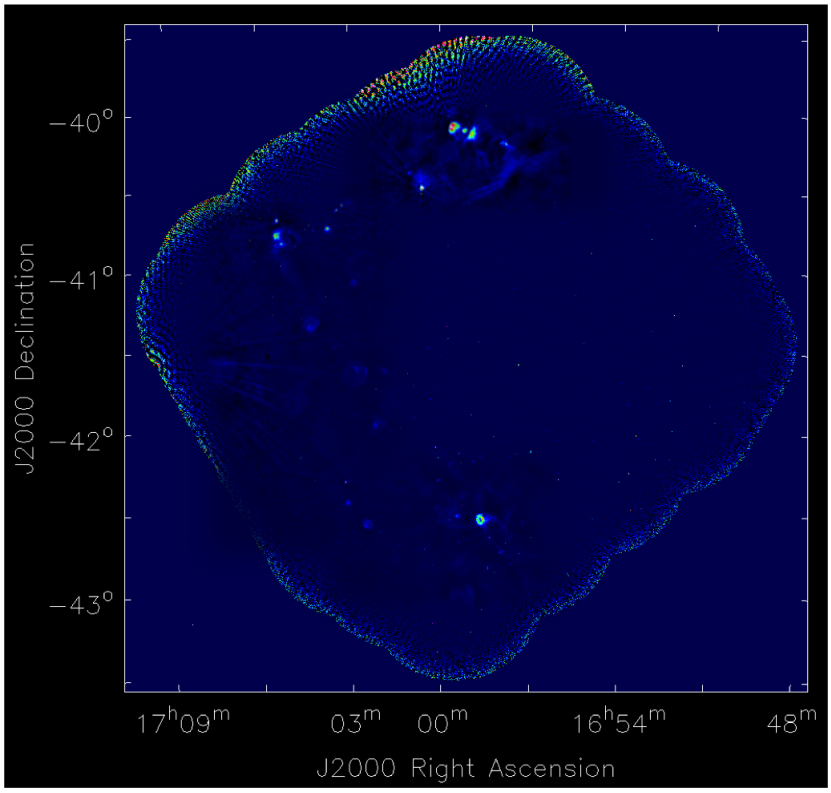

Figure 4.7: Final map of SCORPIO

4.7.3 Source extraction

At the present, there are several source extractors available: BLOBCAT, (Hales et al., 2012), Aegean, (Hancock et al., 2012), the source extractor described in Franzen et al. (2011) (hereafter the Franzen algorithm), etc. When the pilot map was imaged, the only source extractor available was the latter one so we used it. With the new maps we tested all the extractors and, after noticing that the differences are not significant, we decided to continue using the Franzen algorithm. This produces a background and a rms maps. after removing the background, the rms map was used to identify sources on the basis of their signal-to-noise ratio. Local maxima above 5σ were identified as sources. The peak position and flux density value were measured by interpolating between pixels. No gaussian fit was made. The centroid position, integrated flux density and source area were also calculated by integrating contiguous pixels down to 2.5σ, and double/multiple sources were identified as overlapping if the integration area contained more than one source. Our source extraction process yielded a sample of more than 2000 point-like sources in the whole field but the work is still in progress. We will now describe the source extraction process on the pilot field.

As shown in Fig. 4.8, the pilot field has not a uniform rms (the whole field has an analogue issue). The noise is larger near the edges, where the field is not covered by the highest frequencies because of the smaller primary beam and there are less pointings overlapping. We decided to select only the field inside the red rectangle in the Fig. 4.8, to have a better signal-to-noise ratio. The area chosen is defined by the rectangle between $l = 343$ and 344 deg and $b = -0.5$ and 1.833 deg. We extracted a catalogue containing 614 sources, that we matched with several catalogues. In Table 4.4 we show the results of the matchings and the references of the catalogues. The fraction of spurious identifications is calculated using the method proposed in Norris et al. (2006), consisting in cross-identifying after shifting the coordinates of the radio sources by 1 arcmin towards north, south, east and west and averaging the results. The optical and near infrared catalogues are too crowded to be reliable.

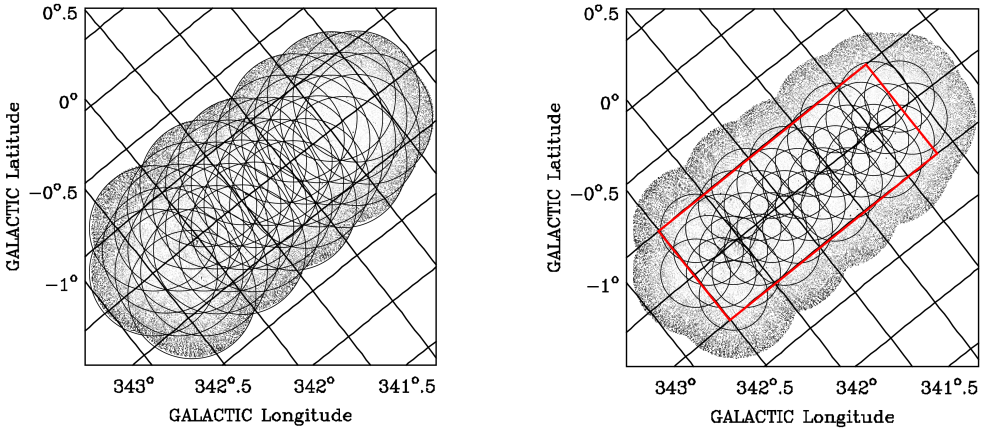

(a) Low frequency primary beam

(b) High frequency primary beam and, in red, the selected field.

Figure 4.8: SCORPIO pilot field showing the primary beam at the lowest and highest frequency.

Catalogue name	Number of matches	Band/λ	Spurious per cent	Ref
NOMAD	320	NIR-opt	NA	Zacharias et al. (2004)
2MASS	301	NIR	NA	Cutri et al. (2003) Skrutskie et al. (2006)
GLIMPSE	229	NIR-MIR	NA	Benjamin et al. (2003) Churchwell et al. (2009)
WISE	116	NIR-MIR	NA	Wright et al. (2010)
MSX6C	47	NIR-MIR	NA	Egan, Price, & Kraemer (2003)
AKARI	34	MIR	27	Ishihara et al. (2010)
IRAS	117	MIR-FIR	40	Helou & Walker (1988)
Hi-Gal	148	FIR	35	Molinari et al. (2010)
ATLASGAL	14	mm	26	Contreras et al. (2013)
MGPS-2	43	cm	4	Murphy et al. (2007)
WBH2005	18	cm	1	White, Becker, & Helfand (2005)
RMS	6	cm	0	Urquhart et al. (2007)

Table 4.4: Number of matched sources. NA stands for not applicable due to the overcrowding of the catalogue.

Chapter 5

Study of the spectral indices

As discussed in the previous chapters, thanks to future surveys we will able to detect millions of sources. For many of them this will be their first detection. In this scenario, one of the most urgent issues to face it to reliably and automatically classify as many sources as possible, especially in the GP, where the Galactic population adds up to the extra-galactic one. There are essentially five ways to classify a generic radio source, depending on the data available and whether it is resolved or not:

1. studying the radio emission mechanism, which implies the knowledge of the spectral energy distribution (SED) in the radio wavelengths;
2. studying the polarization, which requires a very high signal-to-noise ratio;
3. studying the time domain, which requires a sufficient time resolution;
4. studying the complete SED, which requires the identification of the source counterparts at different wavelengths;
5. studying its morphology, in case the source is resolved.

In this chapter we will focus on the first method, since it is solely based on radio multiwavelength or wide-band observations and no further information is required. The radio SED depends on the continuum emission mechanism, usually ascribed to bremsstrahlung or synchrotron radiation. As discussed in the introduction, a parameter that characterises the SED in the radio wavelengths is the spectral index α. To derive this information for a large number of sources, considering that the future surveys will detect millions of sources (Norris et al., 2011), we developed an algorithm to automatically compute the spectral index.

Our algorithm has been applied to the images of the SCORPIO survey. As described in Chapter 4, in Paper I we produced a catalogue of 614 point sources located in the pilot field, listing their flux densities, position and possible infrared counterparts. In this chapter we present a statistical analysis of the radio SED of the 614 point sources extracted and catalogued in Paper I, with the aim to discriminate Galactic and extra-galactic point sources. In Section 5.1 we describe our algorithm to automatically reconstruct the source SED and derive the spectral index. In Section 5.2 we present our results, thoroughly discussing their relation with ATLAS (Norris et al., 2006), highlighting and explaining the differences. Conclusions are reported in Section 5.3.

5.1 Image analysis

The SED can give us, besides information on the mechanism of the radio emission (thermal or-non thermal), clues on some physical parameters such as magnetic field or electron density when the turn-over frequency can be estimated. This information can help us to characterise Galactic sources and distinguish them from extra-Galactic ones.

5.1.1 Flux Extraction Algorithm

In order to automatically estimate the source flux densities at different frequencies and the local noise, we wrote a Python script that runs in CASA (Common Astronomy Software Applications, McMullin et al. 2007) and uses the `imfit` task (see flowchart in Fig. 5.1). The script reads the position of each source from Paper I catalogue and creates a box encompassing it and 4 other boxes, that are 15 pixels along the x axis and 10 pixels along the y axis away from the vertices of the central box. The box dimensions are chosen to be 3 times the beam major and minor axis respectively (the major axis is oriented along the north-south direction). The script calls `imfit` in the central box and `imstat` in the other four ones. `imfit` performs a bidimensional Gaussian fit in the chosen region and returns a Python dictionary *dic* containing all the fit parameters (such as integrated flux, Gaussian peak position, major and minor axis dimension, etc.). The task `imstat` returns different statistical information for each box, such as noise, mean and median. The script calculates the median of the noise in all the boxes. At the end the script returns two matrices with N lines and M columns, where N is the number of sources and M the number of sub-bands. Every element a_{ij} of the first matrix is the fit parameter *dic* of the $i^{\rm th}$ source for the $j^{\rm th}$ sub-band,

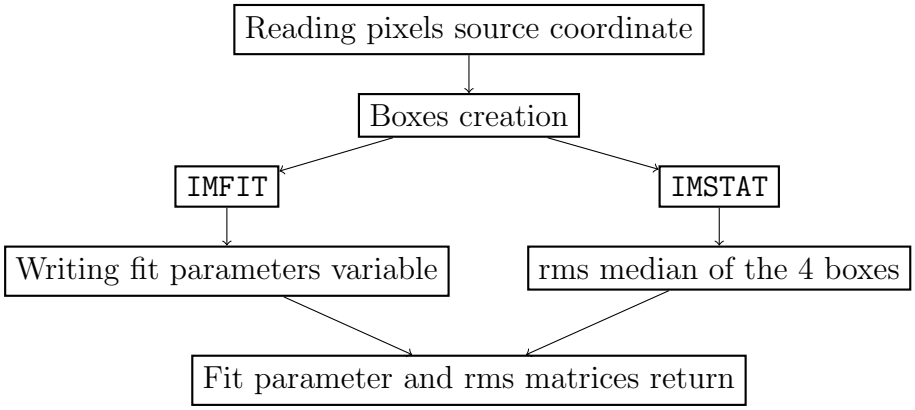

Figure 5.1: Flowchart for the flux extraction algorithm

in a similar way every element b_{ij} of the second one is the local rms of the i^{th} source for the j^{th} sub-band. If the Gaussian fit does not converge for the i^{th} source and the j^{th} sub-band, a_{ij} is set to 0.

5.1.2 Spectra construction and control algorithm

For the purposes of this work, we assume that all the sources follow a power-law spectrum (i.e. linear in the log-log plane). The SED reconstruction is performed by another algorithm, described below. It linearly fits $\log S$ as a function of $\log \nu$, where S is the flux density and ν the frequency. To guarantee that the SED has a linear behaviour it fits a second degree polynomial and compares the χ^2 of the linear and parabolic fits. There are 30 sources in which the χ^2 of the parabolic fit has a better value. It is possible that this is due to the presence of a turn-over. In this case the algorithm considered in the linear fit only the frequencies greater than the turnover frequency, chosen as the one with the largest χ^2. In Fig. 5.2 the spectrum of one of these sources is shown as an example. This is how the algorithm works step by step, performing the following tests for each frequency to ignore "bad points" (see Fig. 5.3):

1. The flux S is equal or less than 0. This is the case of non-converged Gaussian fit or Gaussian fit of negative values on the map, for e.g. caused by artefacts:

$$S \leq 0. \tag{5.1}$$

2. The difference between the position of the Gaussian fit peak and the position given by the source extraction algorithm is greater than half

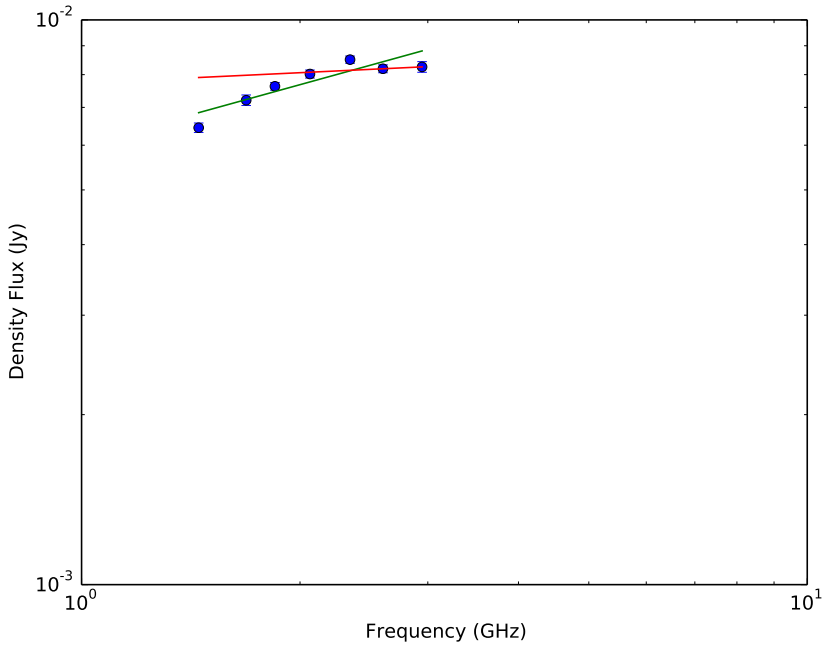

Figure 5.2: Spectrum of SCORPIO1_243. In green the straight linear fit while in red the line of the fit after the application of the turnover algorithm is showed.

the width of the beam w. This is the case of a Gaussian fit made on a near brighter source or on bright source sidelobes:

$$P_{\text{peak}} - P_{\text{list}} \geq \frac{w}{2}. \tag{5.2}$$

3. The area of the fitting Gaussian exceeds n times the average of the other $M-1$ frequencies. This is the case of fitting a faint source whose parameters can be affected by the noise:

$$A \geq n\bar{A}, \tag{5.3}$$

where A and $\bar{A}$ are respectively the area of the Gaussian fit for a sub-band and the mean area of all the sub-bands. We chose $n = 1.3$ after testing several values between 1 and 2. The results of these tests on ~ 50 sources have been visually checked and $n = 1.3$ was the minimum value above which fit appeared unreliable.

4. The flux density significantly exceeds the average $\bar{S}$.

$$S > 1.8\bar{S}. \tag{5.4}$$

If a frequency of a source shows one of those irregularities, it will be discarded and will not contribute to the linear fit. The linear fit is weighted on the single point error

$$\Delta S = \sqrt{e_{\text{fit}}^2 + e_{\text{rms}}^2 + e_{\text{cal}}^2} \tag{5.5}$$

where e_{fit} is the fit uncertainty, computed by `imfit`, e_{rms} is the noise and e_{cal} is the calibration error.

5.1.3 Group sources

A total of 65 over 614 sources are classified by the source finding algorithm as "double sources"(Franzen et al., 2011). They can be components of larger extended sources or simply lie close to each other. To fit these multiple sources `imfit` reads a file that contains a list of estimates of the position of the Gaussians peaks, their dimensions, orientation and brightness. We created a script hat produces as output this file for every group source, keeping the Gaussian size and orientation fixed to the synthesised beam values. Then the Gaussian fitting algorithm works in the same way as it does for the single sources. The algorithm treats each component of a double source as a real component of a larger source, adding the integrated flux densities and using

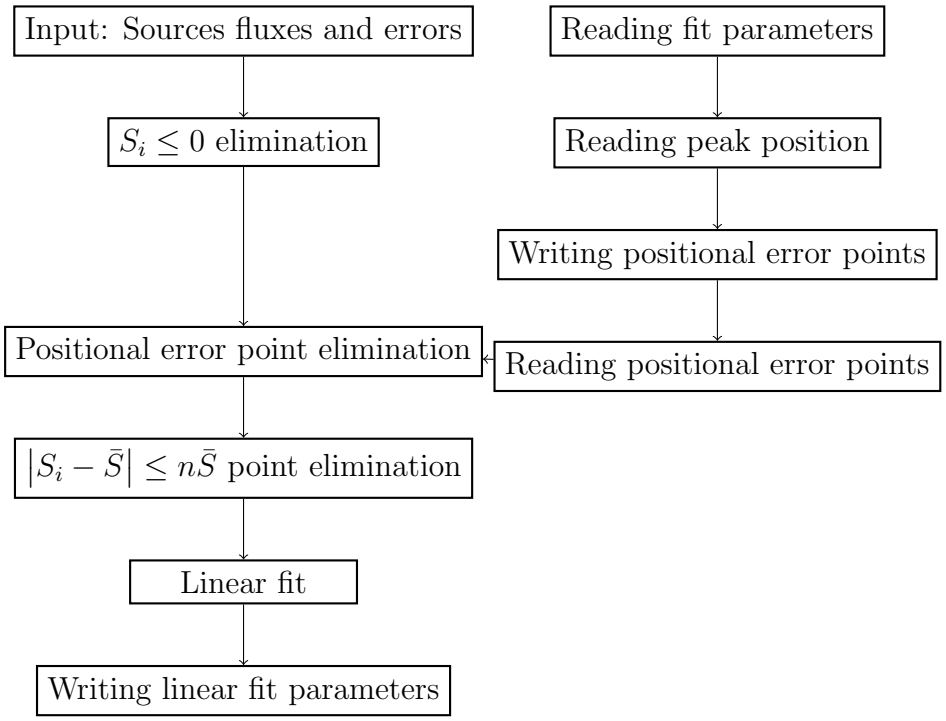

Figure 5.3: Spectral index extraction algorithm flowchart.

the result as the flux density of the complex source. In Fig. 5.4 and 5.5 we show, as an example, the spectrum and the gaussian fit of one of the double sources. Notice that this double source appear to be a FR-I type radio source next to a background source so the spectrum can be a sum of the two spectra.

5.1.4 MGPS-2 matches

As presented in paper I, 43 sources matches second epoch Molonglo Galactic Plane Survey (MGPS-2, Murphy et al. 2007) sources. We can use them to check our spectral indices. If we exclude double sources and those embedded in diffuse emission (with confusion, because of the large MGPS-2 beam), there are only 16 sources left, shown in Fig. 5.6 and 5.7. Hence we proceed with calculating their spectral index, including the 843-MHz MGPS-2 point. In Fig. 5.8 and 5.9 we show the spectra of the 16 sources. Roughly in all but SCORPIO1_178 the SEDs are consistent with the 843 MHz flux. In the case of SCORPIO1_178 the discrepancy is due to the fact that the MGPS-2 centroid is not centred on the SCORPIO source and its beam encompasses another bright source, leading to a higher flux density of the MGPS-2 source.

5.2 Spectral indices analysis

Since images obtained with sub-bands have a lower signal-to-noise ratio than the full band image, for the faintest sources we could not have 2 or more sub-bands with a reliable flux density measurement. In fact the algorithm failed for 104 sources, so we extracted the SED for 510 sources of the 614 detected. However not all the 510 spectral indices are accurate ($\Delta\alpha \lesssim 0.2$, the minimal value necessary for a good separation between the synchrotron and thermal free-free emission) due to the errors on the flux density extraction in the sub-bands. It is important to evaluate a priori when the spectral index of a given source can be extracted accurately. To achieve this goal we set up the simulation described below. We used the `uvgen` task on miriad to simulate 10 ATCA fields with a total of 301 sources with a flat SED. We mapped the whole fields and derived the spectral index by following the same method used for the SCORPIO data. As we can see in Fig. 5.10, simulated sources with a signal-to-noise ratio smaller than ~ 40 have spectral index error even in excess of 0.5. Therefore we consider 40σ the threshold below which spectral index values become too inaccurate to be significant and, in the following, we restrict the analysis of the spectral index of the sources in SCORPIO only to those detected with a signal-to-noise ratio greater than 40.

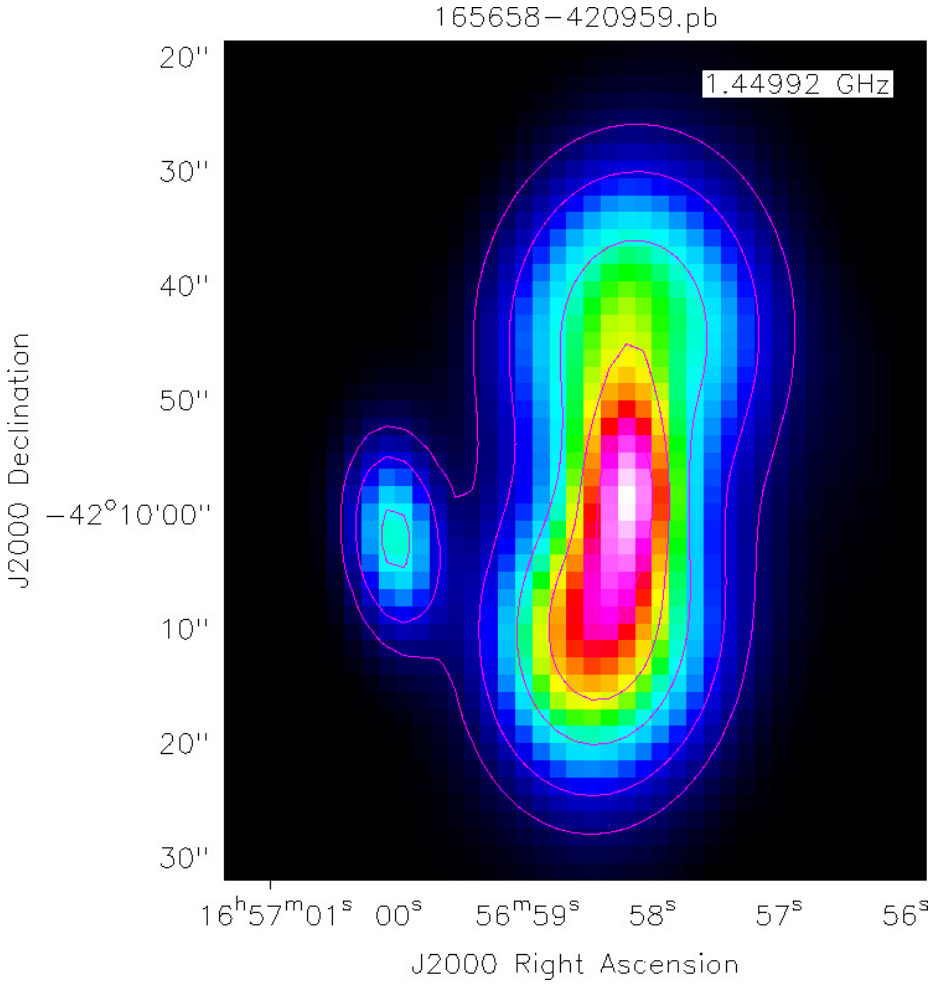

Figure 5.4: Map of one of the double sources, SCORPIO1_334. The purple contour represents the gaussian fit made by the described algorithm. To fit this source the script used 4 gaussians.

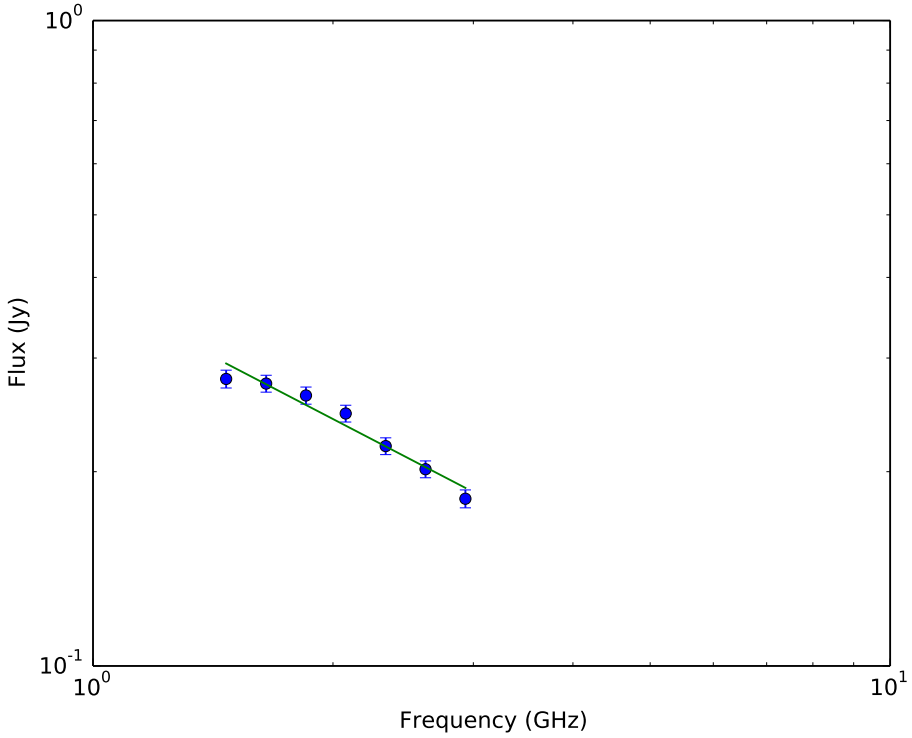

Figure 5.5: Spectrum of SCORPIO1_334. The straight green line represents the linear fit. The points result from the sum of the value of each of the 4 gaussian at each frequency.

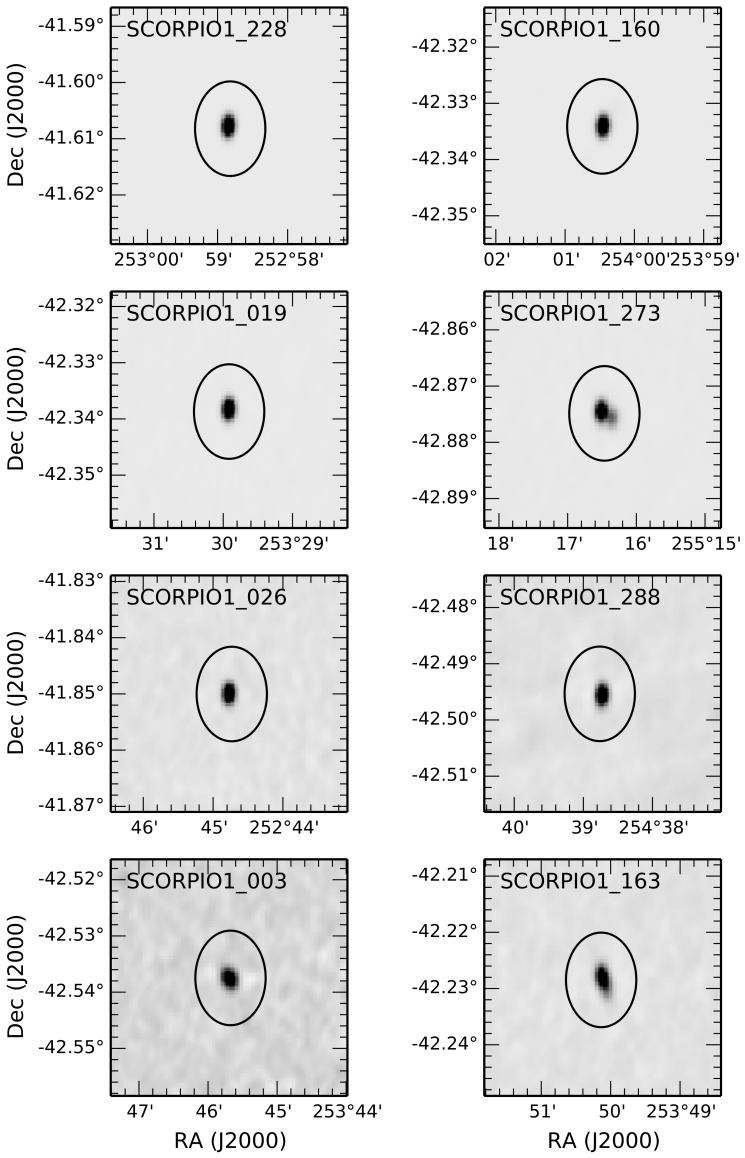

Figure 5.6: Grey scale of the 16 SCORPIO sources with a MGPS-2 match. The black ellipse embedding the sources is the Molonglo beam.

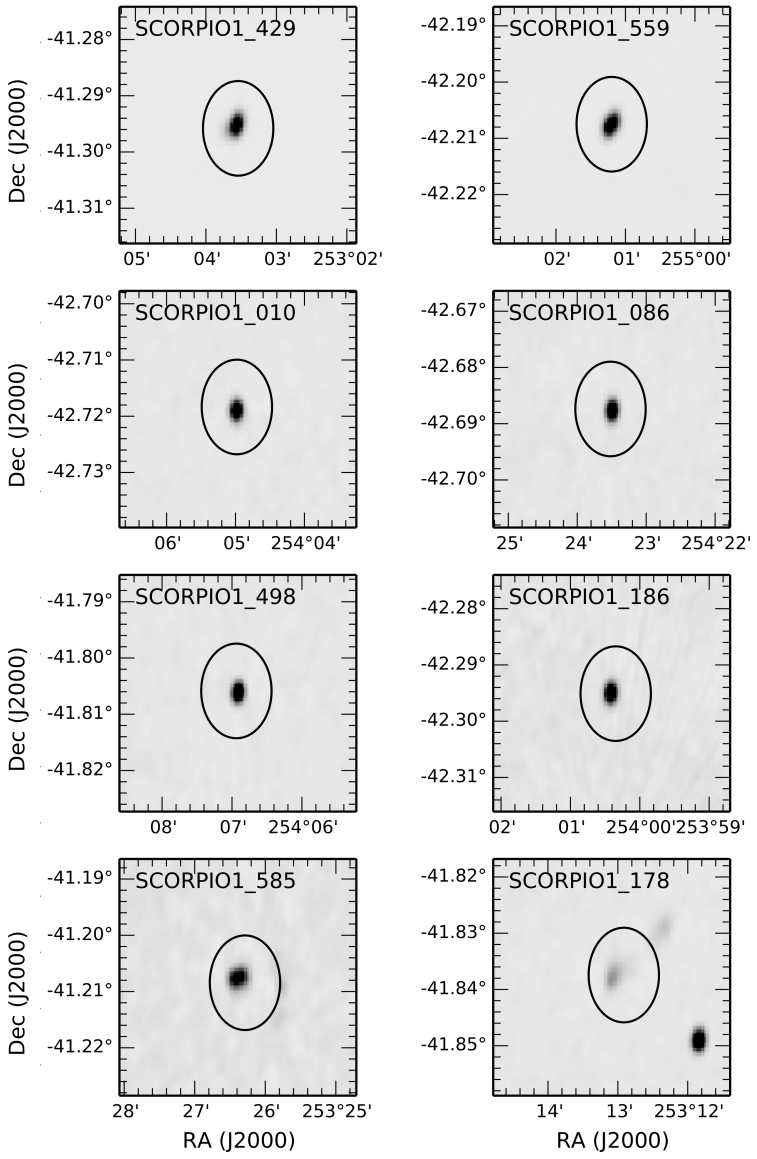

Figure 5.7: Continued from the previous figure.

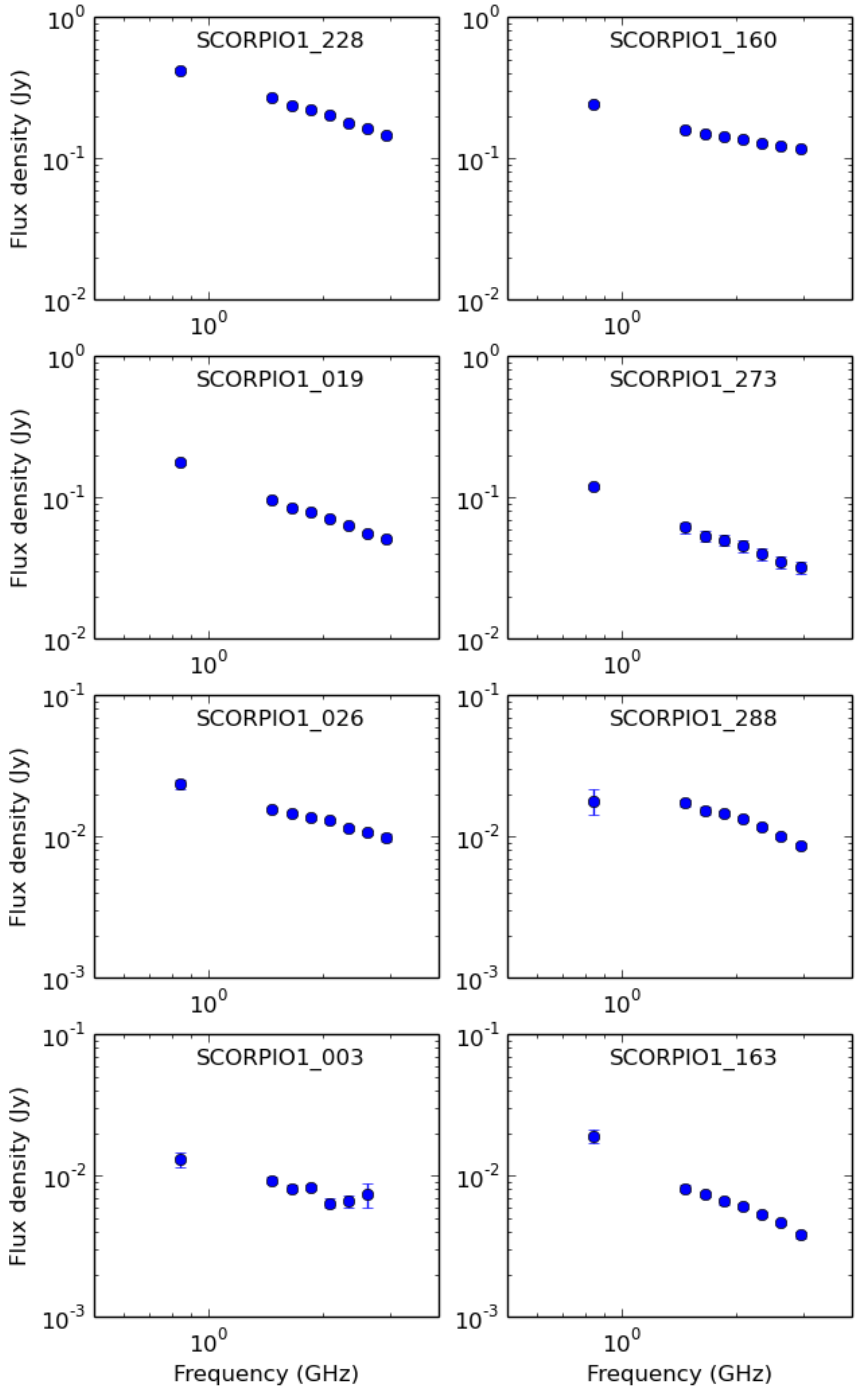

Figure 5.8: Spectra of the 16 sources selected among the 43 sources that match with the MGPS-2.

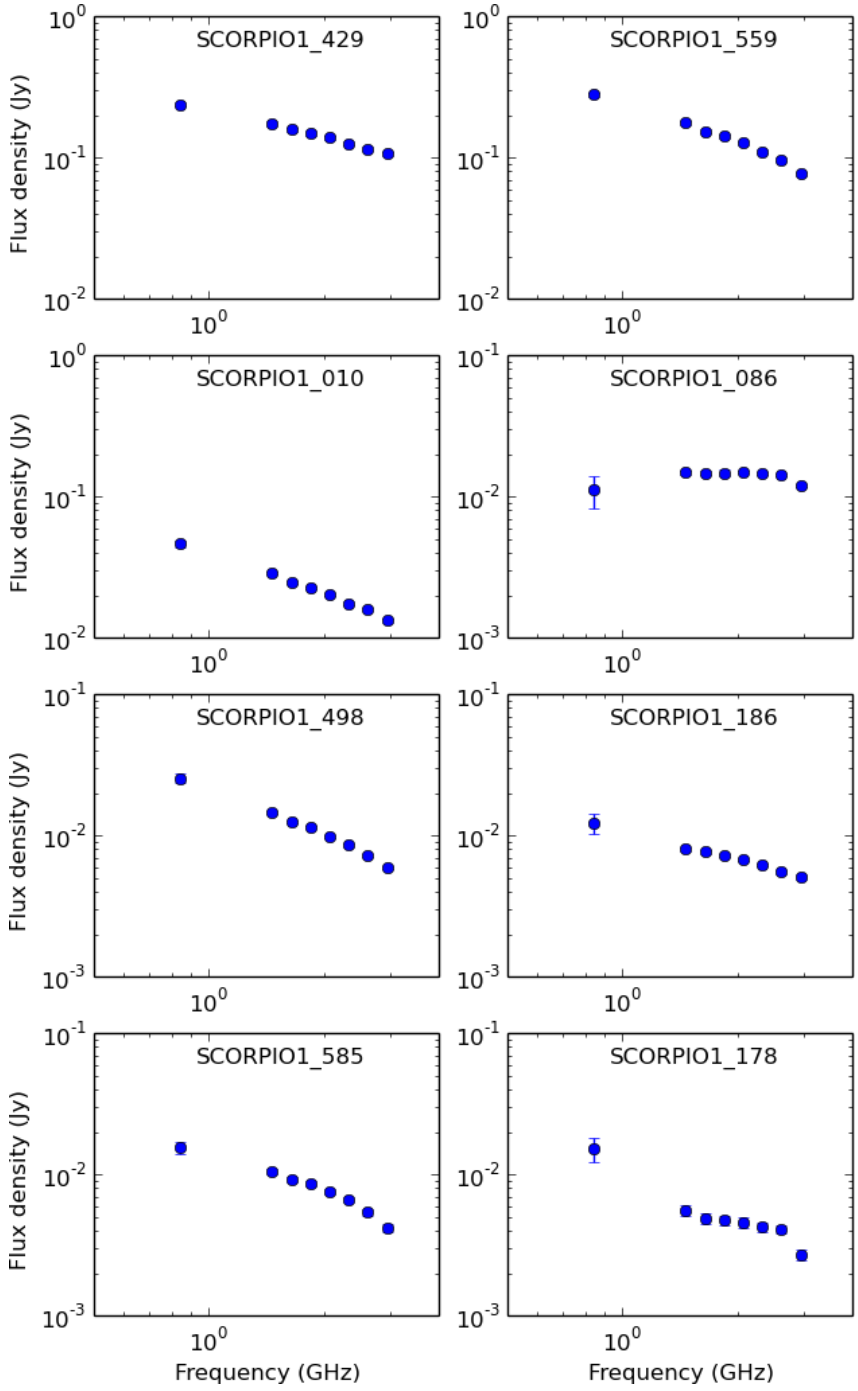

Figure 5.9: Continued from the previous figure.

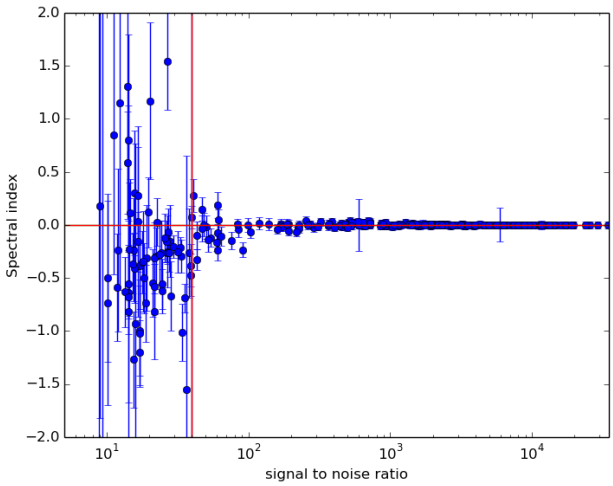

Figure 5.10: Spectral indices against signal-to-noise ratio in the simulation. All the sources have been built to have a flat SED, but the spectral indices are not accurate enough below 40σ (indicated by the red line).

SCORPIO data strongly support that the 40 threshold is a good choice, as it is possible to notice in Fig. 5.11. The median of the spectral index errors depends on the signal-to-noise ratio as a function $\sim 1/\sigma^2$ and below $\sim 40\sigma$ it decreases rapidly. Furthermore at 40σ the median on the spectral index errors is ~ 0.2. Our threshold of 40σ agrees with Rau, Bhatnagar, & Owen (2016) who suggest a value between 16σ and 100σ as the limit of reliability for spectral indices. Considering that in the pilot field the background noise is $\sim$ 25-30 μJy/beam, we conclude that, in order to extract a reliable spectral index, the flux density of a source in SCORPIO shall be at least 1 mJy. The number of sources in SCORPIO with a flux density above 1 mJy is 306.

5.2.1 Results

In Fig. 5.12 we plot the histogram of the distribution of the spectral indices extracted for the sources in SCORPIO, setting the bin width to 0.25. There is one main peak around ~ -0.9 and other smaller peaks around ~ -0.2 and ~ 0.6.This result derives from the sum of several source populations, both Galactic and extra-galactic.

To model the spectral index distribution, considering that there might be two or more different populations, we fit it with a variable number of Gaussians. We used the Bayesian Information Criterion (BIC; Schwarz 1978)

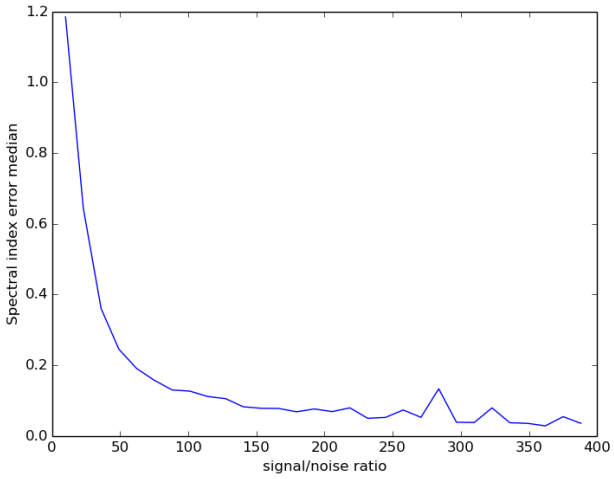

Figure 5.11: The median on the spectral indices error against signal-to-noise ratio in SCORPIO.

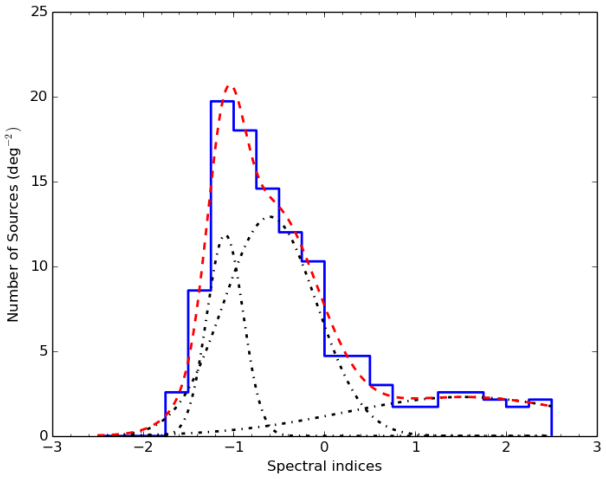

Figure 5.12: Spectral index distribution of the SCORPIO survey using a 0.25 wide bin in blu straight line, modeled using 3 Gaussians (red dashed line). In black dash-point line the three Gaussian components of the final model.

ΔBIC	Evidence against higher BIC
$0 < \Delta\text{BIC} < 2$	Marginal
$2 < \Delta\text{BIC} < 6$	Positive
$6 < \Delta\text{BIC} < 10$	Strong
$\Delta\text{BIC} > 10$	Very Strong

Table 5.1: Criteria to exclude models based on their higher BIC in respect with other models as in Kass et Raftery (1995).

to select which model best fits our data. This model is the one that minimizes the BIC parameter. We used the BIC formula as defined in Wit et al. (2012):

$$\text{BIC} = -2 \cdot \ln \hat{L} + k \cdot \ln n \tag{5.6}$$

where $\hat{L}$ is the maximised value of the likelihood function, n is the number of data points and k is the number of free parameters of the model. We used the criteria described in Kass et Raftery (1995) to exclude models (see Table 5.1). The BIC parameter increases for models with a larger number of free parameters so we can be confident in choosing high parameters number models. Table 5.2 shows that a model consisting of 3 Gaussians (see Fig. 5.12) has a lower BIC than the other considered models (one or 2 Gaussians and the skewed Gaussian, a Gaussian with an additional parameter that makes the function asymmetrical). This Bayesian approach tells us the spectral index distribution reported in Fig. 5.12 can be well approximated by the sum of three different source populations. In the following we compare the statistical results of the spectral index analysis on the SCORPIO data with those of two other surveys, THOR (The HI, OH, Recombination line survey of the Milky Way, Bihr et al. 2016) and ATLAS (Australia Telescope Large Area Survey, Norris et al. 2006), the former performed in the GP and the latter at high Galactic latitude. ATLAS can be used as a template for extra-galactic population while SCORPIO population is the sum of Galactic and extra-galactic sources, as the Galaxy is optically thin at radio wavelengths.

5.2.2 Comparison with THOR

THOR is a survey of a ~ 100 deg^2 area in the GP, carried out with the VLA in spectral line and continuum from 1 to 2 GHz with an angular resolution of $10-25''$. The noise level is $\sim 0.3-1$ mJy beam^{-1}. Bihr et al. (2016) detected around 4400 sources above 5σ. For ~ 1800 of them the authors measured a spectral index between 1 and 2 GHz. The spectral index distribution

Model	BIC
Gaussian	143.3
Two Gaussians	91.4
Three Gaussians	69.4
Skewed Gaussian	81.4
One Gaussian plus one skewed Gaussian	86.0

Table 5.2: BIC for every model considered for the SCORPIO survey. Every Gaussians needs 3 parameters while the skewed Gaussians need 4 ones.

Model	BIC
Gaussian	85.4
Skewed Gaussian	81.7

Table 5.3: BIC for every model considered for the ATLAS survey. Every Gaussians needs 3 parameters while the skewed Gaussians need 4 ones.

is similar for SCORPIO and THOR, with one main difference: in THOR the peak centred between -0.1 and 0 is much higher with respect to the synchrotron peak at -0.9. This is probably due to the difference in the source flux densities. While in the SCORPIO survey we selected all the sources above 1 mJy, in the THOR survey, which has a higher rms noise, they selected all sources that have a reliable intensity for all the six spectral windows in which they divided their data. This makes their flux limit much higher than ours resulting in 18 sources deg^2 with an extracted spectral index, against our 120. The fact that their flux limit is not a priori fixed makes a direct comparison between THOR and SCORPIO not feasible. We know that the HII region are among the brightest galactic sources and that the extra-galactic sources increase rapidly in number with the sensitivity. Considering that, we can reasonably state that it is possible to detect almost all of the H II regions, even with THOR sensitivity, while a lot of galaxies are lost. For this reason the ratio between the peaks around $\alpha = 0$ and around $\alpha = -0.9$ is higher in THOR than in SCORPIO.

5.2.3 Comparison with ATLAS

ATLAS (Norris et al., 2006) is a survey carried out on two main fields, the Chandra Deep Field-South (CDF-S) and the European Large Area ISO Survey-South 1 (ELAIS-S1) at 1.4 GHz with ATCA. The third ATLAS data release (Franzen et al., 2015) includes observations taken using the CABB receiver with a 500 MHz bandwidth covering 1.3-1.8 GHz. It is important to

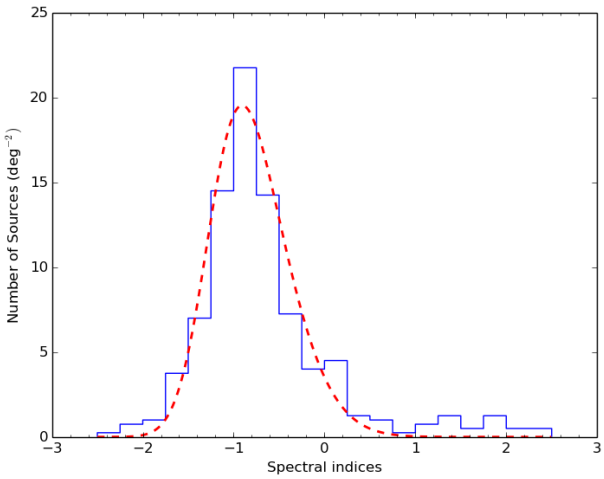

Figure 5.13: Number of sources per square degree in a 0.25 wide bin histogram for the ATLAS survey, modelled as a skewed Gaussian (red dashed line).

notice that the ATLAS fields are located far away from the GP. We expect to find only an extra-galactic population.

In Franzen et al. (2015), the ATLAS DR3 CABB data were divided into two sub-bands and two separate mosaics of each field were created, one using the lower sub-band centred at 1.40 GHz and the other one using the higher sub-bands centred at 1.71 GHz. For consistency with SCORPIO, we extracted the spectral indices of the ATLAS sources running the algorithm described in Section 5.1. We ran it on the two mosaic maps. We then considered the sources brighter than 1 mJy at 2.1 GHz for both surveys (extrapolated using the spectral index) and derived the source surface density (number of sources deg^{-2}). As shown in Fig. 5.13, the synchrotron peak is the predominant component and there is a minor peak around 0. This can be due to the extra-galactic sources, the Gigahertz Peaked Spectrum (GPS), that can have the turnover frequency in around 1.5 GHz and blazars that can have flat spectra. We tried to fit this distribution with different models, as in Section 5.2.1, and we found that a skewed Gaussian is the best-fit (see Table 5.3 for BIC comparison and Fig. 5.13 for the model). Given the high galactic latitude of the ATLAS survey, we can assume that the majority of the ATLAS sources are extra-galactic, so we used the ATLAS model as a template for the extra-galactic population of SCORPIO. We found 20 percent more sources per square degree in SCORPIO than in ATLAS (120 versus

100). To determine if this difference is statistically significant we consider the total number of source, 306 for SCORPIO, 401 for ATLAS. Assuming a poissonian distribution, the statistical error of a number of objects N is $E = \sqrt{N}$, so SCORPIO has 306 ± 17 sources over 1 mJy while ATLAS has 401 ± 20 sources, computing the source density, we have 120 ± 7 sources deg^{-2} in SCORPIO and 100 ± 5 in ATLAS. The difference is statistically significant. Using ATLAS as a template for SCORPIO, we found that a model using the ATLAS skewed Gaussian plus one more Gaussian gives a BIC of 79.3, better than almost all the models shown in Table 5.2 with exception for the one that uses three Gaussians. Nevertheless the model including the ATLAS extra-galactic template has a physical motivation making it the more reliable one. Fig. 5.14 shows that the ATLAS Gaussian fits quite well the peak at $\alpha = -0.9$ and, more importantly, another Gaussian fits the other peaks. Maybe increasing the statistics we could say that they are part of more than one single population, as expected, but, with our data, we can only say that they are part of a broader galactic population.

In Fig. 5.15 the difference between the SCORPIO and the ATLAS population per spectral index bin is shown. The width of the bin is 0.5. The errors $e_{\rm i}$ associated with the i^{th} bin are, assuming a poissonian distribution for both ATLAS and SCORPIO and knowing that the error of a sum is the sum of the errors:

$$e_{\rm i} = \sqrt{N_{\rm Si}} + \sqrt{N_{\rm Ai}} \tag{5.7}$$

where $N_{\rm Si}$ and $N_{\rm Ai}$ are respectively the number of SCORPIO sources and ATLAS sources in the i^{th} bin. We can recognize 3 regions of the spectral index α:

1. $-2.5 < \alpha < -0.5$: this range of spectral indices is typical of optically thin (and possibly, aged) synchrotron emitting sources. The number density of sources in the two surveys is not significantly different, implying that all SCORPIO sources in this spectral index range may be extra-galactic;

2. $-0.5 < \alpha < 0.5$: the difference here is $\sim 15 \pm 6$ per deg^{-2}. These are typical spectral indices of Galactic sources that show a thermal emission in a optically thin environment, e.g. HII regions, Planetary Nebulae (PNe) and Luminous Blue Variable (LBV) or flat spectrum synchrotron source;

3. $0.5 < \alpha < 2.5$: there is an excess of about 11 ± 5 sources deg^{-2} with a spectral index in this range, suggesting stellar winds, interacting stellar

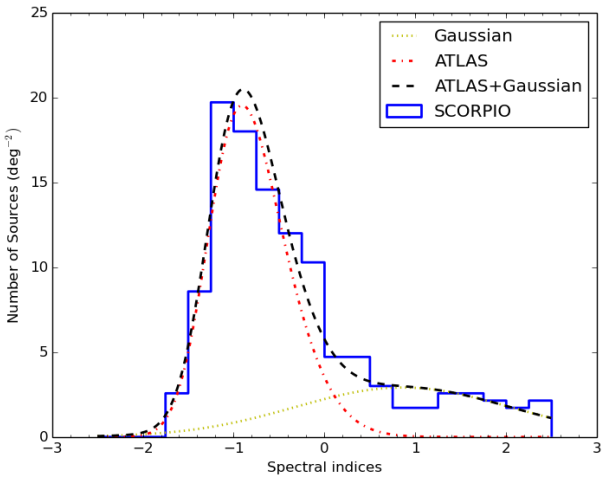

Figure 5.14: SCORPIO spectral index distribution modelled as a sum of the ATLAS model and a Gaussian.

winds and thermal emission in a optically thick environment, e.g. Wolf Rayet, LBV, OB stars and compact and ultracompact HII regions.

Obviously we expect some overlap between spectral index regions. Furthermore, the different frequency range of the ATLAS survey makes likely to have a surplus of extra-galactic flat sources due to possible turnover positions.

Note that the difference between the total sources surplus in SCORPIO (20 percent) and the one in the interval $-2.5 < \alpha < 2.5$ is due to the smaller bandwidth in ATLAS, resulting in a larger number of spurious spectral indices.

5.3 Results discussion

The work described in this chapter can be divided into 4 parts: the development of an algorithm to compute spectral indices of sources in wide-band radio images; the test of this algorithm on the SCORPIO data; a simulation to check the reliability of the algorithm; the comparison between the result on the SCORPIO data and other galactic and extra-galactic surveys.

The first information that we can derive from our work is that, with a bandpass like the SCORPIO one, the signal-to-noise ratio for the objects in the field has to be at least 40 in order to obtain a spectral index with an uncertainty $\lesssim 0.2$. With a narrower bandpass that should be even worst,

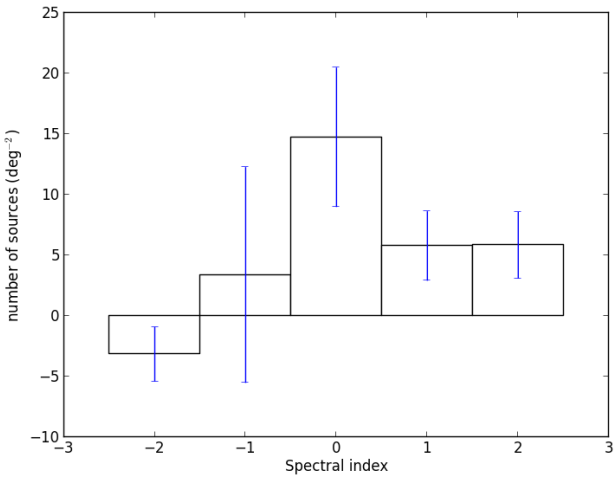

Figure 5.15: Difference between the SCORPIO and the ATLAS spectral indices histogram.

maybe $\sim 100\sigma$ in the case of the EMU bandpass, so only the sources brighter than 1 mJy will have a reliable spectral indices. We could go deeper in some sky region planning different frequencies survey to extend the studied band.

From the comparison between SCORPIO and ATLAS, we discovered that, in the Galactic Plane, the source count with flux densities exceeding 1 mJy is about 20 percent higher than the source count at high galactic latitude. We have 15 Galactic sources deg^{-2} with a spectral index of $\alpha \approx 0$, suggesting optically thin thermal emission such as HII regions and planetary nebulae, with the remaining 12 per square degree with $0.5 < \alpha < 2.5$, suggesting optically thick thermal emission such as stars and compact HII regions.

These results are very important for planning forthcoming radio surveys because they can give us an expected number of Galactic sources. As an example, in the whole SCORPIO field, that have an area of ~ 5 deg^{-2}, we expect ~ 100 Galactic sources with a flux density greater than 1 mJy. This information can be extended to larger radio surveys, such as EMU, that will observe, assuming a GP width of 2 deg and a total coverage of $\sim 75\%$ of the sky, ~ 540 deg^2 of the GP. Assuming the Galactic source density found in this chapter, we expect to detect $\sim 10\,800$ Galactic sources brighter than 1 mJy.

Chapter 6

Source imaging

The main product of the interferometric observation presented in Chapter 4 is a series of images of the surveyed portion of the sky. We produced several all-field maps obtained using different mapping algorithms and settings (different Stokes parameters, different weighting schemes, etc.). Each of them therefore displays peculiar features and, collectively, are aimed at covering different possible analyses, for example searching for polarisation, optimising point-source extraction, recovering extended emission and so on. The first map produced was the pilot map (paper I). It was exhaustively described in Section 4.1. In this chapter we are presenting all the other maps produced in this work and the reason behind their construction. Finally we will discuss some of the detected sources.

6.1 First iteration map and rms map

The first image of the whole field obtained with the "extended" configuration data is shown in Fig. 6.1. The rms at high Galactic Latitude ($b > 0.5$) is $\sim 25\,\mu$Jy, the resolution is $9.8'' \times 5.8''$, the total covered area is roughly 5 deg^2. The rms is higher near in the Galactic Plane (it can reach 200-300 μJy) and near the extended source on the top of Fig. 6.1. This is due to the artefacts caused by the inadequate uv coverage with respect to the size of the sources present in the imaged field, in particular the lack of short baselines, and by the diffuse emission that permeates the Galactic Plane (see Fig. 6.2). This image was made using the individual approach described in Chapter 4. From this map we derived the rms and the background map using the BANE algorithm from the AEGEAN tool (Hancock et al., 2012). Then we ran the Franzen et al. (2011) source finder algorithm on the all-band image and we found 2206 point-like sources. An independent check was performed

using BLOBCAT (Hales et al., 2012), whose result agreed with our previous estimate.

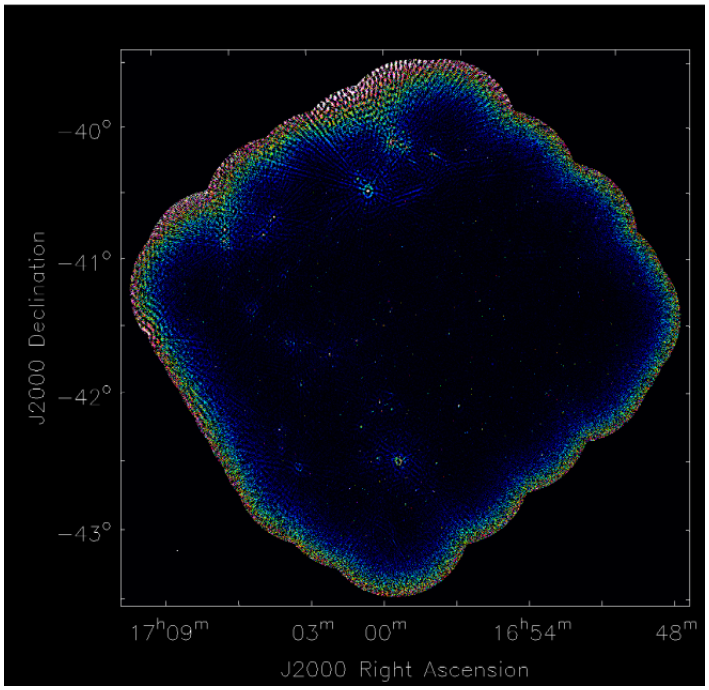

Figure 6.1: First iteration map of the whole field, using only the extended configuration observations, before the primary beam correction.

6.1.1 Primary beam correction

The mosaicing process requires the correction of the telescope primary beam in order to get consistent measurements in the overlapping regions. This correction is applied to take into account the decrease in sensitivity experienced when we observe progressively farther for the phase centre. A non accurate knowledge of the primary beam prevents a good flux density measurement, in particular for the sources far from the center of the individual pointings. As a consequence, in case the primary beam is not well defined as a function of the frequency, the spectral indices of the sources are affected by systematic errors, in principle different for each location.

In the very last years measurements of the primary beam shape for the new 16-cm CABB receivers were made across the entire usable frequency range (1.1 to 3.1 GHz). Although an accurate primary beam model is now available, it was not implemented in MIRIAD when imaging of the SCORPIO pilot was performed. Instead we used the Gaussian primary beam model

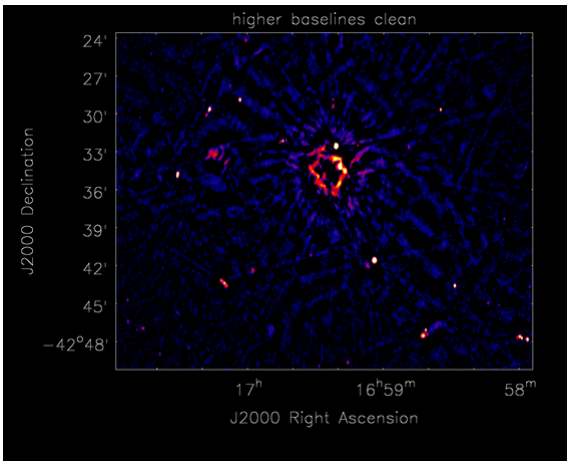

Figure 6.2: Region around the s17 in the first iteration map. Notice the artefacts and the missing flux.

made by Wieringa et Kesteven (1992) (see Table 6.1). The parameter used to characterise the primary beam is the product between the FWHM and the frequency d. In principle it should be constant across the frequencies, depending only on the antennae diameter. In reality it can depend on the frequency because of different receivers and the change of the effective area of the antennae. The measurement of this parameter according to Wieringa et Kesteven (1992) is 47.90 for the first three frequencies and 49.70 for the other four (they used different receivers), since the primary beam is assumed to vary as ν^{-1} in a single receiver. New primary beam measurements show that this is not true[1] (see Table 6.1). The primary beam FWHM tends to decrease less rapidly than ν^{-1} below 2.1 GHz. It can be caused by a deterioration in the focus above 1.4 GHz. For a single pointing the correction factor would be:

$$P = \exp\left\{4\ln 2\left[\left(\frac{x}{d}\right)^2 - \left(\frac{x}{d'}\right)^2\right]\right\} \tag{6.1}$$

where x is the distance from the pointing centre multiplied by the frequency. In general, for n pointings we have:

$$P = \frac{\sum_{i=1}^{n} \exp\left[-4\ln 2\left(\frac{x_i}{d'}\right)^2\right] \cdot \exp\left[-4\ln 2\left(\frac{x_i}{d}\right)^2\right]}{\sum_{i=1}^{n}\left\{\exp\left[-4\ln 2\left(\frac{x_i}{d'}\right)^2\right]\right\}^2} \tag{6.2}$$

[1] `http://www.narrabri.atnf.csiro.au/people/ste616/beamshapes/beamshape_16cm.html`

ν (GHz)	d (arcmin GHz)	d' (arcmin GHz)
1.469	48.34	47.90
1.649	49.34	47.90
1.850	50.40	47.90
2.075	51.03	49.70
2.329	49.91	49.70
2.613	49.54	49.70
2.932	48.31	49.73

Table 6.1: Product of the primary beam FWHM and frequency at every SCORPIO sub-band, using the recent measurements of the primary beam for the new 16-cm CABB receiver (d) and the primary beam model by Wierenga & Kesteven (1992) (d').

Even with these corrections, we found a shift in the synchrotron peak of the spectral index distribution of ~ 0.2 towards the flatter spectra. Knowing that in the new `MIRIAD` upgrade, `LINMOS` has the right primary beam correction, we proceeded to recalibrate the data and to produce new maps, fixing the problem. The slight differences in the flux densities between the data in this thesis and the data in Paper I is due to this correction.

6.2 The joint approach map

In February 2014 we observed a region of the field for the first time in compact configuration: the Galactic Plane ($|b| < 0.5$) and 4 pointings that include the large source on top of Fig. 6.1. We will call this field the GP field. Our decision to re-observe SCORPIO using the compact configuration was motivated by the fact that including data from shorter baselines would have allowed us to well image more extended sources, increasing the LAS and lowering the flux density loss. We decided to test the MEM algorithm because the CLEAN algorithm is better suited for point sources, while the MEM algorithm does not present this issue. As stated in Chapter 4, we could not invert the whole field at once because that would overflow the fixed array size used by the task to store temporally the uv data, but, given the limited area of the considered region, smaller than the whole field, we managed to invert all the region pointings at once. In Haverkorn et al. (2006) the authors found out that the superuniform algorithm is better suited for large area field than the normal uniform algorithm, so we decided to `invert` our region with a

superuniform weight, modifying the robust value to -2 and the sup value to 2000, as in Haverkorn et al. (2006). To apply the MEM deconvolution, we used the `mosmem` task. It requires as input a flux density value or a map to use as a model. We used a low resolution CLEANED map as the `mosmem` model and obtained the map on Fig. 6.3. The map created with the MEM algorithm presents a better imaging of the extended sources (as an example we show a comparison in Fig. 6.4) but a worst imaging of the point sources imbedded in extended emission, as noticed in Section 4.3. This can be fixed using the peeling technique, as described in the Conclusions. Because we focused, until now, on the point sources, we decided not to use this map, preferring the CLEANed image.

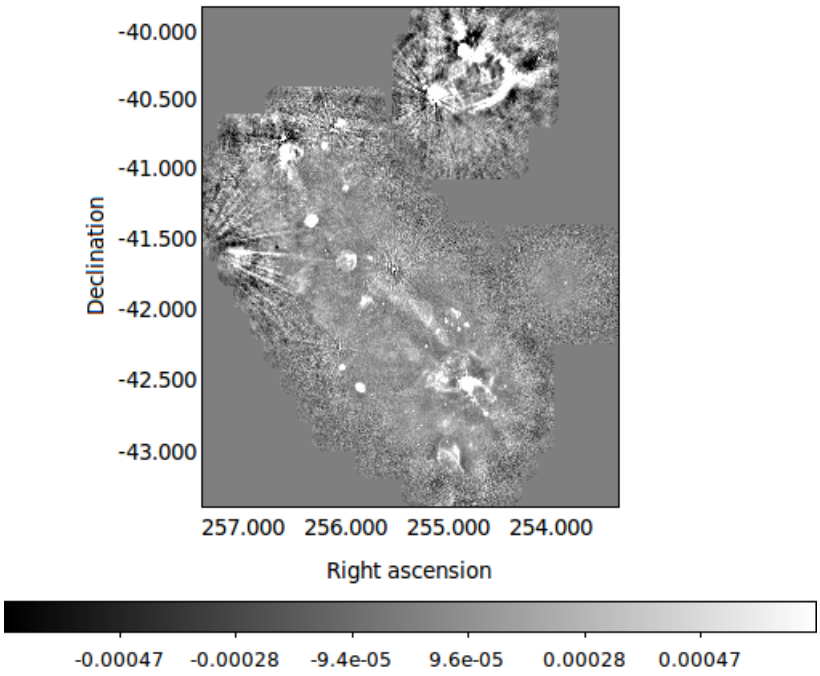

Figure 6.3: Map of the SCORPIO Galactic Plane done using `mosmem`.

6.3 Short baseline map

In January-February 2016 we observed in compact configuration the rest of the field. As written in Chap 4, we found out some calibration problem regarding the complex gain calibrator (see Section 4.6.2 for more details) and

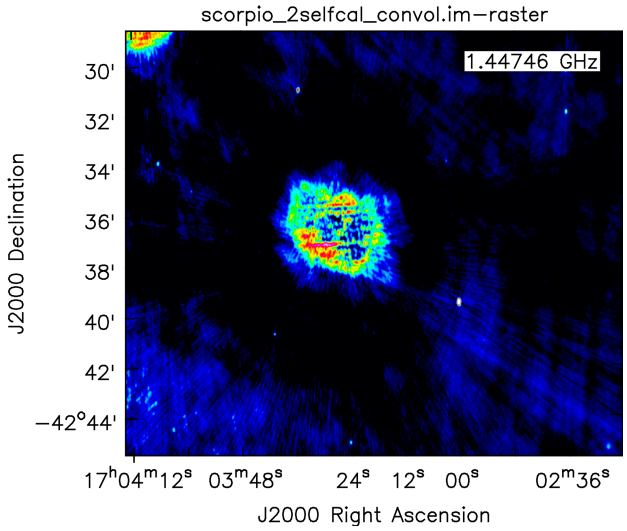

(a) Source deconvolved using the CLEAN algorithm

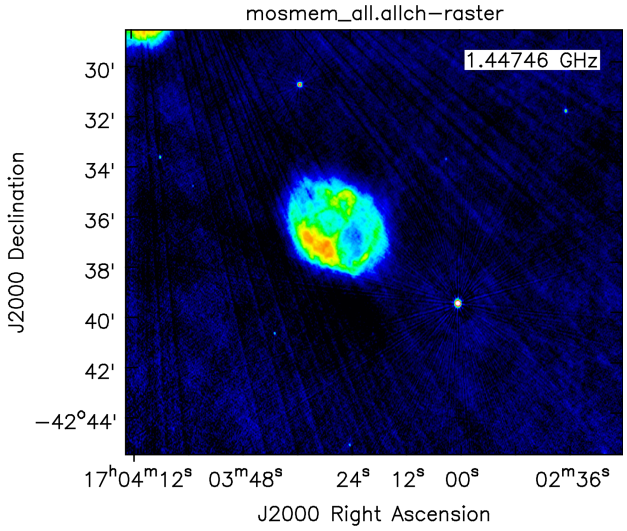

(b) Same source deconvolved using the MEM algorithm

Figure 6.4: An extended source of the SCORPIO field, deconvolved using the CLEAN and the MEM algorithm. The CLEANed source is badly imaged because of how the CLEAN algorithm works, assuming that sources are made of a collection of point sources.

we have not produced the final image from this dataset yet, but, from the preliminary results, we observed a better mapping of the extended source, as, for example, for the source shown in Fig. 6.5. Although the results are encouraging, showing that adding short baselines can effectively greatly improve the imaging, it is clear, from the missing flux around the source, with negative peaks of $\sim -200\,\mu$Jy, that we need shorter baselines or even single dish observations

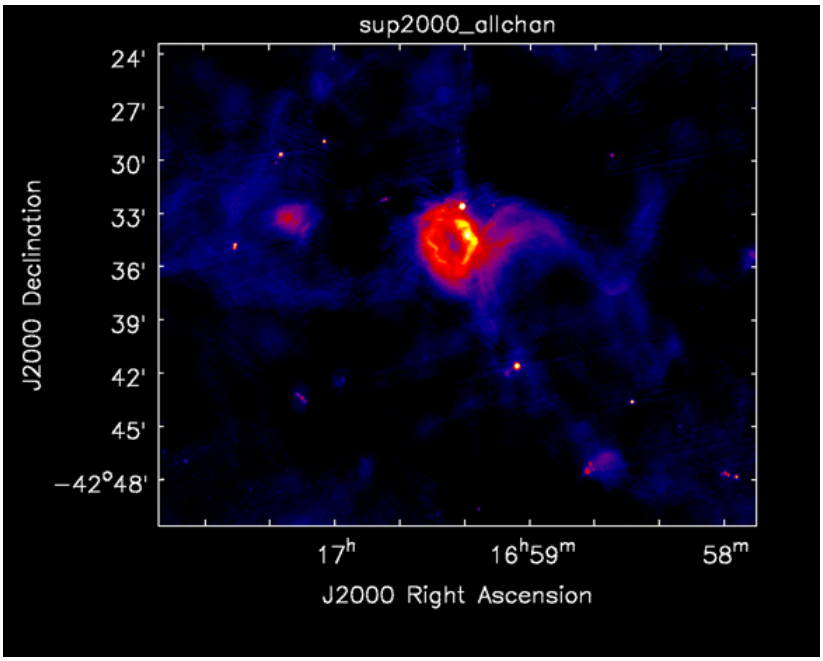

Figure 6.5: Region around the s17 adding up the short baselines from the compact configuration. Notice the differences with Fig. 6.2.

6.4 Polarisation maps

The polarisation of a source can give us a lot of information about it and give us hints about the emission mechanism. Knowing that a source is linearly polarised can tell us that the source emits thanks to a synchrotron mechanism. Furthermore, measuring the polarisation angle can give us information about the magnetic field between the source and the observer, thanks to the effect known as Faraday Rotation, an interaction between the light and the magnetic field that causes a rotation of the plane of polarisation. This effect is proportional to the squared wavelength, causing different polarisation angles at different frequencies. The presence of circular polarisation is symptomatic

of a coherent emission or gyrosynchrotron, e.g. MCP, flare stars, pulsars or the interaction between a satellite and the magnetosphere of the planet (e.g. Io and Ganymede with Jupiter). To calibrate the polarisation we need to set the option "qusolve" on the `gpcal` task.

The first imaged polarisation map was the Stokes V one (see Fig. 6.7). Stokes-V maps are usually "empty", featuring only white noise, because the circularly polarised sources are rare in respect of the non-circularly polarised ones. For this reason, the Stokes-V map can be regarded as a test to check for possible calibration issues. The map is effectively empty or almost empty (there are only 3 point sources, see next sections). The background noise of the Stokes-V map, measured as its rms, is $\sim 20\,\mu$Jy, exactly as expected on the basis of receiver thermal noise. In Fig. 6.8 it is shown how the rms depends on the Galactic latitude for Stokes V and I. At high Galactic latitude the rms of the Stokes I is similar to the Stokes V one but in the GP this is not true anymore. The higher rms of the Stokes V around the GP is due to the higher T_{sys}.

In Fig. 6.6 the Stokes Q map is shown. We did some tests on known extra-galactic source and we found polarisations around 1% in a single sub-band, while the average value for galaxies is 3.5% in Banfield et al. (2014). Given that the value considered by Banfield et al. (2014) is an average, our 1% do not seem unrealistic.

As stated before, the linear polarisation angle depends on the frequency because of the Faraday Rotation. This can cause, if we do not divide the band enough, a depolarisation of the source. The Faraday rotation on extragalactic source is easier to track because their light pass trough the whole Galaxy in the direction they are located, while the light from Galactic source interact only with the magnetic field of the Milky Way between them and the observer. If we assume a rotation measure through our Galaxy RM = 100 (Simard-Normandin, Kronberg, & Button, 1981) rad m^{-2} and knowing that (Burke & Graham-Smith, 2014):

$$\theta_1 - \theta_2 = \mathrm{RM}\left(\lambda_1^2 - \lambda_2^2\right) \tag{6.3}$$

if λ_1 corresponds to our highest frequency and λ_2 corresponds to our lowest one then $\theta_1 - \theta_2 \approx 200$ deg for extragalactic sources. This translates into a reduction of the polarised flux to 56% of the initial one. This is consistent with the data, we imaged an all-band polarisation map and found out that the polarisation was halved in respect of a sub-band map. In Fig. 6.6 is evident a difference between the pilot field and the rest of the SCORPIO field. This is probably due to the differences in flagging but we will investigate this issue deeply in the next months.

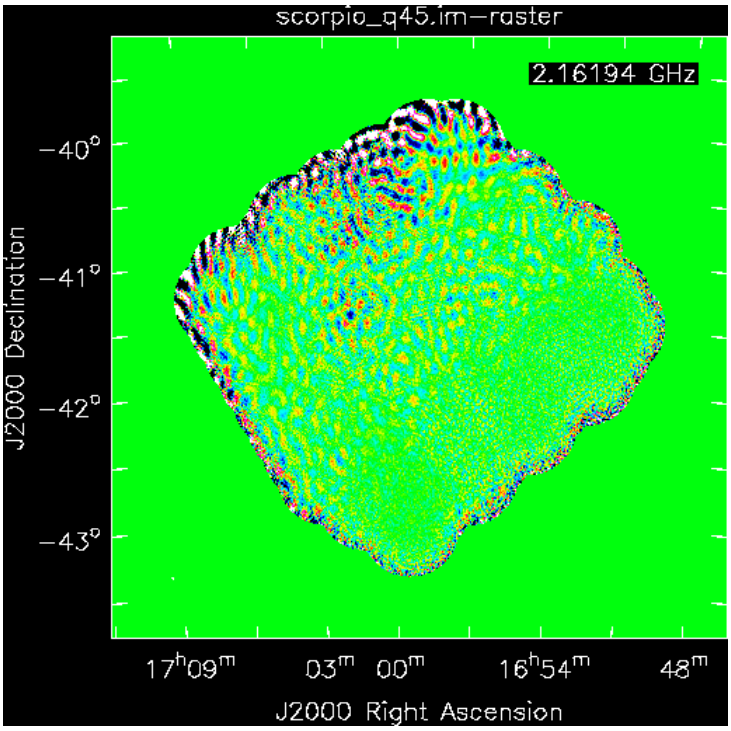

Figure 6.6: Stokes Q map of the SCORPIO field at the 4$^{\text{th}}$ sub-band.

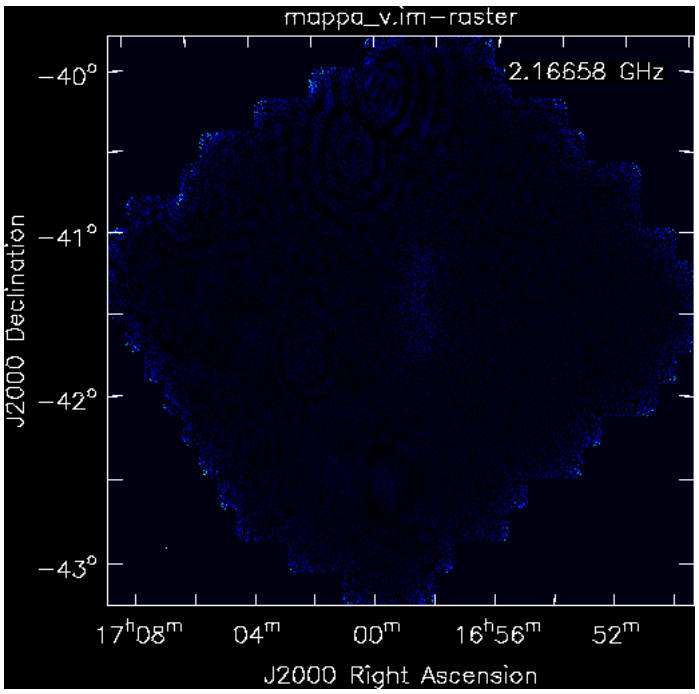

Figure 6.7: Stokes V map of the SCORPIO field.

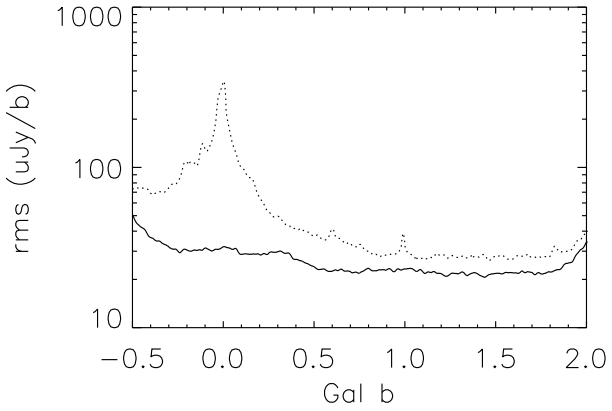

Figure 6.8: The rms as a function of the Galactic latitude for Stokes I (dashed line) and Stokes V (solid line). For each pixel of the map the rms has been averaged over 0.3 deg in longitude.

6.5 SCORPIO sources

In this section we describe the most interesting objects, from this thesis work point of view, among the more than 2000 sources detected in SCORPIO. First we focus on extended sources (mainly H II regions) and then on some interesting radio stars.

6.5.1 Extended source

Within the SCORPIO field we have found about 50 extended sources. A complete catalogue is in preparation. The extraction method that we are using is the visual inspection, however we plan to use also a new algorithm, the Compact And Extended Source Automated Recognition (CAESAR), described by Riggi et al. (2016). The algorithm can be divided into three main steps (see Fig. 6.9):

1. pre-filter the input map, removing point sources. The compact source filtering is done using a source extractor like BLOBCAT and it demands the construction of a background and noise map;

2. decompose the residual image into a set of superpixel (regions). The pixels on the same superpixel share similar properties;

3. merge the superpixel into larger regions of background or sources, depending on a threshold decided in the second step by the algorithm,

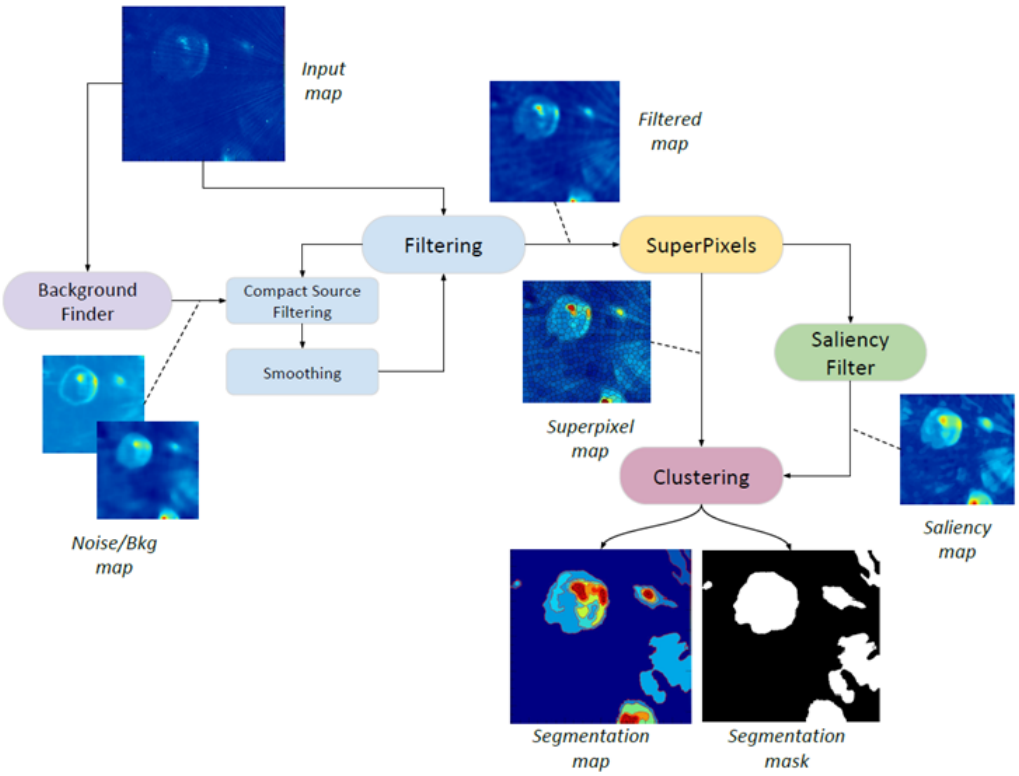

Figure 6.9: Flowchart of the CAESAR algorithm

taking into account the background and the noise maps.

The SCORPIO field is still small enough to allow a single astronomer to search for extended sources but, in the future surveys, the visual inspection will not be feasible. This double search will then be used as a test for the reliability of the CAESAR algorithm in "real-life" conditions.

The classification of these extended sources is usually hard if only radio data are available. In these cases infrared images turn out to be extremely useful. They in fact may supply complementary information with respect to radio and help shedding light on the nature of the studied sources. We found 15 Simpson isolated bubbles (Simpson et al., 2012), selected by Bufano et al. (submitted) and called Simpson Gold sample. A bubble is defined as an extended emission detected in the infrared, ring or shell-shaped. The presence of a source in both the SCORPIO and Simpson catalogues tells us that it has both an infrared and radio emission. With a more detailed inspection we could classify the source, the study is in preparation. We also found several matches between SCORPIO and the Anderson et al. (2014) H II region catalogue. The H II regions on the Anderson et al. (2014) catalogue are visually searched around the GP ($|b| \leq 8°$) in the WISE 12 μm and 22 μm images. The first selection is morphologic. Then all the sources with WISE colour $[F_{12}/F_{22}] < 0.5$ and $F_{12} > 15$ are discarded as in Anderson et al. (2012), where F_{12} and F_{22} are the fluxes at 12 and 22 μm. They also look for recombination lines to discriminate the H II regions from the PNe. The authors also matched their catalogue with six radio surveys: MAGPIS (Helfand et al., 2006), VGPS (Stil et al., 2006), CGPS (Taylor et al., 2003), NVSS, SGPS (McClure-Griffiths et al., 2005) and SUMSS (Bock, Large, & Sadler, 1999)

The Anderson et al. (2014) catalogue classify the sources into 5 different groups, the known H II regions, the candidates, the regions that did not present a radio emission at the time of the catalogue release, called radio quiet regions, the H II regions group and the regions that have no radio observation available at the time of the release. We found:

- 30 confirmed H II regions;
- 11 H II region candidates;
- 12 radio quiet H II regions;
- 3 groups of HII regions.

It is really interesting to find 12 over a total of 84 radio quiet H II regions detected in radio. This is due to the higher sensitivity of SCORPIO with

respect to the SGPS survey, the survey used by Anderson et al. (2014) at the SCORPIO Galactic longitude. In Fig. 6.10 a sample of confirmed H II region is reported, while in Fig. 6.11 we show a sample of radio quiet ones.

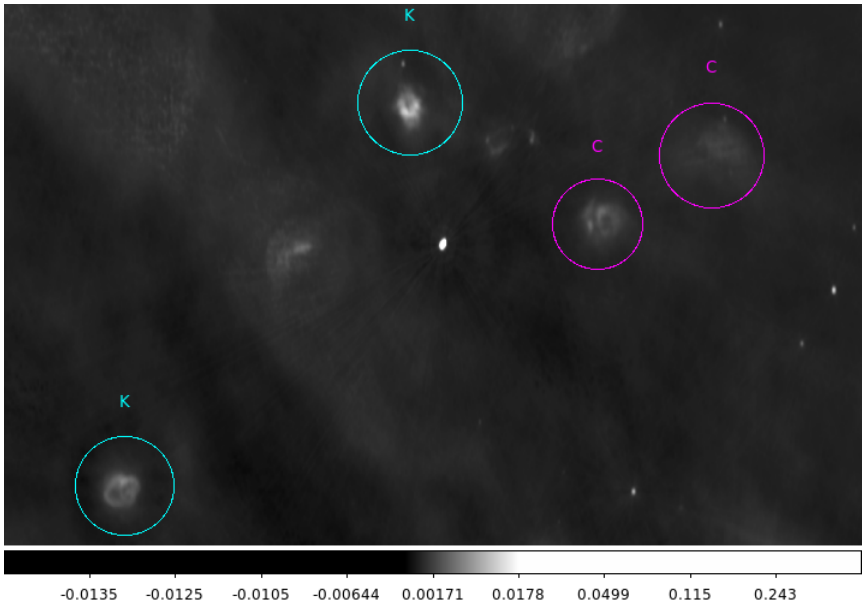

Figure 6.10: Four sources from the Anderson et al. (2014) catalogue. The "K" regions denote a confirmed H II region while the "C" ones denote a candidate.

6.5.2 Radio Stars

As reported in Paper I, we have 34 sources matching with SIMBAD and, among them, there are 10 stars. SIMBAD is an astronomical database storing cross identifications, bibliography and measurements of obsects outside our solar system. It is mostly focused on stellar objects. Our 10 stars with their spectral indices extracted as in Section 5 are:

- SCORPIO1_534: classified as a star in SIMBAD, it is embedded in a extended radio emission (see Fig. 6.12). Its SCORPIO flux density at 2.1 GHz is 7 ± 1 mJy while its spectral index is $\alpha = -0.20 \pm 0.18$, consistent with a flat spectrum;
- SCORPIO1_012: associated with ζ^1 Sco, it is classified as a variable Blue Hypergiant (see Fig. 6.13). Its flux density is 1.2 ± 0.1 mJy and its spectral index is $\alpha = 0.65 \pm 0.35$, consistent with a stellar wind emission;

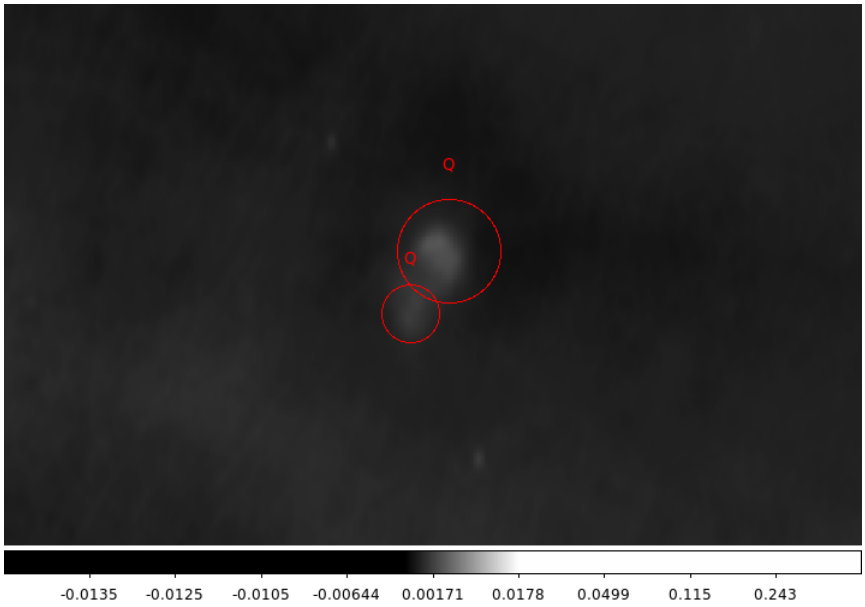

Figure 6.11: Two sources from the Anderson et al. (2014) catalogue classified as radio quiet. As it is shown, they are detected in SCORPIO.

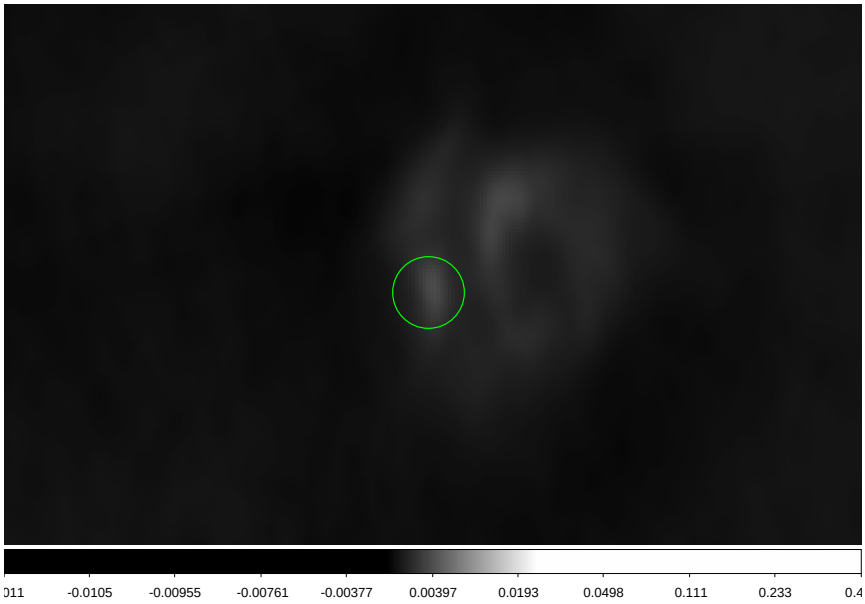

Figure 6.12: The source SCORPIO1_534 and its candidate H II region envelope.

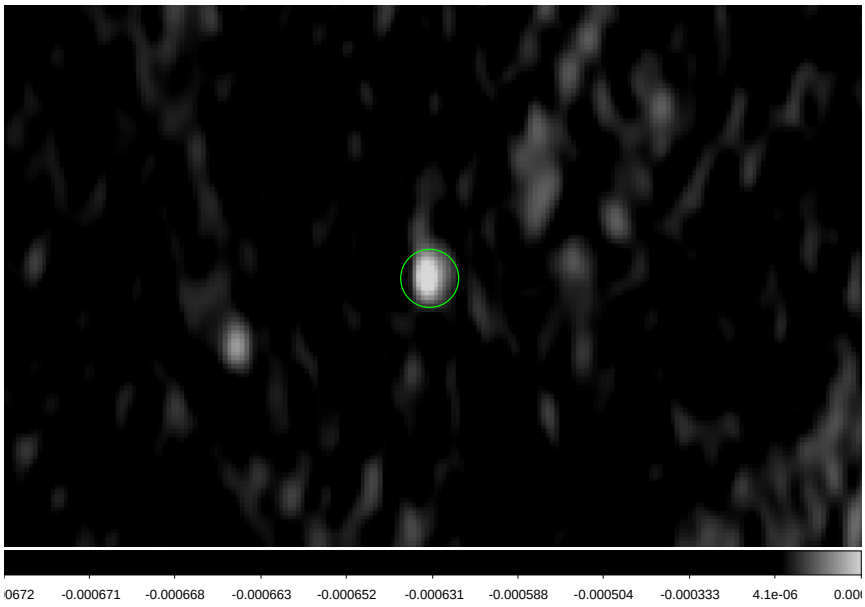

Figure 6.13: The source SCORPIO1_12, ζ^1 Sco.

- SCORPIO1_118: this is classified as a WR star and it is a known radio source (Bieging et al. 1982; Abbott et al. 1986; Hogg 1989; Leitheree et al. 1991 at 1.3 mm). The measured spectral index is $\alpha = -0.6 \pm 0.4$, consistent with a non-thermal emission. Given that the radio emission at 1.3 mm is 11.6 ± 2.3 mJy, the spectral index estimated between the SCORPIO flux (0.85±0.05) and the millimetre one is, instead, consistent with a stellar wind emission ($\alpha_{\rm SED} \approx 0.55$). This could be the case of a shocked wind with an emission dominated by synchrotron at low frequencies and stellar wind at high frequencies. See Fig. 6.14;

- SCORPIO1_311: WC7+O6V star, already known as a radio source (Bieging et al. 1982; Abbott et al. 1986; Hogg 1989). Its flux density is 0.54 ± 0.04 and its spectral index is $\alpha = -0.07 \pm 0.35$, consistent with a flat spectrum, maybe the result of the sum of the wind-colliding non-thermal component and the stellar wind component (see Fig. 6.15);

- SCORPIO1_468: this is classified as a Young Stellar Object candidate. Its flux density is 13 ± 0.4 and its spectral index is $\alpha = 0.01 \pm 0.05$, consistent with a flat spectrum (see Fig. 6.16);

- SCORPIO1_243: it is reported simply as a star. Its flux density is 7.7 ± 0.2 and its spectral index, $\alpha = 0.36 \pm 0.03$, is consistent with a

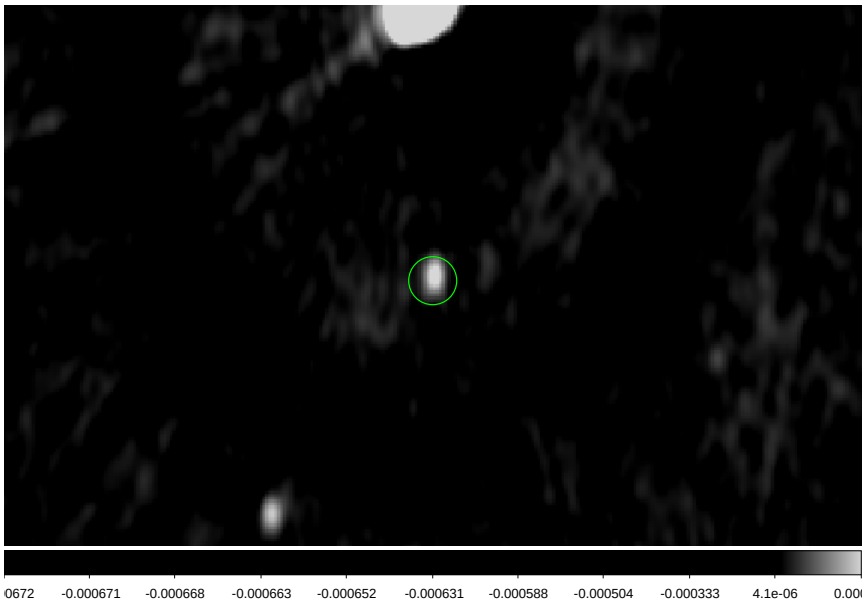

Figure 6.14: The source SCORPIO1_118.

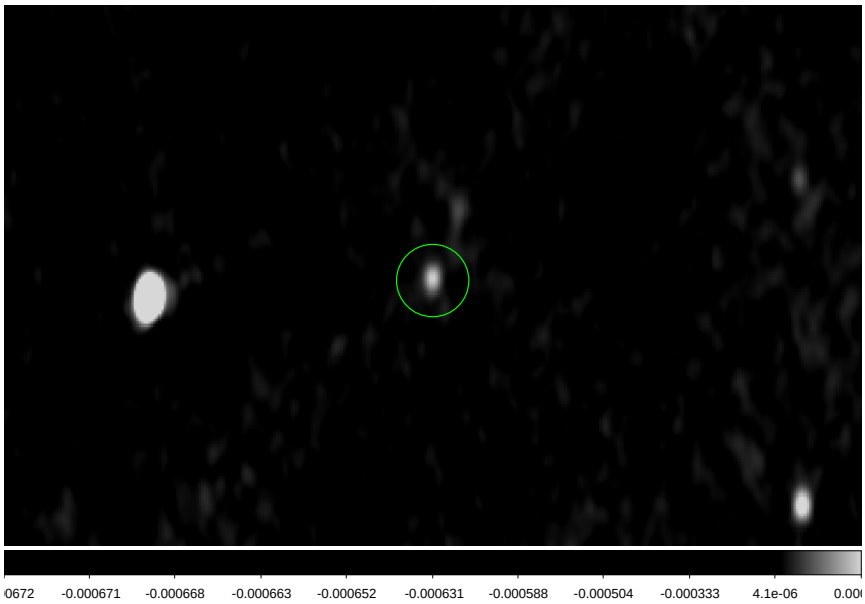

Figure 6.15: The source SCORPIO1_311.

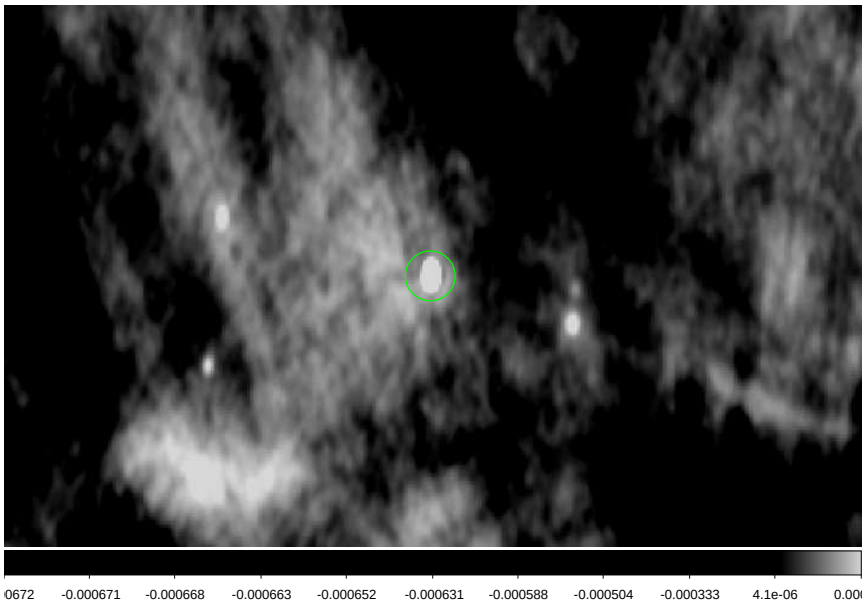

Figure 6.16: The source SCORPIO1_468.

optically thick thermal bremsstrahlung (see Fig. 6.17);

- SCORPIO1_219: this is a known Herbig Ae/Be star, surrounded by an extended envelope detected at sub-mm wavelengths (Mannings, 1995). Its flux density is 9.2 ± 0.7 and its spectral index, $\alpha = -1.0 \pm 0.4$, is consistent with a non-thermal emission (see Fig. 6.18);

- SCORPIO1_406 and SCORPIO1_350: they are classified as Star in Cluster (Sung et al., 1998) (see Fig. 6.19). The first one is embedded in a extended radio emission, its flux density is 5.0 ± 0.4 and it has a spectral index of $\alpha = -0.1 \pm 0.1$, consistent with a flat spectrum, the second one is classified as a B8.5V star, its flux density is 0.5 ± 0.04 and it has no reliable spectral index.

Furthermore, in the whole field, there are 8 pulsars (Manchester et al., 2005), 6 of them are detected and two present a stokes V flux. We also found another source presenting a stokes V flux, that matches with a SIMBAD source, HD151965, classified as a CP variable star, with a stokes V emission around 10% (see Fig. 6.20). Its magnetic field vary between 1000 and 4000 G (Bychkov, Bychkova, & Madej, 2005) with a period $P = 1.60841$ d (Lanz & Mathys, 1991). In Fig. 6.21 it is showed the final map with a zoom on several sources, prototype of different radio source classes.

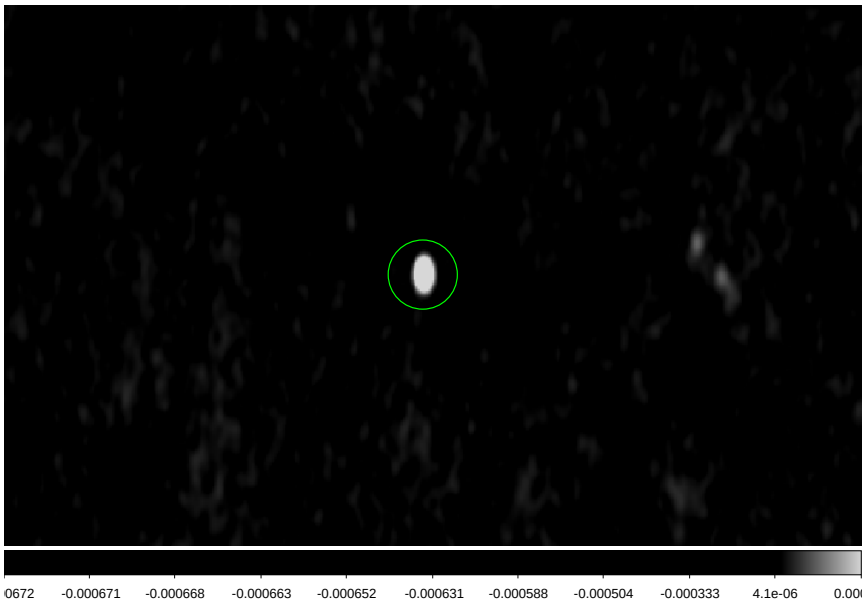

Figure 6.17: The source SCORPIO1_243.

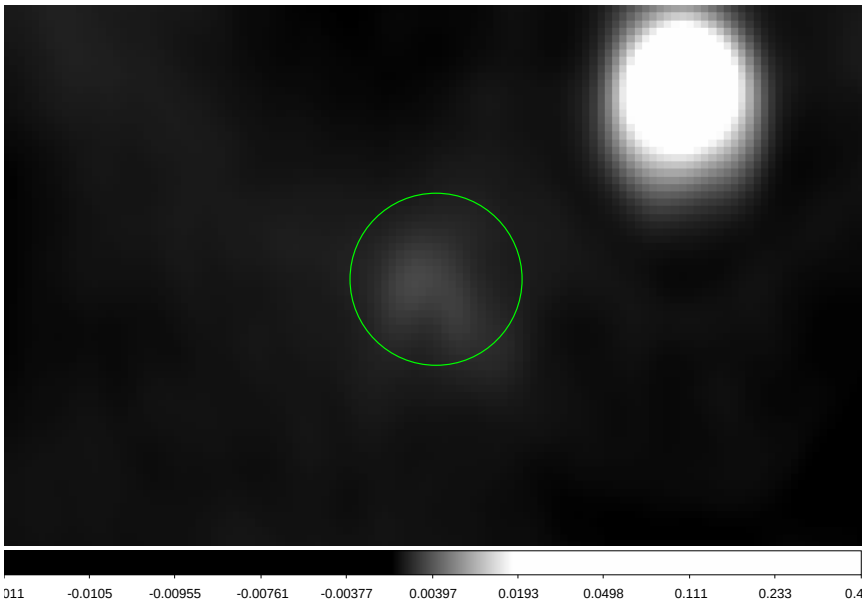

Figure 6.18: The source SCORPIO1_219.

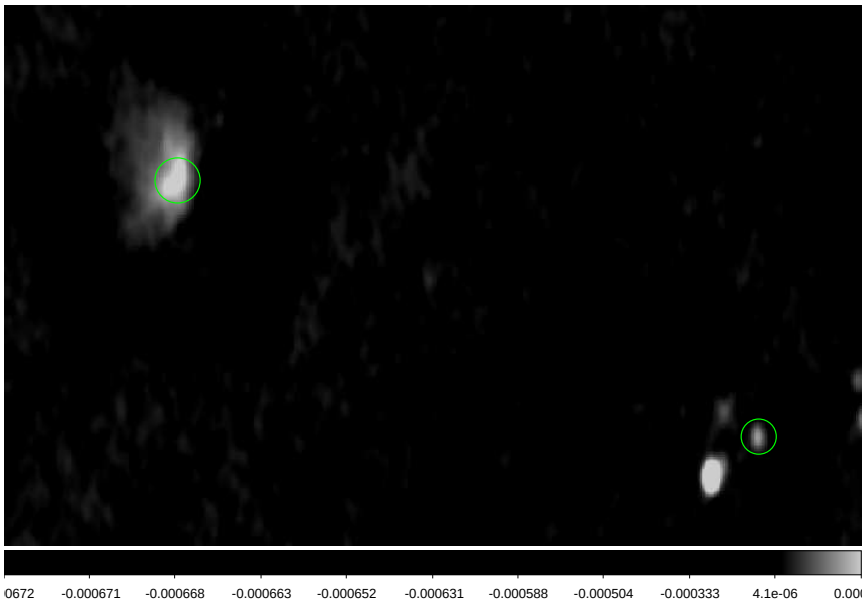

Figure 6.19: The sources SCORPIO1_406 and SCORPIO1_350.

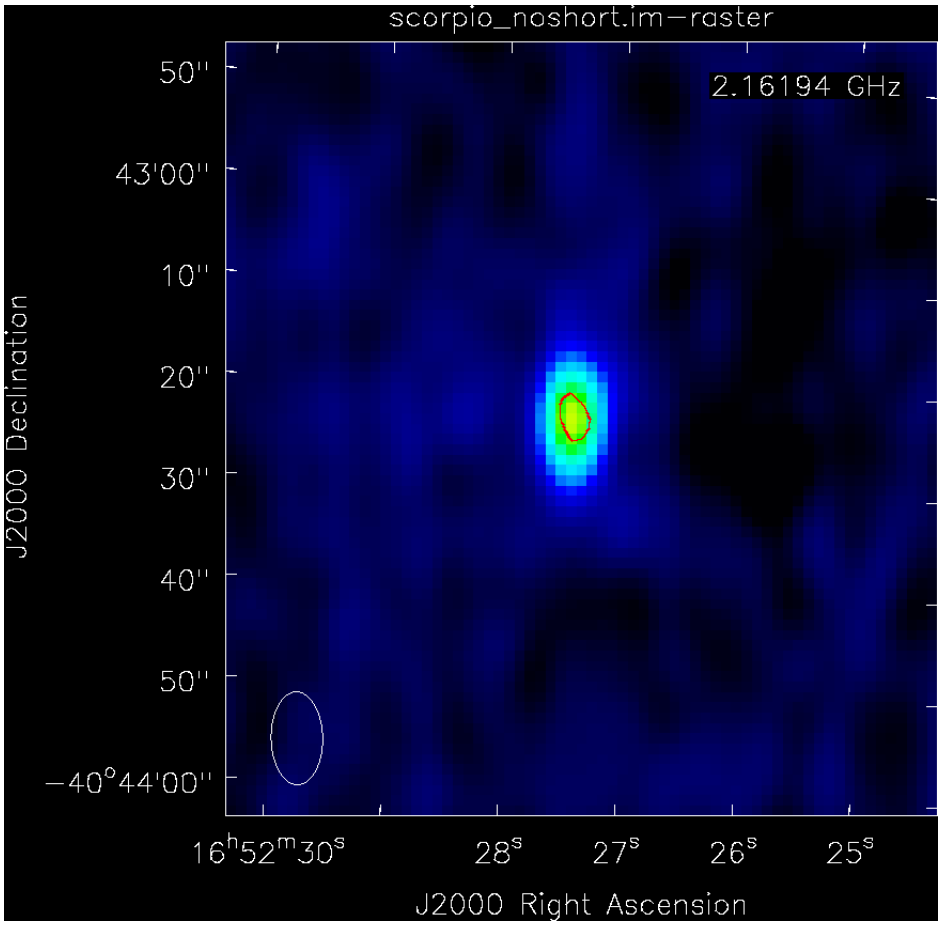

Figure 6.20: HD151965, detected in SCORPIO. The red line inside is the 3σ contour of the Stokes V emission.

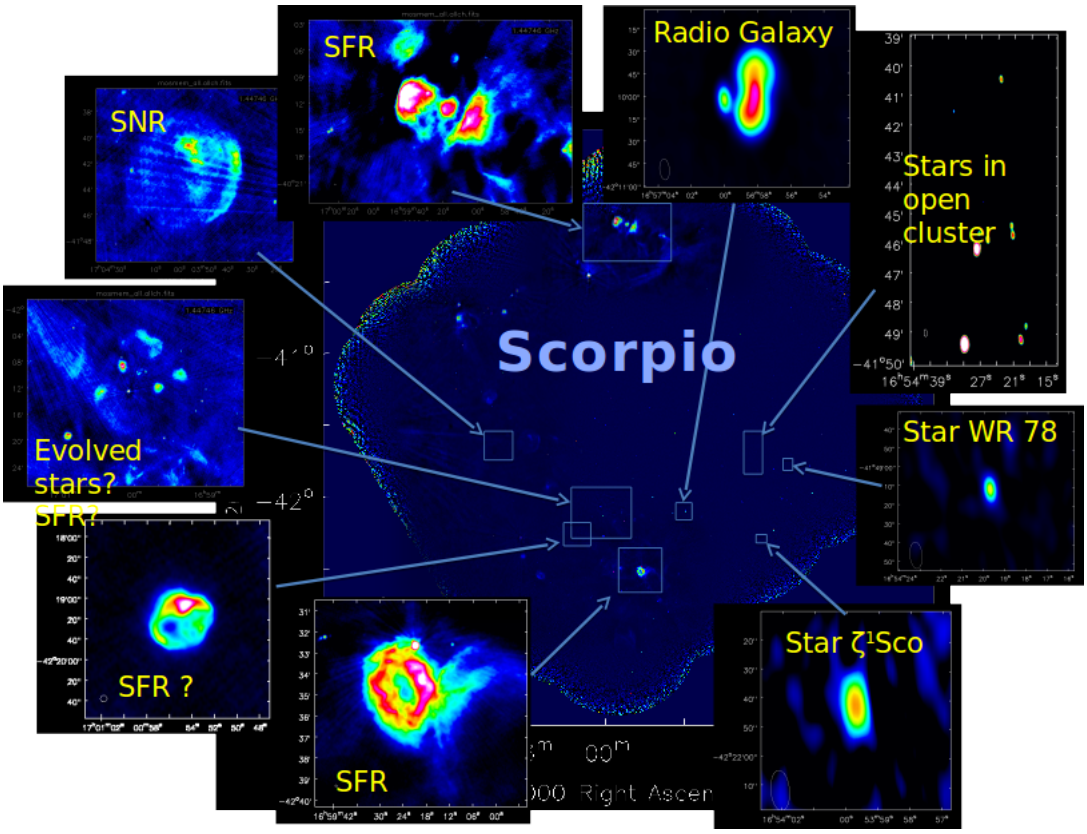

Figure 6.21: Final map of SCORPIO with a zoom on several sources. From the bottom left, going clockwise: S17, a star forming H II region; a candidate H II region; several H II regions candidates; a Supernovae Remnant; a huge H II region; a radio galaxy; several sources comprising a couple of sources matching with stars in open cluster; WR 79, a Wolf-Rayet star and ζ^1 Scorpii, a blue hypergiant in the Scorpio constellation.

Chapter 7

Conclusions

7.1 Summary

The work described in this thesis lies in the wide context of the SCORPIO project. In particular, we focused on the radio stars and on the characterisation of radio sources, resolving the issues coming from the Galactic Plane discussed in Section 4.1 in preparation of the future large area surveys.

The main goal of our work is to estimate the number of stars that we expect in the future radio surveys, such as EMU. We approached the problem from two direction. The first approach is the theoretical one. We estimated the number of radio stars on the basis of the Robin et al. (2003) Galactic model and on some assumptions on the radio emission of different stellar classes. The second approach, the observational one, tries to estimate the number of radio stars studying the blind survey SCORPIO (Umana et al., 2015b).

In the theoretical approach, we gave an estimate of the number of radio stars that we expect to detect at different sensitivity in Chapter 3, focusing on flare, OB, MCP and RS CVn stars. The results does not take into account the H II regions and the evolved stars since in radio they are brighter than a star without envelope. This should translate into more detections than the predicted. We can estimate, from the results in Section 3.3.5, the expected number of stars detected in EMU. We know that EMU will observe 75% of the sky and so it will observe about 75% of the GP. Given that ASKAP is in the southern hemisphere and the Galactic centre is visible in the southern half of the sky, we will assume that EMU, at galactic latitude $-1 < b < 1$, will observe the entire region at galactic longitude $-30 < l < 30$, 50% of the region at $150 < l < 210$ and 75 % of the remaining regions. To simplify it, we will assume a homogeneous 75 % at higher galactic latitude. The

total number of stars $N_{\rm tot}$ will be the sum of several terms $N\left(b_{\rm i}, l_{\rm j}\right)$, where b_0 represents $-1 < b < 1$, b_1 represents $1 < b < 3$ and $-3 < b < -1$, b_2 represents $3 < b < 23$ and $-23 < b < -3$ and b_3 represents the remaining values, while l_0 represents $-30 < l < 30$, l_1 represents $30 < l < 90$ and $270 < l < 330$, l_2 represents $90 < l < 150$ and $210 < l < 270$ and l_3 represents $150 < l < 210$. In general we will have

$$N\left(b_{\rm i}, l_{\rm j}\right) = A\left(n_{\rm OB}\left(b_{\rm i}, l_{\rm j}\right) + n_{\rm MCP}\left(b_{\rm i}, l_{\rm j}\right) + n_{\rm Flare}\left(b_{\rm i}, l_{\rm j}\right) + n_{\rm RSCVn}\left(b_{\rm i}, l_{\rm j}\right)\right) \quad (7.1)$$

where n are the surface densities of the considered classes and A is the surface of the observed region of the sky. Using the results presented in Tables 3.4, 3.5, 3.6 and 3.7, we have

$$N\left(b_{\rm i}, l_{\rm j}\right) = \sum_{\rm i=0}^{3} \sum_{\rm j=0}^{3} N\left(b_{\rm i}, l_{\rm j}\right) \approx 250\,000 \quad (7.2)$$

We expect $\sim 95\%$ of them to be flare stars, that will dominate even at low galactic latitude. SKA-1 will have a greater impact on the stellar astrophysics, starring a ~ 2 orders of magnitude increase over EMU in terms of stars detected, from $\sim 250\,000$ to $\sim 50\,000\,000$

In Chapter 4 we showed the reduction of the SCORPIO data using `MIRIAD` tasks. The region around the GP ($-0.5 < b < 0.5$) is embedded in diffuse emission and there are a lot of extended sources so the reduction proved particularly difficult. A parallelisation of the CLEAN was implemented in the usual pipeline using python libraries, to take advantage of the large number of cores available in the modern computers and clusters. We achieved, at the end, an rms of $\sim 30\,\mu$Jy/beam at high galactic latitude, $\sim 200\,\mu$Jy in the GP.

We gave an estimate of the number of galactic radio sources brighter than 1 mJy and a way to discriminate them from the extragalactic source in Chapter 5 from an observational approach. We expect, as stated in Section 5.3, 10 800 Galactic sources brighter than 1 mJy in the EMU survey. This, combined with the results from the paragraph before, will help us planning the image analysis of the future surveys and in particular EMU, giving as a guide line on how many radio stars and galactic sources we should expect.

In Chapter 6 we focused on the imaging and on some of the sources in the SCORPIO field, analysing the encountered issues and showing that, cross-matching the sources with other wavelength catalogues, it is possible to individuate stars in a blind surveys. In particular we found 9 stars in the pilot field thanks to the SIMBAD cross-match, 6 pulsars in the entire field and one MCP star outside the pilot thanks to the cross-match with the Stokes V image. This shows how important the Stokes V is for Galactic studies, in particular for radio stars and pulsars.

7.2 Future works

We will continue our work on the SCORPIO project in the next future, using also data from other radio telescopes, such as Parkes (Parkes observations have already been carried out in April 2016, data reduction is in progress) and ASKAP. We are currently waiting for the SCORPIO ASKAP12 data to test all the work done on SCORPIO and the issues of imaging 36 ASKAP beams, using also the Parkes data to add zero-baseline data. Other works that we are planning are:

1. extend the spectral index analysis to the whole field. This work is almost complete and will increase our statistics by a large margin, making our results more reliable;

2. calibrate the short baselines data applying a self calibration on the secondary calibrator. This is a mandatory step to include the short baselines into our project and to better study the extended sources;

3. improve the imaging, using the "peeling" technique. It consists in modeling the image and doing successive iteration of estimation of the calibration parameter and subtraction of a single source. When the brightest source is removed, it is possible to pass to the second one. This technique could greatly decrease the artefacts of the image. It can also be used to subtract the point sources embedded in diffuse emission from a field to prepare it for the MEM algorithm (see Section 4.3);

4. build a catalogue of all the sources detected in the whole field, both point-like and extended ones, including spectral indices and other catalogue matchings.

5. improve the polarisation maps, dividing the sub-bands into smaller ones and investigating the difference between the pilot and the rest of the field described in Section 6.4

As summarised in Section 7.1, the SCORPIO project produced interesting results, both technical and scientific. We are currently looking forward to the new outcomes that we expect in some months and, in particular, to the ASKAP12 observation of the field, given that it will be the perfect test bed for Galactic EMU.

Acknowledgements

Firstly I want to express my gratitude to my tutor Prof. Corrado Trigilio for the support that he gave me on my Ph.D. study, following me patiently and always trusting me. I'm really glad he was my tutor.

I want to thank my supervisor, Prof. Francesco Leone and my co-supervisor in CASS (CSIRO Astronomy and Space Science), Prof. Raymond P. Norris, for their continuous help and their guide in the research.

This work was carried out in collaboration between Università di Catania and CASS in Sydney, through the CASS Graduate Student Program. I want to thank Dr. George Hobbs and Dr. Julie Tesoriero for being responsible for the program.

I would like to thank also the institution that supported this work: Università di Catania that granted the scholarship, INAF-OACT (Istituto Nazionale di Astrofisica - Osservatorio di Catania) and CASS that had me as a guest in Sydney and in Narrabri, in the ATCA site.

I want to thank the director of the INAF-OACT, Dr. Grazia Umana, the Ph.D. Coordinator, Prof. Vincenzo Bellini and the tutor of the Astrophysics Ph.D. students, Prof. Rossella Caruso.

My thanks go also to my referees, Prof. Carlo Stanghellini and Prof. Daniele Dallacasa, for their insightful comments on the thesis and their hints on the work to do to improve it.

My sincere thanks go to the research group I worked with, for giving me the opportunity to work with them. In alphabetical order, Dr. Carla Buemi, Dr. Milena Bufano, Dr. Paolo Leto, Dr. Simone Riggi, Dr. Francesco Schillirò, Dr. Grazia Umana and, in particular, Dr. Adriano Ingallinera, for helping me in the thesis work and always supporting me.

My thanks go also to Dr. Joshua Marvil and Dr. Thomas Franzen, for their help in my research and the knowledge that they shared with me.

I want to thank the visitor centre staff of CASS, Vicki Drazenovic, Leanne Edwards and Jayde Clayton for helping me in every kind of issues in a foreign country, to Nathan Pope, Robin Wark and Philip Edwards for helping me with the facilities and to all the staff of CASS and Narrabri.

I want to thank my father, my mother, my brother Fabio, my grandma and all my uncles, aunts and cousins, my friends and the boy-scouts and, in particular, Elena, for spiritually supporting me in all those years, contributing in making me what I am.

Last but not the least, I want to thank all the fantastic people that I met in Australia, for making me feel at home on the other side of the planet.

Bibliography

Abbott D.C., Bieging J.H., Churchwell E., Torress A.V., 1986, ApJ, 303, 239

Anderson L. D., Zavagno A., Barlow M. J., García-Lario P., Noriega-Crespo A., 2012, A&A, 537, A1

Anderson L. D., Bania T. M., Balser D. S., Cunningham V., Wenger T. V., Johnstone B. M., Armentrout W. P., 2014, ApJS, 212, 1

Bagchi M., 2013, IJMPD, 22, 1330021

Banfield J. K., Schnitzeler D. H. F. M., George S. J., Norris R. P., Jarrett T. H., Taylor A. R., Stil J. M., 2014, MNRAS, 444, 700

Becker R. H., White R. L., Helfand D. J., 2006, AIPC, 840, 102

Bensby T., Feltzing S., 2010, IAUS, 265, 300

Bell A. R., 1978, MNRAS, 182, 147

Bell A. R., 1978, MNRAS, 182, 443

Benjamin R. A., et al., 2003, PASP, 115, 953

Berger E., 2006, ApJ, 648, 629

Bieging J. H., Cohen M., Schwartz P. R., 1984, ApJ, 282, 699

Bihr S., et al., 2016, A&A, 588, A97

Bieging J. H., et al., 1982, ApJ, 263, 207

Bieging J. H., Abbott D. C., Churchwell E. B., 1989, ApJ, 340, 518

Bock D. C.-J., Large M. I., Sadler E. M., 1999, AJ, 117, 1578

Bridle A. H., Hough D. H., Lonsdale C. J., Burns J. O., Laing R. A., 1994, AJ, 108, 766

Briggs D. S., 1995, AAS, 27, 112.02

Brook C. B., Kawata D., Gibson B. K., Freeman K. C., 2004, ApJ, 612, 894

Burke B. F., Graham-Smith F., 2014, ira..book,

Bychkov V. D., Bychkova L. V., Madej J., 2005, A&A, 430, 1143

Carey S. J., et al., 2009, PASP, 121, 76

Carilli C. L., Rawlings S., 2004, NewAR, 48, 979

Catalano F. A., Leone F., 1994, ASPC, 60, 110

Chippendale A. P., et al., 2015, isap.conf, 1

Churchwell E., et al., 2009, PASP, 121, 213

Clark B. G., 1980, A&A, 89, 377

Cohen M., Chapman J. M., Deacon R. M., Sault R. J., Parker Q. A., Green A. J., 2006, MNRAS, 369, 189

Condon J. J., Cotton W. D., Greisen E. W., Yin Q. F., Perley R. A., Taylor G. B., Broderick J. J., 1998, AJ, 115, 1693

Contreras Y., et al., 2013, A&A, 549, A45

Cornwell T., Braun R., Briggs D. S., 1999, ASPC, 180, 151

Crézé M., Chereul E., Bienayme O., Pichon C., 1998, A&A, 329, 920

Cutri R. M., et al., 2003, tmc..book,

Cutri R. M., et al., 2013, wise.rept,

Dame T. M., 1993, AIPC, 278, 267

Deharveng L., et al., 2010, A&A, 523, A6

Donati J.-F., et al., 2008, MNRAS, 390, 545

Drake S. A., Abbott D. C., Bastian T. S., Bieging J. H., Churchwell E., Dulk G., Linsky J. L., 1987, ApJ, 322, 902

Duffy A. R., Meyer M. J., Staveley-Smith L., Bernyk M., Croton D. J., Koribalski B. S., Gerstmann D., Westerlund S., 2012, MNRAS, 426, 3385

Egan M. P., Price S. D., Kraemer K. E., 2003, AAS, 35, 57.08

Eker Z., et al., 2008, MNRAS, 389, 1722

Fanaroff B. L., Riley J. M., 1974, MNRAS, 167, 31P

Fanti R., 2009, AN, 330, 303

AMI Consortium: Franzen et al., 2011, MNRAS, 415, 2699

Franzen T. M. O., et al., 2015, MNRAS, 453, 4020

Frieden B. R., 1972, JOSA, 62, 511

Garmany C. D., Conti P. S., 1984, ApJ, 284, 705

Gomez A. E., Grenier S., Udry S., Haywood M., Meillon L., Sabas V., Sellier A., Morin D., 1997, ESASP, 402, 621

Gruenwald R., Aleman A., 2007, A&A, 461, 1019

Guedel M., Benz A. O., 1993, ApJ, 405, L63

Güdel M., 2002, ARA&A, 40, 217

Hales C. A., Murphy T., Curran J. R., Middelberg E., Gaensler B. M., Norris R. P., 2012, MNRAS, 425, 979

Hancock P. J., Murphy T., Gaensler B. M., Hopkins A., Curran J. R., 2012, ascl.soft, ascl:1212.009

Haverkorn M., Gaensler B. M., McClure-Griffiths N. M., Dickey J. M., Green A. J., 2006, ApJS, 167, 230

Hawley S. L., Davenport J. R. A., Kowalski A. F., Wisniewski J. P., Hebb L., Deitrick R., Hilton E. J., 2014, ApJ, 797, 121

Haywood M., Robin A. C., Creze M., 1997, A&A, 320, 440

Helfand D. J., Becker R. H., White R. L., Fallon A., Tuttle S., 2006, AJ, 131, 2525

Helou G., Walker D. W., 1988, iras, 7, 1

Hjellming R. M., 1988, gera.book, 381

Högbom J. A., 1974, A&AS, 15, 417

Hogg 1989, AJ, 98, 282

Humphreys R. M., Davidson K., 1994, PASP, 106, 1025

Ingallinera A., et al., 2016, MNRAS, 463, 723

Ishihara D., et al., 2010, A&A, 514, A1

Jahreiss H., 2003, ANS, 324, 96

Jarvis M., 2015, fers.conf, 7

Johnston S., et al., 2008, ExA, 22, 151

Kass R. E., Raftery A. E., 1995, Journal of the American Statistical Association 90 (430), 773, 795

Kurtz S., 2005, IAUS, 227, 111

Laing R. A., Bridle A. H., 1987, MNRAS, 228, 557

Lanz T., Mathys G., 1991, A&AS, 90, 365

Leitheree et al., 1991, ApJ, 377, 629

Leone F., Trigilio C., Umana G., 1994, A&A, 283, 908

Leone F., Trigilio C., Neri R., Umana G., 2004, A&A, 423, 1095

Linsky J. L., Drake S. A., Bastian T. S., 1992, ASPC, 26, 325

Manchester R. N., Hobbs G. B., Teoh A., Hobbs M., 2005, AJ, 129, 1993

Mannings V., 1995, Ap&SS, 224, 185

McClure-Griffiths N. M., Dickey J. M., Gaensler B. M., Green A. J., Haverkorn M., Strasser S., 2005, ApJS, 158, 178

McMullin, J. P., Waters, B., Schiebel, D., Young, W., Golap, K. 2007, Astronomical Data Analysis Software and Systems XVI (ASP Conf. Ser. 376), ed. R. A. Shaw, F. Hill, D. J. Bell (San Francisco, CA: ASP), 127

Mihalas D., Binney J., 1981, ed. 2, Galactic Astronomy: Structure and Kinematics, W. H. Freeman and company, New York

Miller-Jones J. C. A., Kapinska A. D., Blundell K. M., Stappers B., Braun R., 2007, wmdr.conf, 11

Mioduszewski A. J., Rupen M. P., Hjellming R. M., Pooley G. G., Waltman E. B., 2001, ApJ, 553, 766

Molinari S., et al., 2010, PASP, 122, 314

Morin J., et al., 2008, MNRAS, 390, 567

Morin J., Donati J.-F., Petit P., Delfosse X., Forveille T., Jardine M. M., 2010, MNRAS, 407, 2269

Murphy T., Mauch T., Green A., Hunstead R. W., Piestrzynska B., Kels A. P., Sztajer P., 2007, MNRAS, 382, 382

Mutel R. L., Morris D. H., Doiron D. J., Lestrade J. F., 1987, AJ, 93, 1220

Norris R. P., et al., 2006, AJ, 132, 2409

Norris R. P. et al., 2011, PASA, 28, 215

Norris R., Basu K., Brown M., Carretti E., Kapinska A. D., Prandoni I., Rudnick L., Seymour N., 2015, aska.conf, 86

Offringa A. R., de Bruyn A. G., Biehl M., Zaroubi S., Bernardi G., Pandey V. N., 2010, MNRAS, 405, 155

Panagia N., 1973, AJ, 78, 929

Panagia N., Felli M., 1975, A&A, 39, 1

Parra R., Conway J. E., Diamond P. J., Thrall H., Lonsdale C. J., Lonsdale C. J., Smith H. E., 2007, ApJ, 659, 314

Perryman M. A. C., et al., 1997, A&A, 323, L49

Peterson W. M., Mutel R. L., Güdel M., Goss W. M., 2010, Natur, 463, 207

Preston G. W., 1974, ARA&A, 12, 257

Purcell C. R., Hoare M. G., 2010, HiA, 15, 781

Rahman S. F. u., 2015, CaJPh, 93, 384

Randall K. E., Hopkins A. M., Norris R. P., Edwards P. G., 2011, MNRAS, 416, 1135

Rau U., Bhatnagar S., Owen F. N., 2016, arXiv, arXiv:1605.07640

Reynolds J. E., 1994, Technical Report No. 39.3/040, A Revised Flux Scale

Riggi S., et al., 2016, MNRAS, 460, 1486

Robin A. C., Reylé C., Derrière S., Picaud S., 2003, A&A, 409, 523

Salpeter E. E., 1955, ApJ, 121, 161

Schönrich R., Binney J., 2009, MNRAS, 396, 203

Schwab F. R., 1984, AJ, 89, 1076

Schwarz, Gideon E., 1978, Annals of statistics 6 (2), 461, 464

Seaquist E. R., 1993, RPPh, 56, 1145

Skrutskie M. F., et al., 2006, AJ, 131, 1163

Simard-Normandin M., Kronberg P. P., Button S., 1981, ApJS, 45, 97

Simpson R. J., et al., 2012, MNRAS, 424, 2442

Smith K., Pestalozzi M., Güdel M., Conway J., Benz A. O., 2003, A&A, 406, 957

Spiegel E. A., Zahn J.-P., 1992, A&A, 265, 106

Steinmetz M., 2012, AN, 333, 523

Jamie Stevens, Robin Wark, Phil Edwards, Shari Breen, and Karen Lee-Waddell, 2016, ATCA Users Guide

Stil J. M., et al., 2006, AJ, 132, 1158

Sung H., Bessell M.S., Lee S.W. 1998, AJ, 115, 734

Taylor A. R., et al., 2003, AJ, 125, 3145

Thompson A. R., 1999, ASPC, 180, 11

Trigilio C., Leto P., Leone F., Umana G., Buemi C., 2000, A&A, 362, 281

Trigilio C., Leto P., Umana G., Leone F., Buemi C. S., 2004, A&A, 418, 593

Trigilio C., Leto P., Umana G., Buemi C. S., Leone F., 2008, MNRAS, 384, 1437

Umana G., Catalano S., Rodono M., 1991, A&A, 249, 217

Umana G., Trigilio C., Catalano S., 1998, A&A, 329, 1010

Umana G., Trigilio C., Cerrigone L., Buemi C. S., Leto P., 2008, MNRAS, 386, 1404

Umana G., et al., 2015, aska.conf, 118

Umana G. et al., 2015, MNRAS, 454, 902

Urquhart J. S., Busfield A. L., Hoare M. G., Lumsden S. L., Clarke A. J., Moore T. J. T., Mottram J. C., Oudmaijer R. D., 2007, A&A, 461, 11

Urry C. M., Padovani P., 1995, PASP, 107, 803

Usov V. V., 1992, ApJ, 389, 635

Verschuur G. L., Kellermann K. I., van Brunt V., 1974, gegr.book, 127

Weisenburger K., West A. A., Irwin J., Charbonneau D., Berta Z. K., Dittmann J., Newton E. R., 2013, AAS, 221, 158.10

White R. L., Becker R. H., Helfand D. J., 2005, AJ, 130, 586

Wieringa M. H., Kesteven M.J, 1992, Measurements of the ATCA Primary Beam, AT Memo 39.3/024

Williams P. M., van der Hucht K. A., Pollock A. M. T., Florkowski D. R., van der Woerd H., Wamsteker W. M., 1990, MNRAS, 243, 662

Wit E., Van Den Heuvel E., Jan-Willem Romeijn, 2012, Statistica Neerlandica 66 (3), 217, 236

Wood M. A., Oswalt T. D., 1998, ApJ, 497, 870

Wright E. L., et al., 2010, AJ, 140, 1868-1881

Zacharias N., Monet D. G., Levine S. E., Urban S. E., Gaume R., Wycoff G. L., 2004, AAS, 36, 48.15